DOCTOR OF PHILOSOPHY

Direct Numerical Simulation of Transition and Turbulence in Magnetohydrodynamic Flows in Rectangular Ducts

Braiden, Lee

Award date:
2016

Awarding institution:
Coventry University

Direct Numerical Simulation of Transition and Turbulence in Magnetohydrodynamic Flows in Rectangular Ducts

Coventry University

Lee Braiden

A thesis submitted for the degree of

Doctor of Philosophy

August 2016

Direct Numerical Simulation of Transition and Turbulence in Magnetohydrodynamic Flows in Rectangular Ducts.

By

Lee Braiden

A thesis submitted in partial fulfilment of the Universities requirements for the Degree of Doctor of Philosophy

August 2016

To Sue

Acknowledgments

I wish to take this opportunity to express my deepest respect, thanks and admiration to my supervisor, Sergei Molokov. Your continual patience, guidance, understanding and humour have been steadfast throughout my time in studying this doctoral degree: without which, I do not believe I would have attained completion. You have taught me too much to mention. Thanks Boss!.

I wish to additionally express my gratitude to Dr Tim Hender for all his hard work on my behalf in accessing the Super computer which I have employed within this study. To Dr Alex Pendcenko for his un-wavering patience, humour and helpfulness in the ways of the force!!, Thank you master!!. I would also wish to show my appreciation to the Engineering and Physical Sciences research council and Culham Centre for Fusion Energy (UK) for the CASE PhD studentship award. Part of the work was carried out within the frame work of the EUROfusion Consortium and has received funding from the Euroform research and training programme 2014-2018 (grant No 633053). I wish to also thank Richard Looney, for his advice and discussions on many different topics.

Finally, I wish to demonstrate my sincere thanks, appreciation and undying love to my children, Alex, Luke, India and Mia, in addition to my wife, Sue. Over the past twenty years you have given me so much. Your hard work, both professionally and privately have been paramount in keeping our family striving forward. The loyalty you have continually shown to our cause has been without doubt, the one thing that has kept our family functioning. Without you I am nothing.

Abstract

In this work, a flow of an electrically conducting fluid is driven through a rectangular duct by a constant pressure gradient in the presence of a transverse, externally applied magnetic field: the flow is studied using the method of Direct Numerical Simulation (DNS). This particular Magnetohydrodynamic (MHD) flow investigation is important in the development of liquid metal blankets design, which is the proposed cooling system within nuclear fusion reactors. The duct walls parallel to the magnetic field are ideally electrically insulating, while the walls perpendicular to the magnetic field are ideally electrically conducting. This flow is referred to as a Hunt's flow. In this work the emergence of time dependent flow and its transition to a fully developed turbulent regime is explored. By fixing the strength of the magnetic field and increasing the fluid velocity, a number of time-dependent flow regimes have been observed in the side layers, which includes Ting-Walker vortices, elongated vortical structures, fully turbulent side-wall jets, as well as singular and multiple side-wall jet detachments.

It has been found that at low velocities, the time-dependant flow takes the form of Ting-Walker vortices, which develop in the side layers of the duct. For all but the lowest magnetic fields studied, the Ting-Walkers vortices completely disappear after a short initial transient time, being replaced by new, higher energy, complex, anisotropic vortical structures. Additionally, a number of new flow regimes involving jet detachment have been identified. This study also demonstrates that Hunt's flow exhibits hysteresis behaviour, where different unsteady states are possible for the same flow parameters.

Nomenclature

Re	Reynolds Number
Ha	Hartman Number
Re_m	Magnetic Reynolds Number
N	Stuarts Number
$\boldsymbol{\nabla}$	Nabla Symbol
x, y, z	Cartesian coordinates
$\boldsymbol{F}_{vol}$	Body Forces $[kg \cdot m \cdot s^{-2}]$
$\mathbf{u}$	Fluids velocity $[m \cdot s^{-1}]$
$\boldsymbol{E}$	Electric Field
$\boldsymbol{B}$	Magnetic Field
$\boldsymbol{J}$	Electrical Charge
ρ_e	Electrical Current density
$\boldsymbol{F}_L$	Lorentz Force
U_0	Characteristic velocity $[m \cdot s^{-1}]$
τ	Shear Stresses $[kg \cdot m^{-1}.s^{-2}]$
γ	Dynamic Viscosity $[kg \cdot m^{-1} \cdot s^{-1}]$
v	Kinematic viscosity $[m^2 \cdot s^{-1}]$
ρ	Fluid Density $[kg \cdot m^{-3}]$
∂_t	Time Derivative $[s^{-1}]$
p	Pressure $[kg \cdot s^{-2} \cdot m^{-1}]$

t Time [s]

$\in_0$ Permittivity of Free Space

μ_0 Permeability of Free Space

$\emptyset$ Electric Potential

Table of Contents

1 Chapter.

Introduction

There are many important applications and industrial processes where electrically conducting fluids are utilized. The casting of liquid metals such as aluminium and steel are excellent examples of such Figure 1(a). Additionally, conducting fluids occur in the propulsion systems of sea vessels, pumping mechanisms that produce a continuous non-pulsating flow; even our planet relies on conducting fluids to produce a protective shield against cosmic radiation.

A very different but equally important topic concerning electrically conducting fluids is the research into thermo nuclear fusion reactors (Tokamaks) Figure 1(b). Within the scope of the latter application, liquid metals are being investigated to act not only as a proposed cooling system for thermonuclear fusion reactors, but also as a breeding ground for the rare hydrogen isotope, Tritium (T).

Some materials have been removed due to 3rd party copyright. The unabridged version can be viewed in Lancester Library - Coventry University.

Some materials have been removed due to 3rd party copyright. The unabridged version can be viewed in Lancester Library - Coventry University.

(a) (b)

FIGURE 1. An example of the continuous aluminium casting processes (a). A vertical mid-plane cut schematic of a thermo nuclear fusion reactor (Tokamak) (b). [1]

Fusion energy has been identified by many countries as a clean replacement or alternative to conventional fossil and nuclear fuels, studies into which have been active for many years. Numerous plutonium enriching countries including the United Kingdom, France, USA, Russia and China all began to understand the great benefits and possibilities that fusion

energy could possess in aiding to relieve the imminent global energy short fall crisis. All countries mentioned are now in possession of a nuclear fusion reactor, which is leading to the development of new technologies and materials to be studied at a much more accelerated rate than in previous years i.e. divertor, liquid metal blankets and Eurofer.

Within the hostile environment of a nuclear fusion reactor, liquid metal, constituting the proposed protection system, is typically driven through rectangular ducts by a pressure gradient. The orientation of the rectangular ducts varies depending upon the particular blanket concept. Numerous ducts, which contain the constant pressure driven liquid metal are situated between large D-shaped magnets and the reactor's toroidal core (plasma chamber), thus fully encasing the torus. Due to the ducts encasement properties, the term liquid metal blanket has been coined and the ducts will now be referred to as such for the remainder of this work. The strength of the magnetic field employed within the rector can exceed 9 T. The fusion process occurring within the torus involves two hydrogen isotopes, Deutritium (*D*) and Tritium (*T*), which are accelerated at extremely high velocities around the plasma chamber until they eventually collide, thus fusing together. As the isotopes fuse, helium is formed, in addition to an extra neutron. The energy released from this process can reach electron levels of $17.6\,MeV$, forcing the operating temperatures within the torus to reach in excess of one hundred million degrees centigrade. At these temperatures the helium turns into plasma; matter's fourth state. It should be noted that the resulting plasma is one million times less dense than air, but also many times hotter than our Sun.

Throughout the course of many decades, various blanket configurations have been investigated, including circular, oval and rectangular. Out of the three primary concepts, blankets involving rectangular ducts have been the most desirable; this is due to the ease and symmetry in which blanket modules can be constructed and possibly replaced. In addition, various duct wall conductance ratios have been investigated, all with differing results. Historically this has included research into fully electrically insulating blanket [1], [2] and electrically conducting blankets [3]. The latter blanket concept delivers unusual high velocity jets located at the side walls, parallel to the external magnetic field Figure 2. Side wall velocity jets are absent in a fully insulating blanket. The side-wall jets are more pronounced and stronger when a third blanket concept is studied, which includes the sidewalls parallel to the magnetic field being electrically insulating and the Hartmann walls, which are the walls transverse to a magnetic field, being perfectly conducting. This third, particular duct

configuration is known as Hunt's Flow. In fact, Hunt's flow and the instabilities contained within the side wall jets are the focus of this entire study.

Within the context of the present investigation two main dimensionless parameters governing the flow have been employed: the Hartmann number (Ha) and Reynolds number (Re), both of which are defined in more detail within Chapter 2. The Hartmann number characterizes the ratio of the electromagnetic to viscous forces, while the Reynolds number – that of inertial to viscous ones.

FIGURE 2. Velocity profiles of Hunt's flow in a rectangular duct with perfectly conducting Hartmann walls and perfectly insulated side walls parallel to an external magnetic field at $Ha = 100,$ and $Re = 500.$

At the Hartmann walls, which are perpendicular to the external magnetic field, thin layers are formed in which a sharp drop in the fluid velocity is observed due to the no-slip condition at any boundary surface. These boundary layers are historically referred to as Hartmann layers and their thickness dependents upon the strength of the external magnetic field. The thickness of the Hartmann layer scales as $\delta_{HA} \sim LHa^{-1}$, where L is the duct width. As well as Hartmann layers, boundary layers parallel to the magnetic field are also observed, which are referred to as Shercliff layers. The thickness of the Shercliff layers scales as $\delta_{SH} \sim LHa^{-1/2}$, which means they are somewhat thicker than the Hartmann layers. Resolving both layers numerically poses severe problems which will be addressed in this study.

Lead-Lithium (*PbLi*), the proposed metal alloy to flow inside the blanket, melts at 327.5°C and as the blanket operates in excess of 400°C, the alloy is now classified as liquid. At this point, the metal being characterised as such, is studied as a subsidiary of physics commonly referred to as fluid dynamics. Furthermore to the governing equations that govern the motion of a fluid, there is a further branch of physics which must be included, electromagnetism. The combination of classical fluid dynamics and electromagnetism results in a fairly recent field of physics, Magnetohydrodynamics (MHD) and it is the general area of this research.

The mathematical equations which govern MHD flows are in general non-linear, thus can describe very different flow regimes. For instance, the flow may be turbulent, demonstrating chaotic behaviour. Analytical study into such fluid flow is extremely difficult and virtually impossible. It is for this reason why computer simulation has to be used to reproduce fluid flow. The continual advancement of computers has led to major, rather recent furtherance in computer-aided simulation design, commonly referred to, both in industry and academia as Computational Fluid Dynamics (CFD). CFD is a tributary of fluid dynamics, employing numerical analysis and algorithms to aid in solving fluid flow. By having the ability to model fluids in greater depth, scientists have gained a deeper understanding of the complexities of fluid flows in many different applications. It has been through the development of CFD that Direct Numerical Simulation (DNS) has been bought to fruition. By integrating DNS into large super-computing systems, it gives a much greater defined visual and statistical representation of complex fluid flows.

The thesis is structured as follows. Chapter 1 starts with a review of the historical development of nuclear fusion science. Additionally, Chapter 1 also contains a very brief introduction to the particular flow which this study encompasses, i.e. Hunt's flow. In Chapter 2 the governing equations in which this work is based upon will be derived. Chapter 3 contains the description of the DNS method which was employed in this study. Chapter 4 presents the main body of work, including procedures used and results obtained. Chapter 5 contains the results concerning high Hartmann numbers, which are values beginning to approach nuclear fusion environments. Within Chapter 6 the opposite limit of a low Hartmann number is investigated. The study then concludes with Chapter 7 where a summary of the work is presented and future work discussed.

1.1 Historical Background.

MHD is a relatively young discipline within the context of mathematics and fluid dynamics, incorporating studies of complex interactions with electrically conducting fluids and magnetic fields. The various phenomena and applications have intrigued scientists since its inception. Naturally, this leads us to the question, *When were the first MHD effects discovered and by whom?*

Within the context of MHD, Faraday's famously unsuccessful experiment in 1832 investigated the river Thames tidal motion through the use of electromagnetic induction. His early study may be seen by some scientists as the starting point in which MHD began, but Faraday's experiment was not strictly an MHD experiment. Others may argue that it was not until many years later, that the catalyst for MHD began with the early investigations by Hartmann and Lazarus [4]. The interaction between conducting fluids and magnetic fields gave rise to an unexpected phenomenon, oscillations of ions residing within a conducting fluid as it passed through a magnetic field. Hannes Olof Gosta Alfven (1908-1995) discovered that if a conducting fluid passes through a constant magnetic field, an Electro Magnetic Force (E.M.F.) is induced, thus producing electric currents [5]. The force arising from the interaction of these currents with the magnetic field affects the motion of the liquid, thus giving rise to a combined electromagnetic-hydrodynamic wave. For the discovery of these waves and thus founding MHD, Alfven became the recipient of a Nobel Prize in 1970. Alfven aptly named these waves," Alfven waves".

A little over seventy years ago, scientific research gained its first insights into the fundamental physics which allows stars to keep their luminosity over a time period of billions of years. Scientific research discovered that stars are essentially held together by their own mass, pulling inwards, compressing themselves against gravity. This process in turn dramatically increases the temperature and pressure at their core. The highly increased temperature and pressure, results in a nuclear reaction which transforms hydrogen into helium, thus generating huge amounts of energy. This process is now known as nuclear fusion [6]. Upon understanding the fusion process within the stars, scientists began to consider whether the process could be replicated on Earth. Therefore scientists began to

initiate formulations attempting to harness this enormous amount of energy. It is the harnessing of fusion energy which is the main motivation behind this work.

1.2 TOKAMAK 1950-1960.

A small team of scientists in the USSR working on thermonuclear weapons design within the Arzamas-16 nuclear centre, Moscow, began to formulate initial principles of magnetic confinement at high plasma temperatures [7]. Fundamental, initial research led the team to enthusiastically suggest possibilities of a future thermal nuclear reactor. This initially small team of Soviet scientists was led by Igor Yevgenyevich Tamm, (1895-1971) and his former postgraduate student Andrei Dimitrievich Sakharov, (1921-1989). Both men became highly influential in the early development of plasma magnetic confinement, not only in the Soviet Union, but throughout the thermo nuclear scientific community. In 1958 Tamm received the Nobel Prize in Physics for his combined work on the Cherenkov-Vavilov Effect [8]. Sakharov won a Nobel Peace Prize in 1975 for his work on civil liberties and reforms in the Soviet Union, to which a Sakharov prize is awarded each year by the European Parliament in his honour.

Following on from the Soviets scientific teams ideas, research into plasma initiation and heating in toroidal systems began to gather momentum in 1951 at the Kurchatov institute, Moscow. Sakharov, having undertaken his Ph.D. studies under the direction of Tamm, begun to formulate provisional parameters of a toroidal reactor, with a power capacity of 900 Mega Watts (MW). The reactor consisted of an outer toroidal radius of R = 1.2 m, a smaller inner radius of A = 0.2 m, a magnetic field, $\boldsymbol{B}_0$, of 5T and an ion temperature of 100KeV. Early experimental toroidal chambers at this stage of development by the team were made from materials which included glass, porcelain and metal, all of which included insulating inserts. The research and developments of the different material configurations quickly lead and progressed to the first nuclear fusion reactor in 1958, the T-1 Tokamak (Tokamak is a Russian abbreviation for Toroidal Chamber with Magnetic Coils TCMC). The T-1 Tokamak was the first toroidal Tokamak featuring a steel vacuum vessel, in which the temporary stability of plasmas was demonstrated, thus satisfying the Kurskal-Shafranov stability condition [9]. The experiments suggested that for the stability of plasma the pitch angle of the

magnetic fields curvature needed to be very low. The new dimensions of the T-1 accommodating this suggestion were R = 0.8 m, A = 0.13 m, $\boldsymbol{B}_0$ = 1.5T and I = 0.25 MA. It was observed within the team's early initial experiments that the dominant role in the power balance of the hot plasma was played by the losses caused by ultra-violet radiation [10]. With this observation in mind, the T-2 was constructed a year later in 1959. The research on the re-developed T-2 attempted to re-address the problem of radiation losses and steps were implemented to mitigate this, which were met with some success. In attempting to eradicate this problem entirely, the Russian team installed an innovative inner vacuum chamber that could be heated to 500 degrees centigrade. Located within the newly installed inner vacuum chamber sat a diaphragm, which limited the area of the discharge currents, thus resolving the radiation losses and eliminating the problem.

1.2.1 1960 – 1970.

1962 witnessed the next development stage of Tokamak design, the T-3. The T-3 had an increased outer toroidal radius of 1 Meter, in addition to an increased magnetic field. Due to the plasma being electrically conducting, a pulsed induced current could be employed to heat the plasma, thus allowing for full ionization of the major impurities through a process known as Ohmic heating. The parameters of the T-3 were R = 1 m, A = 0.12 m, $\boldsymbol{B}_0$ = 2.5T and I = 0.06 MA. The increase in radius moved the new design of the Tokamak in the correct direction, as full ionization was achieved in a stable plasma regime at a record 1 KeV (10 million degrees centigrade). In addition to the success of the increased radius, a plasma density limit could be achieved, thus giving rise to the Kurchatov density limit [11]. 1966 saw studies, using the T-3, into external perturbations by visual plasma radiation, further leading to observations of a helical plasma structure. This feature is now common to all Tokamak perturbations. During the 1960's to the early 1970's, six different Tokamak designs were fabricated and investigated, the T-3, T-3a, TM-1, TM-2, TM-3 and the T-4. The results of the experiments in nuclear fusion were considered by many scientists outside of the small dedicated Russian team as evidence of thermo nuclear isolation of the plasma in a toroidal system, and 1968 lead to beneficial debates resulting in the first international collaboration in nuclear fusion [12]. With the advancing work and development on the T-3, the initial collaboration existed between the Kurchatov Institute, Moscow, Russia and the Culham

Plasma Physics Laboratory, Oxford, England. The concluding results of the collaboration between the two laboratories established the Tokamak as the correct direction for further research on magnetic plasma confinement [13]. The pioneering collaborative work increased its influence in 1969 as Princetown scientists in America supported the switch from purely toroidal experiments to Tokamak investigations. With the encouraging results determined from the Russian and English collaboration, new Tokamak designs were proposed and later fabricated, the T-3a, Figure 3 and T-4.

The progressive experiments carried out upon the T-3a and the T-4 included the usage of Deuterium, observing how it changed over time for various models. Results were then compared against known cross sectional results of the original reactor. The comparative results lead to the first recorded observation of a stable toroidal plasma column [14]. Not only did the T-3a and T-4 demonstrate a stable plasma column, but along with the TM-2, TM-3 and later the T-11, they gave scientists the ability to establish scaling laws for energy confinement. The community achieved this by deducting from the size of the magnetic field value, discharge and plasma densities [15]

1.2.2. 1970 – 1980.

1970 witnessed for the first time a Tokamak employing a fully graphite chamber, rather than the familiar metal chamber. Graphite was employed to investigate whether there was a lower charge of plasma ions. The change in chamber material was a complete success [16]. In addition to this, Shafranov proposed an elongated plasma cross section to improve stability to the external perturbations. Further studies were performed by magnetic probes upon this suggestion.

Shafranov's proposal lead to the development of the T-9, T-8 and the T-12 in 1972. 1971 saw further investigations conducted on the T-4 into different areas of Tokamak technologies, discovering features of internal MHD effects. At this point France began designing their own TFR Tokamak series, which resulted in large Tokamak designs, ultimately leading to the J.E.T (Joint European Torus) program [17]. Scientific research was developing, either as single studies or joint collaborations, all of which lead to the first D-shaped cross sectional

Tokamak in late 1971. Also in this year the T-6 was designed [18], with parameters R = 0.7 m, A = 0.17 m, $\boldsymbol{B}_0$ = 1.5 T and I = 0.22 MA.

FIGURE 3. The T-3a Tokomak housed at the Kurchatov Institute 1964. [2]

1975 observed the development and fruition of the largest Tokamak at that time, the T-10. It's parameters were R = 1.5 m, A = 0.4 m, $\boldsymbol{B}_0$ = 4.5 and I = 0.68 MA. There were two main outcomes from this larger Tokamak experiment. The first concerned the investigations into Ohmic heating and the maximum possible plasma temperatures allowed through this type of heating. Secondly, the T-10 employed auxiliary plasma heating techniques. The results of these particular types of heating experiments were able to reach an efficiency of 70% - 80% [19]. Electron heating in the central areas of the T-10, at the Ohmic stage of the discharge increased from 0.6 to 0.9KeV and the electron temperature attained in these experiments reached 10KeV. The large dimensions of the T-10 and subsequent Tokamaks from this point on, in an historical context, were achieved on the basis of numerous plasma energy scaling's. 1978 saw the T-7 in operation, with parameters R = 1.22 m, A = 0.31 m, $\boldsymbol{B}_0$ = 3 T and I = 0.39 MA. When research had been completed on the T-7, it was disassembled and relocated to China as a gift from Russia. The T-7 was transported to China under great economic difficulties and housed at Hefei [20]. The move took more than three years to complete, but nevertheless in 1995 the TH-7 was commissioned, thus marking China as a valued member nation in the possession of a Tokamak. Recently the TH-7 was re-housed after being de-commissioned to Huainan, eighty kilometres west of Hefei, where it is still situated.

1.2.3. 1980 – Present.

The first superconducting Tokamak, the T-15 was commissioned in Russia in 1983. Due to economic difficulties, research on the T-15, which was housed at the Kurchatov Institute, Moscow, was put on hold in 1995, but not before successfully demonstrating a first plasma burn in 1988. Quiet recently there have been plans to upgrade the T-15 by installing a new divertor, which is proposed to remove plasma waste, i.e. heavy ions, more efficiently. Scientists at the institute are aiming to initiate the device again towards the end of 2017. The T-15's twenty four toroidal field coils are still the largest in the world to date. 2006 witnessed the signatures of seven participant members including the European Union, Japan, India, Russia, China, America and South Korea. All nations agreed to pledge financial support to the worlds' largest thermo nuclear reactor, ITER (International Thermonuclear Experimental Reactor). Located opposite the Cadarache institute, southern France, I.T.E.R, once completed, will boast the worlds' largest magnetic plasma confinement physics experiment. It is designed to produce over 500 megawatts of power while only drawing 50 megawatts of power to operate the reactor. Proposed plasma experiments are scheduled at I.T.E.R for 2025 and a full tritium-deuterium plasma burn is expected in 2035.

It is important to emphasize that during the early years of Tokamak development through the 1960's, 1970's and 1980's, parallel investigations at the Kurchatov Institute into plasma stability were conducted. The work done on 2-D and 3-D plasma equilibrium, linear and non-linear stabilities, plasma heating and non-inductive driven currents, created the foundations for which magnetic confinement of hot plasma in thermo nuclear reactors is based on today[21], [22], [23]. The Tokamak has proved successful by the combined research effort that the Russian and English scientific thermo nuclear community developed in the 70's. Within this particular time period, it was the first time that a wide range of international delegations and scientists had come together to develop one project. It was these pioneering, ground breaking collaborations which have built the basis on which the thermo nuclear reactor under construction at ITER is based.

In the early nineties, hydrogen isotopes Deuterium and Tritium were being used as fuel for the T.F.T.R (Tokamak Fusion Test Reactor) in Princeton, USA and J.E.T (Joint European Torus) located at Culham in the U.K. J.E.T gave the world the opportunity of multi- national collaborations, and in 1991 achieved the worlds' first controlled nuclear fusion reaction. With

the continual developing work on the T.F.T.R., J.E.T and Japan's Tokamak programme, the JT-60, scientists are striving to achieve 500MW of output with only 50 MW input. Below is a historical account of the processes that has recognised nuclear fusion as the main source of power for the latter part of this century and into the future.

As Tokamak construction and investigations were at arguably their height of academic interest across the globe, theoretical work on conducting fluids in an external magnet was conducted on the periphery of fusion development. It was realised very early by the scientific community, that in order for the nuclear fusion reactor Figure 4, to burn plasma for extended periods of time, some form of cooling system needed to be developed, along with a way of extracting heat from the plasma. It is at this point that we now turn our attention away from the Tokamak and take a closer look at the pioneering scientists undertaking early investigations into MHD, which resulted in the development of a proposed cooling system for the Tokamak, liquid metal blankets.

FIGURE 4. A schematic of the nuclear fusion reactor to be built at ITER. Highlighted are some key components of such a fusion reactor. [3]

1.3. Harwell meeting, 1956.

In 1956, the year before Arthur Shercliff was given his lectureship at Cambridge, a Russian scientist named Igor Kurchatov, who was not well known outside of Russia at that time, was invited to give a presentation at the Atomic Energy Research Establishment in Harwell, Oxfordshire [24]. From the outset of Kurchatovs' presentation, it was apparent to the members present that the Soviet were researching thermo nuclear fusion power. Kurchatov demonstrated that the small team he was a member of was using hydrogen isotopes as the end product of a peaceful power production concept. This was quite a remarkable situation, as .unknowingly to Kurchatov, both England and America has been researching the same thing at approximately the same time. The difference albeit between these three nations was that the research done in America and England was highly classified. Kurchatov's bold, initial statement on the issue was a revolutionary step forward in opening up fusion research in all three countries. This pioneering move by Russia resulted in a major exchange of scientific information for all three countries involved at the United Nations Conference two years later in Geneva, 1958 [25]. All three countries now had a common interest in developing a way to contain hydrogen isotopes at high temperatures to enable a fusion reaction to occur, ultimately releasing energy.

1.3.1. Scientists.

To begin this section one is required to re-visit the pioneering work conducted by Hannes Alfven in Stockholm, Sweden, in the 1940's [26]. Leading from his early success, Alfven assembled a scientific team consisting of twenty members, half of which were completely dedicated to scientific research. The group's laboratory was situated in the Royal Institute of Technology, Stockholm, Sweden. A main feature housed within the laboratory was a large magnet which produced a homogeneous magnetic field up to 1.5T. It was through the studies in employing the magnet that Alfvens' group observed an interaction between the magnetic field and mercury. The interaction between the magnetic field and the electric currents induced by the flow affected the movement of the mercury, resulting in strong MHD drag effects.

Maintaining the focus within the same decade, we now divert our attention away from Alfvens' research group in Sweden and onto England, or to be more precise, the Engineering Department at Cambridge University and L.M.Trefethen. Trefethen came to Cambridge having completed a master's degree at the Massachusetts Institute of Technology (M.I.T) and his interest in heat transfer properties lead to an acceptance in 1946 of his research proposal, entitled "Gas Turbines-turbine blade cooling". Trefethens' investigative reputation quickly developed whilst he studied at Cambridge. One experiment in particular which he conducted in 1946 included driving mercury through a pipe and measuring its flow rate by electromagnetic means [27]. From Trefethens initial studies and results into this phenomenon, one can postulate, that MHD had arrived at Cambridge University. One year later W. Murgatroyd was recruited at Cambridge University to also work upon liquid metal heat transfer within the Engineering Department. Often collaborating with Trefethen on his liquid metal flow circuit, Murgatroyds' accepted research proposal was entitled "Heat Transfer from Liquid Metals". Eventually, through collaborative investigations with Trefethen, Murgatroyds research into turbulence, lead to his pioneering results on the transition to turbulence that the MHD community will always attribute his fame [28]. As Murgatroyd progressed through his doctorate and apparatus allowing, he employed higher values of Reynolds numbers into his system, which was comparable to the research conducted by Hartmann and Lazarus [4] nine years earlier in Denmark. Hartmann and Lazarus demonstrated that a conducting fluid subjected to high magnetic fields, produces thin layers near the walls of the channel. Within the context of MHD they are commonly referred to as Hartmann layers. Murgatroyds' studies observed these layers to be much thinner than their distance apart in the system, thus resulting in the discovery that non dimensional qualities, such as the friction coefficient, depended upon *Re/Ha* [28].

Before Murgatroyd completed his Ph.D., John Arthur Shercliff (1927-1983), arguably the most significant scientist within the MHD community began his studies into liquid metals at Cambridge University. It is necessary to give a slightly extended overview of Shercliff due to the exceptional contributions this scientist gave to not only fluid dynamics in, but also to MHD.

In 1938 Shercliff won a scholarship to Manchester Grammar School. During his three years at the school, he acquired nine distinctions in total. This high academic achievement allowed his progression to a further three years study at sixth form studying mathematics. The excellence shown within the further three years won Shercliff a one year open scholarship at

Trinity College, Cambridge in 1944. He arrived at Trinity College very highly regarded by his former tutors and spent an additional three years studying an undergraduate degree in physics and mathematics. Upon completion of his undergraduate degree he gained the most distinguished undergraduate title at Trinity College in 1947, which allowed him to win the Rex Moir prize [29]. This outstanding prize paved the way for a further award, the Joseph Hodges Memorial Fellowship, giving Shercliff the opportunity to study a one year master's degree at Harvard in 1948. Whilst at Harvard, Shercliff demonstrated his enthusiasm in physics and mathematics and achieved his master's degree two years later in 1950. 1951 saw Shercliff being appointed as full apprentice at A.V. Roe & Co Ltd, an aircraft manufacturing company. Shercliff only completed one year of his apprenticeship, owing to an opportunity arising to study a research Ph.D. under a former tutor at Trinity College, W.R. Hawthorn. Being given this opportunity, Shercliff's approved Ph.D. research was entitled "Problems in Magnetohydrodynamics". Almost immediately, Shercliff began working on a conducting fluid as it flowed through a transverse magnetic field [30], [31], [32], [33]. This initial research lead to the discovery of boundary layer characteristics of fluid flows at high magnetic fields, an important discovery, as this demonstrated a relationship between the volume flux of the fluid and the pressure gradient. Encouraged by these preliminary results, Shercliff continued further into his Ph.D. and began to explore deeper into fluid flow and electrodynamics flow-meters. He subsequently completed his Ph.D. and was bequeathed a lectureship at Cambridge University in 1957, a position he held until 1964.

Combining both lecturing and research, Shercliff in 1959 produced a further two definitive papers on incompressible Magnetohydrodynamics [34], [35]. The first included results on the flow of a purely transverse fluid flow to a magnetic field, the second included coinciding results of the effects of a magnetic field within flow direction. Six years later in 1965 Shercliff gained an appointment at a new university in the middle of England, Warwick University. There he was given the rare opportunity to develop the new engineering department as he saw fit. By being able to employ such autonomy, he gave the new undergraduate courses a great amount of flexibility, by combining different fields of mathematics, physics, engineering and the recently developing field of computer sciences. Due to the pre-occupation of developing the engineering department, scientific papers by Shercliff diminished throughout the late sixties and early seventies, but upon completing a two year sabbatical at the Culham Laboratory, Oxfordshire, Shercliff produced his second text book [36].

Throughout Shercliffs' scientific career he gained and served in many highly prestigious positions including: 1976-1979 Committee of Engineering Professors, 1975-1980 Vice chairman of the advisory committee to the Coventry area Health Authority on medical engineering, 1980 elected fellowship of the Royal Society, I.C.I Professorship of Applied Thermodynamics at Cambridge, re-elected as a fellow of Trinity college, Cambridge and Associate editor of the Journal of Fluid Mechanics. In the latter part of his career, Shercliff became increasingly un-well which prevented him from continuing his research into science. Nevertheless, he honoured his standing commitments into the early eighties, culminating with his death on the 6th December 1983.

1962 is regarded through historical events by many scientists as the "Golden Age" in MHD research. Not only through scientific advances, but also for the scientists themselves, the names of which have been and will be continually introduced as we progress through this continuing section.

C.J.N Alty, J. A. Baylis and C. J. Stephenson joined Cambridge University as research students in the early 1960's. All three new research students had a large interest in a paper written two years earlier [37]. Within this paper, Hasimotos observed fluid behaviour in a parallel flow, located outside an infinite cylinder, exposed to a transverse external magnetic field. This was the first intimation that free shear layers parallel to the magnetic field play an important role in external flows. Upon reading Hasimotos' work, Shercliff observed that it also had implications for fluid flows in square ducts when two walls were insulating and the remaining two walls were conducting, again in the presence of a uniform, but tilted, transverse magnetic field. Alty's proposed and accepted PhD was entitled "Fully developed secondary flow in Magnetohydrodynamics" and acting upon Shercliff's advice, began conducting experiments based on this configuration, using mercury as the fluid and copper as the duct walls. Alty used ordinary sellotape as the insulating material in his experiments and employed an external magnetic field with strength of approximately 1.2T. The mercury flow was driven along the duct via a longitudinal pressure gradient against the electromagnetic forces, which were induced by the short circuit path between the two copper walls. This particular experiment resulted in further investigations into the pressure difference down the duct in connection with buoyancy-driven MHD flow [38].

Baylis, having his proposed PhD entitled simply as "Magnetohydrodynamics" accepted at Cambridge began, again under the advice of Shercliff, to conduct experiments on the stability

criterion for Couette flow between the gaps of the torus formed from concentric copper cylinders [39]. The magnetic field strength was reduced in comparison to Alty's experiment, by approx. 0.3T. By reducing the magnetic field strength, Baylis was able to compare the observations to previously known results [40] earlier that same year. The stability results were a little higher than that of Chandrasekhar, but this was put down to the uncertain gap width of the copper cylinders due to an amalgam layer building up on the copper. Baylis next conducted an experiment on a toroidal chamber, aiming to investigate the fluid's secondary flow effect. But as the experiments were progressing, Baylis discovered that it was an excellent opportunity for testing asymptotic channel flow theory.

Late 1963 saw the introduction of two further research students at Cambridge under the guidance of Shercliff. The two new students were R.C Baker and J.C.R Hunt. Immediately, Shercliff suggested to Baker that he should investigate the stability of mercury in a trough set within a horizontal magnetic field. Shercliff further suggested that a horizontal electric current would interact with the magnetic field, resulting in an upward vertical force and along with these unsteady conditions 2-d waves would grow exponentially with time. As a result, it was observed that slightly before a complete breakdown of the fluids surface a crest would rise, albeit a very small one, thus demonstrating encouraging stability results. Upon completion of his stability experiment, Baker decided to re-align his focus and investigate electromagnetic flow meters. Baker advanced the electromagnetic flow metering by demonstrating that a voltage difference between the two channel walls would depend on the fluid's velocity and its distribution over the distance of the channel walls. Baker's advances in this experiment, culminated into a formula for the overall potential difference: he quite aptly called it, Baker's formula [41].

Hunt in the meantime, although registered at Cambridge as a PhD student only spent one full year there, relocating his studies to Warwick University. This was no doubt influenced by Shercliff's new appointment as Head of the Engineering Department there. During Hunt's initial year at Cambridge, he observed that he could further develop his supervisor's work of analysing a rectangular duct with insulating walls and conducting walls perpendicular to a uniform magnetic field. As a result of this investigation, Hunt produced two initial papers in 1965 [42], [43]. The two papers just stated are the basis on which the present author's work is based upon. Throughout Hunt's highly successful scientific career he collaborated with over seventy different scientists, achieving in excess of three hundred and sixty scientific papers.

At present, Sir Hunt is a fellow of Trinity College Cambridge and an Honouree professor in the Department of Applied Mathematics and Theoretical Physics.

MHD began to gather great interest at this stage and early pioneers within this new phenomenon began to take up the mantle and researched different effects a magnetic field had on a conducting fluid. Before moving deeper into MHD's history, it is extremely important at this stage to disseminate different avenues of MHD research. Within the context of this work we will look at the history of MHD on a relativity small scale, i.e. the effects of a magnet on a conducting fluid passing through a duct.

1.4. Evolution of Liquid Metal Blankets.

The pioneering scientists of the 1950's realized nuclear fusion power was indeed attainable. They also determined that in order for fusion to be initiated between the two hydrogen isotopes Deuterium and Tritium, temperatures needed to reach in excess of $10^{8^{\circ}}$C. Reaching such high temperatures would totally dismiss conventional solid wall confinement. Therefore a particular genre of plasma magnetic confinement using large D-shaped magnets was realized as the only option available in order to suspend the plasma within a toroidal chamber. In order to protect the large powerful D-shaped magnets employed for the plasma confinement, a radical proposal was initiated to develop a blanket concept where liquid metal flowed within and through the blanket, which were placed between the plasma filled torus and the large magnets themselves. The blankets were designed to shield the magnets against high neutron radiation emitted from the Deuterium-Tritium plasma burn and for heat and mass transfer properties. Therefore by implementing the liquid metal blankets, a protective cooling system would be in place, thus allowing the plasma to burn for extended periods of time. It is believed that when ITER comes online in 2035 that numerous physical experiments into blanket operations will be undertaken. Under such physical conditions, the experiments will attain whether a particular blanket concept can indeed be a candidate for future further investigation into the purpose for which it is intended. The research contained within this present work will address the candidacy of a very specific blanket design concept and determine whether this specific blanket design is sufficient enough to be taken seriously as a real contender for future possible realization.

1.4.1. Modern Experimental Liquid Metal Blankets.

A liquid metal blanket has primarily three functions; it is required to absorb the fast neutrons which are expelled from the fusion process, converting their energy into heat. Secondly, it is to be employed as a breeding ground for the highly elusive element Tritium, which is the fuel required to initiate the fusion process and thirdly, to protect the powerful D-shaped magnets from both heat and neutron radiation bombardment [49]. In order for the blanket to operate within safe tolerable limits, the first wall (the wall closest to the plasma) which receives the highest amount of heat flux, must remove heat at such a rate that temperatures do not exceed critical limits. For this to be attained, liquid metal has been viewed by many scientists as the prime candidate to be used within a blanket concept. Extensive research has found a mixture of lead-lithium alloy (Pb-17Li) to be the ideal fluid, mainly due to the leads' high thermal content and the Lithium component providing a good breeding grounds for Tritium [50].

Over many decades different blanket designs have been investigated, but as to date a fully agreed blanket design has yet to be decided upon. As we progress through this section, we will briefly describe different blanket concepts that have been, or are, being investigated.

1.4.2. Self-cooled Liquid Metal Blankets.

Self-cooled liquid metal blankets, essentially use the same fluid as a coolant and to breed tritium, thus greatly simplifying the design and material constraints. Although this is advantageous, there are certain constraint factors that must be observed within such a design. Two of the constraints include material compatibility between the blanket walls and the liquid metal coolant being used [51], additionally the liquid metal must be able to proceed through the blanket at a sufficiently increased velocity in order to remove the intense heat generated by the plasma burn [52]. A simple concept was designed to include staggered rows of circular pipes curving around the plasma Figure 5

FIGURE 5. Schematics of cylindrical poloidal channels for the use in thermo nuclear fusion reactors; (a) demonstrates circular pipes that remove heat away from the first wall, (b) poloidal channels, (c) manifolds in reactor sectors. [5]

Behind these were ducts of rectangular cross section. The fluid would enter both pipe and duct at the top via a manifold, flow through the blanket and exit via a collection point located at the bottom of the blanket. By theoretically applying this particular design to a thermo nuclear reactor we have a so-called poloidal blanket, primarily designed for the central part of the reactor. To date the most advanced blanket concept of this design is the Self Cooled Lead Lithium Blanket and is the product based upon advanced theoretical and experimental plasma physics investigation upon a coaxial flow. The vessel's design is based upon a ceramic fibre composite structure and is generally thought of as a good candidate for low activation wall material, mainly due to its electrical insulation properties, thus leading to higher electrical resistance, reduced electrical currents and pressure drop. The latter point in a poloidal flow of the self-cooled liquid metal blanket does not seem to issue, but three dimensional effects of the blanket's ends give an extra contribution to flow resistance, therefore should be investigated in the future.

1.4.3. Toroidal Blankets.

Up to the present, the main problematic historical trend is the problem of pressure drop within the self-cooled liquid metal blanket concepts. In 1971 a report by Hunt & Hancox [53]

directly mentions the use of a toroidal fluid flow within a blanket, in which circular pipes are used within the toroidal cooling ducts, thus allowing MHD effects to be kept to a minimum. The alignment of the fluid flow with the magnetic field would therefore suppress turbulent fluctuations within the fluid itself. The first wall is cooled by a high velocity fluid flow through small narrow channels being supplied through a slanted poloidal manifold, perpendicular to the magnetic field. An advantage to this type of design is that the mean velocity in these poloidal ducts can be kept low, thus reducing the pressure drop, through the manifold itself. Secondly, the poloidal channels are able to absorb high stress levels since they are not exposed to the ducts' first wall and high radiation doses. Due to this configuration, the toroidal channels are perpendicular only to the poloidal field, which are much weaker. This results in a high fluid velocity in toroidal channels, without increasing the overall pressure drop within the system, making this concept very attractive as a future design feature.

1.4.4. Separately cooled Liquid Metal Blankets.

Within this concept, the Pb-17Li acts primarily as a tritium breeder unit, while the heat produced by the plasma is removed by fast flowing helium [54]. As the helium is non-conducting, it does not suffer from MHD interaction, thus it can be circulated through the magnetic field at high velocity without affecting the MHD pressure drop, thus removing heat more efficiently. Concerning the main flow, the Pb-17Li can circulate through the blanket at a much lower velocity, resulting in a decreased pressure drop within the system, compared to Self-cooled liquid metal blankets. The design of this type of blanket is composed of liquid filled rectangular boxes arranged around the plasma. All blanket walls, including the first wall, are cooled by helium flowing inside the blanket walls in small channels. In addition to this, inserted between each liquid filled box are cooling plates, aiding in keeping temperatures between tolerable limits and aiding structural integrity. The MHD difficulties for this design are the flows in slim ducts, which are the product of the insertion of the cooling plates, and also the expansions and contractions of inlet and outlet areas of the breeder units. Another issue due to the cooling plates is the electrical coupling between the plates themselves, this would allow, if not sufficiently insulated, allow electrical currents to pass from one fluid region to another within the system.

Liquid metal blanket design and development over past years has had to contend with various difficulties, such as the pressure drop, duct flow, duct expansion-contraction, electrical flow coupling - to name but a few. Most, if not all differing phenomenon that occurs within three dimensional flows in single ducts can be modelled and in some cases understood via computer modelling. But the designing of fusion blankets using 3-D flow modelling is not yet fully sufficient enough to accurately predict MHD in the blanket in its entirety as a single component. All progress so far in the theme of nuclear fusion MHD research has thus been updated by scientific experimental work confirming theoretical based investigations. The scientific progression conducted within the context of liquid metal blanket design and all future investigations, either performed at JET or ITER, are fundamental in the realization of thermo nuclear fusion power. If blanket design and development is not continued in the future, nuclear fusion power will not become a reality.

1.5. What is Hunt's Flow ?.

Fluid flow in rectangular ducts is comprised in many different blanket concepts, as just briefly described. In the following, we focus on a specific combination of wall conductivities, where the walls parallel to the magnetic field are insulating and the walls transverse to the magnetic field are conducting. The reason for investigating this particular configuration is that it gives rise to Hunt's flow; nearly all of the characteristic features to many blanket concepts are present in this flow.

Here we give a brief overview of Hunt's flow. The complexities and governing equations will be described in greater detail in subsequent chapters. By assuming a duct of rectangular cross section has perfectly conducting Hartmann walls transverse to the magnetic field, i.e. the electrical conductivity of these walls being $\sigma_{HW} = \infty$ (top and bottom), in addition to perfectly insulating side walls parallel to the field, $\sigma_{SW} = 0$, it leads to a determined duct configuration referred to as Hunt's flow. A conducting fluid is driven through a rectangular duct by a constant pressure gradient, subjected to an externally applied magnetic field. An important feature to such a regime is the requirement to produce sufficient turbulence within the fluid flow in order to promote heat and mass transfer within the system. This scenario in itself could be problematic, as high MHD effects produce strong braking and damping of turbulence within the core of the fluid, as viscous forces attempt to balance the pressure

gradients, scaling as 0(*Ha*), thus altering the fluid flow through the duct. Such braking produces an unusual velocity profile not observed in a purely hydrodynamic flow regime or in MHD flows with fully insulated wall.

Due to the fact that we employ $\sigma_{SW} = 0$, induced electrical currents produced in the core of the fluid must turn almost parallel to the external magnetic field. Once the currents turn at the side walls, MHD effects are greatly reduced in this region, allowing increased fluid velocities, thus producing side wall velocity jets Fig 6. The analytical complexities of such a flow are well known and the specific velocity profile was solved by Hunt in 1965 [42]. Within this particular configuration, the side wall jets are well pronounced when compared to a fully conducting duct regime, or a fully insulating duct regime. As *Ha* increases, i.e. $Ha \to \infty$, the mass flow rate in the jets increases and the velocity in the core of the fluid tends to zero, suggesting that the jets carry most, if not all of the flux. Since Hunt's analytical solutions into such a specific regime were presented in 1965, remarkably very few additional investigations have been conducted, except for [102,103]. Therefore, with the aid of DNS, this is the first time that an in-depth investigation into Hunt's flow with varying parameter of *Ha* & *Re* values has been conducted.

FIGURE 6. Flow geometry of Hunt's flow in a square duct. Laminar velocity flow profile distribution with perfectly conducting Hartmann walls, $\sigma_{HW} = \infty$, and perfectly insulating side walls $\sigma_{SW} = 0$ at *Ha* = 100 (blue). Electric current lines are also shown (brown).

1.6. Literature Review.

Early research into the effects that an external magnetic field had on laminar, incompressible, conducting fluid flow were initially focused on conducting pipes [55, 56]. The results which ensued observed that depending on the conductivity of the walls, boundary layers developed at the side walls Subsequent research developed from these early studies [57, 58, 52, 59, 60] as different wall conductance ratio's and ducts geometries were investigated in greater detail.

Ensuing research progressed into studying rectangular ducts with conducting walls which were perpendicular to the magnetic field and insulating walls parallel to the magnetic field [42, 43]. Hunt found the exact solutions to this particular duct problem through the use of Fourier series. Additionally, he observed that by employing thin duct walls, the magnetic field had an enhancing effect on the fluid flow in the boundary layers, compared to that in the core. This had a dramatic effect on the velocity profile. These new and encouraging results spurned Hunt to develop his inquiries further [61, 62]. Over a period of three years, Hunt's studies led to five separate collaborations on MHD [63, 64, 52, 65] including one with his former supervisor at Cambridge [66].

Due to early pioneering work in MHD, the conductance of the duct walls was viewed by those involved to be of paramount importance, encouraging further investigation by other scientists to either fill in the gaps which Hunts research had left, or confirming his results [67]. An important resultant from the continuation of Hunt's initial studies were that boundary layer at the side walls of the duct were observed with thickness $0\left(Ha^{-\frac{1}{2}}\right)$, both theoretically and experimentally [68]. Using the same duct material as in Ref [38], but now with a duct conductance ratio of $c = 18.5$, thus, all walls being well conducting, Gelfgat, Dorofeev & Scherbinin observed that the side wall velocity jets were thicker than Hunt had predicted, in addition to being lower in magnitude at $Ha = 100, 200$. A subsequent paper published one year later confirmed this result [69].

Most, if not all early studies into MHD had been conducted analytically for low to moderate Ha, mainly in part to the limiting computer resources available at that time and the magnets employed within the experiments yielded relatively low magnetic fields. However, studies into high values of Ha were conducted in subsequent years to investigate the varying levels of suppression a stronger magnetic field could exert on a conducting fluid [70, 72, 73, 74].

The preeminent consensus was that as the magnetic field was increased, it did indeed damp turbulence. In realizing this phenomenon, in addition to the increasing levels of computer resources now being available, modelling fluid flow and the investigations into the transition to turbulence began to gather momentum [75]. In fact, transition to turbulence has been extensively investigated in both pipe flow [76, 77] and rectangular ducts [78, 81]. But a complete encompassing theory as to the inherent instabilities and the transition to turbulence has yet to be determined.

A fundamental experimental result in MHD came through utilizing thin conducting walls with, $c = 0.07$ for $Ha \leq 5800$, where c is the so-called wall conductance ratio, definition of which can be found within Chapter 2 [82]. Within this study it was observed that fluid flow became turbulent in the near side wall region at $Re \sim 3000$. This suggested that perturbations in side layers, housed near the parallel walls were responsible for the thickening of the velocity jet. This study gave a jet thickness of order $\sim N^{-\frac{1}{3}}$, where $N = Ha^2/Re$ is the magnetic interaction parameter, whose again derivation can be found within Chapter 2. This result was later confirmed in other steady 3-D flow regimes [83, 84].

Keeping for the moment in the vein of duct conductance, conflicting results developed shortly after [82] from a team of five scientists researching linear stability in a straight duct, again employing thin conducting walls [85]. Their investigation mirrored the conditions set out in [68]. Employing the assumption of an asymptotic profile as Ha tended to infinity, Ting et al. calculated a critical Reynolds number $Re_{cr} = 313$, which is ten times lower than the experimental result [82]. The contradiction came from newly observed instabilities in the side wall jets, not noticed in previous investigations due to the instabilities being very weak in both size and amplitude. A DNS investigation was later undertaken for $Ha = 1200$ which resulted in confirming the presence of the new instabilities, they were later named Ting-Walker vortices (TW) [86].

At the turn of the millennium, increased computer power enabled more advanced modelling techniques, thus expanding investigations into MHD flows. Large eddy simulation (LES) were developed to simulate difficult MHD flow problems at high fluid velocities [87-89]. This was not however without difficulty, as the applicability of LES is limited by the underlying assumptions and approximations. There are no such issues in Direct Numerical Simulation (DNS). Due to the controllable accuracy of DNS, it has been the preferred method

of investigation in many fluid flow problems [90, 94]. Although DNS limits the range of accessible parameters, it can produce more accurate and reliable results when adequate numerical resolution is used [95, 98]. With the increased numerical resolution, instabilities could now be observed in the flow [99] and investigations into already known instabilities and boundary layers [100, 101] could be extended and confirmed.

It has to be noted that MHD studies into the transition to turbulence are still in progress and new flow regimes are emerging in which high velocity side wall jets detaching themselves from the duct wall at, $Ha = 200$ are observed [102]. In Ref. [102] it was observed that for a duct wall conductance ratio of $c = 0.5$, the mean velocity profile demonstrated thicker jets of lower magnitude as Re was initially kept high and then reduced.

It can be deduced from this introduction that most studies into MHD flow instabilities have been performed on either fully insulating or fully conducting ducts. Little attention has been given to the duct conductance ratios set out in [42, 43] until recently. In fact there are only two known studies, which include a linear stability analysis of Hunt's flow that demonstrates long streaks in the flow regime, beginning in the core of the flow and spreading out towards the side walls [103]. At $Ha > 50$, TW vortices are observed again at $Re_{cr} = 121$. The second and most recent study investigated a toroidal duct orientation [104], at $Ha = 260$, observing at high Re, i.e. $Re > 10000$ strong turbulent fluctuation near the Hartmann layer.

These two most recent studies aside, the present study is the very first investigation, through the use of DNS, into the transition to turbulence in Hunt's flow at $Ha = 100, 200, 300, 800, 2{,}000$ & $4{,}000$ with $100 \leq Re \leq 20{,}000$.

The main aim of this study is to investigate, by means of DNS, transition to turbulence in MHD duct flows. It is of particular interest to determine the thickness of the side wall jets in terms of the Reynolds number (*Re*), Hartmann number (*Ha*) and interaction parameter (*N*). It is interesting to see whether the thickness of the side wall jets differs from earlier results found in [42, 82]. For the results to be comparable, the following parameter ranges $100 < Ha < 1000$ and $500 < Re < 10000$ have to be investigated

The transition from laminar to a turbulent MHD flow regime is expected to be marked by a sharp increase in the perturbations of energy and this phenomenon will be further studied. It would also be interesting to investigate what physical processes cause jets to detach from the side walls, as this is yet to be determined. In order for liquid metal blankets to be seriously

considered as the cooling system for fusion reactors, heat and mass transfer is of vital importance; therefore a turbulent flow within the duct is of great importance, as it determines the mixing of the fluid. It would therefore be advantageous to determine within the context of this study if electromagnetic forces supress turbulence in the core of the duct, thus laminarizing the flow within this region. If laminarization within the core is determined, this could affect the practical application of Hunt's flow as a liquid metal blanket.

2. Fluid dynamics.

2.1. Governing Equations.

Fluid dynamics is a branch of mechanics which studies how liquids and gases flow. Mathematically fluid flow is governed by partial differential equations (PDE) which usually can only be solved numerically using Finite Difference (FD), Finite Element (FE), Finite Volume (FV) and other methods. The FD is based upon a Taylor series expansion, thus relatively straight forward, but FE and FV are more mathematically involved. In this work, neither the FE nor FV were employed, so will therefore not be explained in greater content. This said, to aid in some of the derivations of hydrodynamic flow equations, FV will be employed from time to time.

Fluid flow is completely determined by the distribution of its velocity $\boldsymbol{u} = (\boldsymbol{x}, t)$, pressure $P(\boldsymbol{x}, t)$ and density $\rho(\boldsymbol{x}, t)$, which all are functions of time t, and spatial co-ordinates $\boldsymbol{x} = (x_1, x_2, x_3) = (x, y, z)$. Equations governing fluid flow are built upon certain mathematical and physical principles which will be discussed in the following.

Conservation of Mass

Generically, when we refer to a system, we are referring to identifiable matter and as such, with the system being able change from one state to another. Therefore in order to mathematically describe the conservation of a certain quantity in the system, we use a fixed control volume *V*. Expressing this in differential form results in:

$$\int_V \frac{\partial \rho}{\partial t} dV = \frac{\partial \rho}{\partial t}\, dx\, dy\, dz \tag{2.1}$$

By considering a fluid with density ρ, flowing out of an arbitrary volume *V*, the total mass of the fluid is $\int \rho dV$. The mass flux flowing through the surface $\boldsymbol{S}$, which bounds the volume *V*, per unit time *t*, is $\oint \rho \boldsymbol{u} \cdot d\boldsymbol{S}$. Here $d\boldsymbol{S}$ denotes the vector whose magnitude is equal to the

surface element, pointing in the outward normal direction. In order for the mass of the fluid to be conserved, as matter cannot be created or destroyed, we obtain:

$$\frac{\partial}{\partial t}\int_V \rho dV = -\oint \rho \boldsymbol{u} \cdot d\boldsymbol{S} \tag{2.2}$$

Due to the fact that this must hold for every volume *V*, by applying Gauss's theorem, i.e.$\int \boldsymbol{V} \cdot ds = \int \nabla \cdot \boldsymbol{V} dV$, after a little manipulation, in addition to neglecting the integrand due to the boundaries being the same, we have the more familiar conservation of mass equation, in compact vector form:

$$\frac{\partial \rho}{\partial t} + \boldsymbol{\nabla} \cdot (\rho \boldsymbol{u}) = 0 \tag{2.3}$$

At this point, it would be useful to demonstrate incompressibility, as this property is used throughout the present investigation. Therefore the term *incompressible fluid* describes the negligible changes in the density of the fluid, irrelevant whether it is steady or unsteady, thus $\frac{\partial \rho}{\partial t} = 0$. Therefore for the conservation of mass equation, we have:

$$\int_V \frac{\partial \rho}{\partial t} dV = 0 \tag{2.4}$$

Then due the constancy of density, the velocity field is solenoidal, i.e. divergence free at all points. This leads to the more familiar form of the incompressible condition:

$$\nabla \cdot \boldsymbol{u} = 0 \tag{2.5}$$

Conservation of Momentum

In order to fully understand the derivation of this most important law, a congenial initial starting point would be to use Newton's Second Law, which states that force is equal to the change in momentum of a system. Therefore by considering an arbitrary mass of fluid, we can write its change of momentum as

$$\boldsymbol{F} = \frac{d}{dt}\int_V \rho \boldsymbol{u} dV \tag{2.6}$$

If we develop the right hand side of the equation we obtain:

$$\frac{d}{dt}\int_V \rho \boldsymbol{u} dV = \int_V \left(\rho \frac{d}{dt}\boldsymbol{u} + \boldsymbol{u}\frac{d}{dt}\rho + (\rho \boldsymbol{u})\boldsymbol{\nabla}\cdot\boldsymbol{u}\right) dV \tag{2.7}$$

As the time derivative can be decomposed into expressions which only involved partial derivatives by using the chain rule and adopting (2.3), it can be demonstrated that the second and third terms on the right hand side of (2.7) cancel each other out. The total time derivative of the first term in (2.7) gives.

$$\frac{d}{dt}\int_V \rho \boldsymbol{u} dV = \int_V \left(\rho \frac{\partial \boldsymbol{u}}{\partial t} + \rho \boldsymbol{u}\cdot\nabla\boldsymbol{u}\right) dV \tag{2.8}$$

Subsequently, $\boldsymbol{F}$ through this observation can be decomposed between two classes of forces **f,** these are body forces, denoted as $\boldsymbol{f_b}$and surface forces, denoted as $\boldsymbol{f_s}$ which are applied to the volume of fluid. $\boldsymbol{f_b}$ act directly on the volumetric mass of the fluid, examples of such being electric, magnetic and gravitational forces. Conversely, $\boldsymbol{f}_s$ act directly on the surface of the fluid element, producing shear and normal stresses; both forces are dependent on the velocity of the medium in the $x, y, \& z$ direction. They are also the sum of hydrostatic pressure and viscous stresses: it is worth writing the total surface force on the mass of fluid as the surface

integral of stress tensor $\boldsymbol{\tau_{ij}}$, by implementing the stresses into matrix form, it will result in the stress tensor σ_{ij}.

$$\int_n \boldsymbol{f}_s dV = \oint_{\partial n} \tau_{ij} \cdot d\boldsymbol{S} \tag{2.9}$$

By applying Gauss's theorem, similar to the way we did in (2.2), it results in

$$\rho\left(\frac{\partial \boldsymbol{u}}{\partial t} + \boldsymbol{u} \cdot \nabla \boldsymbol{u}\right) = -\nabla \cdot \tau_{ij} + \boldsymbol{f_b} \tag{2.10}$$

The tensor τ_{ij} is required to be symmetric and as a resting fluid mass the tensor is also diagonal and isotropic, i.e. $\tau_{ij} = -p\delta_{ij}$, where p and δ_{ij} are the thermodynamic pressure and the unit tensor respectively, this however is not the case for a fluid mass in motion. We can however split τ_{ij} into a multiple of δ_{ij} and a remainder, i.e. $\tau_{ij} = -p\delta_{ij} + \tau^{*}_{ij}$, where p is the normal means stress.

It follows then that τ^{*}_{ij} is a tensor with zero trace. In addition, if we assume that it is an isotropic, linear function of the velocity gradient tensor, then τ^{*}_{ij} is constrained further and in general form can be written as:

$$\tau^{*}_{ij} = \gamma\left(\nabla \boldsymbol{u} + \left(\nabla \boldsymbol{u}\right)^{T} - \frac{2}{3}(\nabla \cdot \boldsymbol{u})\right)\delta_{ij}\Big) \tag{2.11}$$

Here γ is the dynamic viscosity. For incompressible flows, the last term on the right hand side of (2.11) is zero, thus leaving;

$$\tau^{*}_{ij} = \gamma(\nabla \boldsymbol{u} + (\nabla \boldsymbol{u})^{T}) \tag{2.12}$$

By defining $v = \gamma/\rho$ as the kinematic viscosity, we can eventually obtain the momentum equation, better known as the Navier Stokes Equation:

$$\rho\left(\frac{\partial \boldsymbol{u}}{\partial t} + \boldsymbol{u}\cdot\nabla\boldsymbol{u}\right) = -\nabla p + \rho v\nabla^2\boldsymbol{u} + \boldsymbol{f}_b \tag{2.13}$$

2.2. Magnetohydrodynamic Governing Equations.

Having shown the fundamental equations governing hydrodynamic flow, we now progress and investigate the effects magnetic fields have when imposed onto a conducting fluid. Imposing a magnetic field onto a conducting fluid flow alters the fluids dynamics. According to Faraday's law, electrical currents appear in the fluid, which subsequently according to Ampere's law, induces a magnetic field. The induced and applied magnetic field interact with the electrical currents producing a Lorentz force.

Electromagnetism

Electromagnetism fundamentally describes the electromagnetic force which occurs between electrically charged particles. It has been observed that a certain charge q, moving with velocity $\boldsymbol{u}$, within an electric field $\boldsymbol{E}$ or magnetic field $\boldsymbol{B}$ will be subjected to a Lorentz force.

A Lorentz force concerns itself with the forces generated when electrical charges are in motion. The resulting force is proportional to the velocity of a moving charge within the fluid, which additionally points perpendicular to the velocity. This scenario demonstrates that the generated force depends on a cross product for investigation. A magnetic field $\boldsymbol{B}$ generated from the electrical current, in simplistic terms wraps itself around the current in a circular motion. The force as it circulates can be defined as the sum of Coulomb and Lorentz forces:

$$\boldsymbol{F}_L = q(\boldsymbol{E} + \boldsymbol{u}\times\boldsymbol{B}) \tag{2.14}$$

Where q is the electrical charge $\boldsymbol{u}$, $\boldsymbol{E}$ and $\boldsymbol{B}$ are the velocity, electric and magnetic fields respectively. By summing over an arbitrary volume of fluid, $\sum q$, we can introduce the charge $\boldsymbol{J}$ and electrical current density ρ_e :

$$\int \rho_e dV = \sum q$$
$$\int \boldsymbol{J} dV = \sum qu \tag{2.15}$$

By incorporating the summations above into (2.14), we can write the density of the Lorentz force as:

$$\boldsymbol{F}_L = \rho_e \boldsymbol{E} + \boldsymbol{J} \times \boldsymbol{B} \tag{2.16}$$

However, we can neglect the first term on the right hand side because when operating in a liquid metal environment, which we are in the context of this research, we can make the assumption that $\rho_e$is neutral, therefore this results in (2.16) to be reduced to:

$$\boldsymbol{F}_L = \boldsymbol{J} \times \boldsymbol{B} \tag{2.17}$$

We have to note that charge is a conserved property and having introduced the quantities above (2.15), we are able to take the divergence of (2.22), noting that $\boldsymbol{\nabla} \cdot \boldsymbol{\nabla} \times \boldsymbol{B} = 0$, divide through by $\mu_0$and finally substitute in (2.19). This allows us to show a similar equation for a charge conservation equation:

$$\frac{\partial}{\partial t} \rho_e + \boldsymbol{\nabla} \cdot \boldsymbol{J} = 0 \tag{2.18}$$

Before progressing, it would be sagacious to define Maxwell's equations as a separate entity. The Lorentz force (2.16) alone is not sufficient to determine the motion of the flow. Knowing

that the electrical current depends on the magnetic field, which in turn depends on the velocity, we are going to employ Maxwell equations to a close system of equation.

2.3. Maxwell's Equations.

Maxwell's four equations describe how the electric $\boldsymbol{E}$ and magnetic field $\boldsymbol{B}$ interact for any given specified matter. Underneath each of Maxwell's equation will be a more detailed explanation, describing each separate law and its inherent parts. The equations are:

$$Gauss's\ Law \qquad \boldsymbol{\nabla} \cdot \boldsymbol{E} = \epsilon_0^{-1} \rho_e, \tag{2.19}$$

$$Gauss's\ Law\ of\ Magnetism \qquad \boldsymbol{\nabla} \cdot \boldsymbol{B} = 0\ , \tag{2.20}$$

$$Faraday's\ Law \qquad \boldsymbol{\nabla} \times \boldsymbol{E} + \frac{\partial}{\partial t}\boldsymbol{B} = 0\ , \tag{2.21}$$

$$Ampere's\ \ Law \qquad \boldsymbol{\nabla} \times \boldsymbol{B} = \mu_0 \left(\boldsymbol{J} + \epsilon_0 \frac{\partial}{\partial t} \boldsymbol{E} \right)\ , \tag{2.22}$$

where ϵ_0, μ_0 represent the permittivity and permeability of free space respectively. If we were to take the divergence of Ampere's law (2.22) and employ Gauss's law (2.19), we would return to (2.18). Separately, by taking the divergence of Faraday's law (2.21), we eventually arrive, through simple manipulation, at Gauss's law of magnetism (2,20). Due to the unknowns and constraints in Maxwell's equations, to which there are eight and ten respectively, we need an additional relationship linking the current and electric field. This relationship is given by Ohm's law. This law states that reason for isotropic stationary fluid, current density is proportional to electric fields, which can be expressed as:

$$\boldsymbol{J} = \sigma \boldsymbol{E} \tag{2.23}$$

By also making the assumption that the motion of the moving medium is much slower than the speed of light, which was discussed earlier in this section, the approximation of Lorentz transformation reduces to $\rightarrow \boldsymbol{E} + \boldsymbol{u} \times \boldsymbol{B}$ **,** which results in:

$$\boldsymbol{J} = \sigma(\boldsymbol{E} + \boldsymbol{u} \times \boldsymbol{B}) \tag{2.24}$$

By re-arranging (2.18) and substituting it back into the divergence of (2.24) we can substitute in (2.19) and re-arrange to give us:

$$\frac{\partial}{\partial t}\rho_e + \frac{\sigma}{\epsilon_0}\rho_e = -\sigma \boldsymbol{\nabla} \cdot (\boldsymbol{u} \times \boldsymbol{B}) \tag{2.25}$$

Also previous considerations within this explanation can also be used to demonstrate that the right hand side of (2.22) can be neglected, as it only becomes important when the medium is moving at a velocity approaching the speed of light. Therefore for much lower velocities we can approximate (2.22) as:

$$\boldsymbol{\nabla} \times \boldsymbol{B} = \mu_0 \boldsymbol{J} \tag{2.26}$$

By taking the divergence of (2.26) results in the reduced and modified charge conservation equation:

$$\boldsymbol{\nabla} \cdot \boldsymbol{J} = 0 \tag{2.27}$$

Induction Equation

The induction equation is a linear partial differential equation for **B**, describing the evolution of the magnetic field with respects to time, in the domain occupied by the conducting medium. For $Re_m \ll 1$, the induction field will be dominated by magnetic diffusion. With the help of Maxwell's equations and Ohm's law, the induction equation can be simply derived.

By taking the curl of (2.24) and re-arranging (2.21) we can now substitute (2.21) into (2.24). We can now take the curl of (2.26) and divide by μ_0. Taking this result we substitute this back into our new (2.24). By noting that $\boldsymbol{\nabla} \times \boldsymbol{\nabla} \times \boldsymbol{B} = -\boldsymbol{\nabla^2 B}$ we eventually arrive after dividing through by σ and a little manipulation at:

$$\frac{\partial}{\partial t}\boldsymbol{B} = \boldsymbol{\nabla} \times (\boldsymbol{u} \times \boldsymbol{B}) + (\sigma\mu)^{-1}\boldsymbol{\nabla^2 B} \tag{2.28}$$

By using the fact that both $\boldsymbol{u}$ and $\boldsymbol{B}$ are solenoidal, we can finally write the more familiar form of the induction equation with incompressibility condition as:

$$\frac{\partial}{\partial t}\boldsymbol{B} + (\boldsymbol{u} \cdot \nabla)\boldsymbol{B} = \frac{1}{\mu\sigma}\nabla^2\boldsymbol{B} + (\boldsymbol{B} \cdot \nabla)\boldsymbol{u} \tag{2.29}$$

Dimensionless Form

Dimensionless numbers are found in various fields including mathematics, engineering and physics. They define expressions which are unit-less. When dimensionless numbers are used within physics, they aid in the simplification of a problem which involves multiple physical characteristics.

$$\boldsymbol{u} = U\boldsymbol{u} \quad \text{(a)}$$

$$\boldsymbol{\nabla} = L^{-1}\boldsymbol{\nabla} \quad \text{(b)}$$

$$t = LU^{-1}t \quad \text{(c)}$$

$$\boldsymbol{f} = U^2L^{-1}\boldsymbol{f} \quad \text{(d)}$$

$$\boldsymbol{B} = B_0\boldsymbol{B} \quad \text{(e)}$$

$$\boldsymbol{J} = \sigma U B_0\,\boldsymbol{J} \quad \text{(f)}$$

$$p = \sigma L B_0^2 U p \quad \text{(g)}$$

Note that in this thesis the dimensionless quantities are denoted with the same letters as the dimensional ones.

Coupling Maxwell's and Navier-Stokes Equations

Now we have all the equations that are needed to describe an incompressible conducting fluid in a magnetic field. The governing equations which describe this are (2.5), (2.13) and (2.29). Additionally, (2.20) is also required as the induction equation (2.29), only guarantees the divergence free characteristic of $\boldsymbol{B}$, if it is initially solenoidal; therefore giving;

$$\frac{\partial \boldsymbol{u}}{\partial t} + \mathbf{u} \cdot \nabla \mathbf{u} = -\rho^{-1} \nabla p + v \nabla^2 \mathbf{u} + \rho^{-1} \mathbf{J} \times \mathbf{B} + \rho^{-1} \mathbf{f}$$

$$\frac{\partial \boldsymbol{B}}{\partial t} + \mathbf{u} \cdot \nabla \mathbf{B} = \mathbf{B} \cdot \nabla \mathbf{u} + \frac{1}{\mu \sigma} \nabla^2 \mathbf{B}$$

$$\nabla \cdot \boldsymbol{u} = 0$$

$$\nabla \cdot \boldsymbol{B} = 0$$

If we non-dimensionalize the above equations via the parameters set out in the dimensionless form we finally arrive at;

$$\frac{\partial \boldsymbol{u}}{\partial t} + \mathbf{u} \cdot \nabla \mathbf{u} = -\nabla p + Re^{-1} \nabla^2 \mathbf{u} + N \mathbf{J} \times \mathbf{B} \tag{2.30}$$

$$\frac{\partial \boldsymbol{B}}{\partial t} + \mathbf{u} \cdot \nabla \mathbf{B} = \mathrm{B} \cdot \nabla \mathbf{u} + R_m^{-1} \nabla^2 \mathbf{B} \tag{2.31}$$

$$\nabla \cdot \boldsymbol{u} = 0 \tag{2.32}$$

$$\nabla \cdot \boldsymbol{B} = 0 \tag{2.33}$$

The dimensionless parameters in the equations above are, Reynolds Number Re, the Magnetic Reynolds Number R_m and the interaction parameter N. Below are definitions of these three parameters including, the Hartmann number Ha.

Reynolds Number

The Reynolds number is defined as

$$Re = \frac{UL}{v}, \tag{2.34}$$

where U, L and v represent the fluid velocity, typical length scale and kinematic viscosity respectively. It is a dimensionless parameter which generally characterizes the fluid flow. It can be understood as the ratio of inertial forces to viscous forces. Reynolds number largely determines the character of fluid flow.

Laminar flow occurs at a relatively low Reynolds number, $Re \ll 1000$, where viscous forces dominate the fluid dynamics, leading to a smooth and steady fluid flow regime.

Turbulent flow occurs at a relatively high Reynolds number, $Re \gg 1000$, where fluid flow is dominated by inertial forces. In turbulent flows the transfer of energy from larger scale vortices down to smaller scale vortices occurs. In many practical applications *Re* values can reach in excess of $10^4 - 10^6$, but within the scope of this investigation we will not be considering fluid flow regimes of this *Re* magnitude. In this study we consider fluid flow with *Re* between $10^4 - 10^5$.

Magnetic Reynolds Number

Magnetic Reynolds number characterizes the strength of magnetic advection relative to that of magnetic diffusion within (2.29), thus being defined as:

$$Re_m = \frac{UL}{(\mu\sigma)^{-1}} \tag{2.35}$$

The main difference between $Re\ and\ Re_m$ is that Re relates to the fluid velocity itself, while Re_m relates to the magnetic field induced within a MHD fluid flow. When $Re_m \ll 1$, the induced magnetic field is usually unimportant and the field inside the fluid is the same as that generated by the external magnets. When $Re_m \gg 1$, inductive effects dominate and the magnetic field lines are transported along with the flow, almost frozen within the fluid,

Hartmann Number

The Hartmann number Ha is a dimensionless parameter associated with the ratio of electromagnetic forces to viscous forces:

$$Ha^2 = \frac{Electromagnetic\ forces}{Viscous\ forces} \approx \frac{\boldsymbol{J} \times \boldsymbol{B}}{v\boldsymbol{\nabla^2 u}}$$

This can also be expressed in a more familiar form

$$Ha = \boldsymbol{B}L\sqrt{\frac{\sigma}{\rho v}} = \sqrt{N\ Re}, \tag{2.36}$$

where σ represents electrical conductivity

At high values of Ha, the electromagnetic forces dominate the flow. In thermo nuclear fusion liquid metal blankets, Ha can reach levels in excess of $Ha = 10^4$. In subsequent chapters, we will demonstrate the effects that different Ha parameters have on a flow within a duct.

Interaction Parameter

The magnetic interaction parameter, also referred to as Stuarts number, is defined as the ratio of the electromagnetic forces to inertial forces.

$$N = \frac{Elecromagnetic\ forces}{Inertial\ Forces} \approx \frac{\boldsymbol{J} \times \boldsymbol{B}/\rho}{(\boldsymbol{u} \cdot \nabla)\mathbf{u}} \tag{2.37}$$

$$= \frac{Ha^2}{Re} \approx \frac{\sigma L \boldsymbol{B_0^2}}{\rho \mu}$$

When $N \ll 1$, the magnetic field has a weak effect on the flow due to the non-linear inertial force dominating over the Lorentz force. Conversely, when $N \gg 1$, the Lorentz force is much greater in magnitude than the inertial forces, making the effect of the magnetic field much more significant on the behaviour of the flow.

Summary

We have now derived all the equations and parameters necessary to describe an incompressible, viscous fluid subjected to a magnetic field. The equations which govern MHD are a combination of (2.30)-(2.33). As is apparent from this section, there are mainly only three non-dimensional parameters which characterises MHD flow $Ha, N\ and\ Re_m$. Re characterizes the ratio of the non-linear inertial and viscous forces. Therefore, if this parameter is small, the fluctuations within the fluid are damped by the viscous forces, resulting in a laminar flow regime. Conversely the opposite occurs if *Re* is high, as large range spatial and temporal scales develop, this is known as turbulence and the transition to which is the main topic this thesis.

2.4. Quasi static approximation.

In this section we derive what is known as the quasi static approximation, which is commonly applicable for liquid metal flows and will be used in this study. In previous subsections we

demonstrated that the induction equation contains only one dimensionless quantity, the magnetic Reynolds number Re_m. When Re_m is small, as it is in most cases for industrial applications, the equations which govern the flow can be simplified. Therefore, in order for us to enable this simplification we must first separate the externally applied magnetic field $\boldsymbol{B}$, from the induced magnetic field $\boldsymbol{b}$, the induction equation is shown below:

$$\frac{\partial}{\partial t}\boldsymbol{b} = -(\boldsymbol{u}\cdot\boldsymbol{\nabla})\boldsymbol{b} + \big((\boldsymbol{B}+\boldsymbol{b})\cdot\boldsymbol{\nabla}\big)\boldsymbol{u} + \frac{1}{\mu\sigma}\nabla^2\boldsymbol{b} \tag{2.38}$$

When dealing with small Re_m, we can justify the neglecting the magnetic field with respect to the diffusive terms via the following order of magnitude estimates:

$$(\boldsymbol{u}\cdot\boldsymbol{\nabla})\boldsymbol{b}\sim\frac{Ub}{L},\quad (\boldsymbol{b}\cdot\boldsymbol{\nabla})\boldsymbol{u}\sim\frac{Ub}{L},\quad \frac{1}{\mu\sigma}\nabla^2\boldsymbol{b}\sim\frac{(\mu\sigma)^{-1}b}{L^2} \tag{2.39}$$

$$\frac{(\boldsymbol{u}\cdot\nabla)\boldsymbol{b}}{(\mu\sigma)^{-1}\boldsymbol{\nabla^2 b}} = \frac{(\boldsymbol{b}\cdot\nabla)\boldsymbol{u}}{(\mu\sigma)^{-1}\boldsymbol{\nabla^2 b}} \sim R_m \ll 1 \tag{2.40}$$

This enables us to reduce the induction equation to:

$$\frac{\partial \boldsymbol{b}}{\partial t} = (\boldsymbol{B}\cdot\boldsymbol{\nabla})\boldsymbol{u} + \frac{1}{\mu\sigma}\boldsymbol{\nabla^2 b} \tag{2.41}$$

Assuming that the magnetic fields very quickly adapt to the velocity field, we can neglect the time derivative term and thus obtain Poisson equation:

$$\frac{1}{\mu\sigma}\boldsymbol{\nabla^2 b} + (\boldsymbol{B}\cdot\boldsymbol{\nabla})\boldsymbol{u} = 0 \tag{2.42}$$

Alternatively, we can now employ Ohm's law to formulate the quasi static approximations. First we separate the inherent electromagnetic quantities $\boldsymbol{E}$, $\boldsymbol{J}$ and $\boldsymbol{B}$ into the mean part $\boldsymbol{E_0}$,$\boldsymbol{J_0}$

and $\boldsymbol{B}$, and perturbations $\boldsymbol{E}'$,$\boldsymbol{J}'$ and $\mathbf{b}$ respectively. The mean and perturbation quantities are governed by;

$$\begin{aligned} \boldsymbol{\nabla} \times \boldsymbol{E_0} &= \mathbf{0} \qquad \boldsymbol{J_0} = \sigma \boldsymbol{E}_0 \\ \boldsymbol{\nabla} \times \boldsymbol{E}' &= -\frac{\partial \boldsymbol{b}}{\partial t} \qquad \boldsymbol{J}' = \sigma(\boldsymbol{E}' + \boldsymbol{u} \times \boldsymbol{B}) \end{aligned} \tag{2.43}$$

If we neglect the electric field perturbations due to Faraday's equation, $E' \sim Ub$, and thus Ohm's law becomes:

$$\boldsymbol{J} = \boldsymbol{J_0} + \boldsymbol{J}' = \sigma(\boldsymbol{E}_0 + \boldsymbol{u} \times \boldsymbol{B}) \tag{2.44}$$

Since $\boldsymbol{E_0}$ is irrotational, (2.44) can be written as the gradient of the electric potential ϕ:

$$\boldsymbol{J} = \sigma(-\boldsymbol{\nabla}\phi + \boldsymbol{u} \times \boldsymbol{B}) \tag{2.45}$$

At this point we have all the necessary information to evaluate $\boldsymbol{F} = \boldsymbol{j} \times \boldsymbol{B}$ within the momentum balance, since (2.27), providing the Poisson equation, linking ϕ to $\boldsymbol{u}$ *and* $\boldsymbol{B}$. By taking the divergence of (2.45), and using (2.27) we obtain:

$$\boldsymbol{\nabla}^2 \phi = \boldsymbol{\nabla} \cdot (\boldsymbol{u} \times \boldsymbol{B}) \tag{2.46}$$

We can now write the full system of non-dimensional quasi static MHD equations:

$$\boldsymbol{\nabla} \cdot \boldsymbol{u} = 0 \tag{2.47}$$

$$\frac{\partial}{\partial t}\boldsymbol{u} + (\boldsymbol{u} \cdot \boldsymbol{\nabla})\boldsymbol{u} = -\boldsymbol{\nabla} p + \frac{1}{Re}\boldsymbol{\nabla}^2 \boldsymbol{u} + N(-\boldsymbol{\nabla}\phi + \boldsymbol{u} \times \boldsymbol{B}) \times \boldsymbol{B} \tag{2.48}$$

$$\nabla^2 \phi = \nabla \cdot (\boldsymbol{u} \times \boldsymbol{B}) \tag{2.49}$$

If quasi-static approximation is applied to a finite domain, the above equation will be beneficial as it only requires one Poisson equation to be solved instead of three in other quasi static formulations. Additionally the quasi static approximation assumes that the induction is dominated by the diffusion. By assuming this, it allows the magnetic field to behave as it would in a motionless fluid, thus the fluctuations in **B** are negligible. Moreover, as the diffusion of the magnetic field is small with respect to the time scale of the fluid motion, the magnetic field adapts itself to the configuration of the fluid. We can therefore assume that concerning the time scale of the fluids motion, that the fluctuations of the magnetic field are time dependent. The most advantageous issue concerning the quasi-static approximation is that it relieves the use of the induction equation.

2.5. Boundary conditions.

The Boundary conditions (BC) ensure that the mathematical problems at hand are well-posed and have uniquely defined solutions. The BC which were integrated into the Fortran code used within the context of this work were Dirichlet boundary conditions along the conducting walls $\phi_{wall} = const$, which specify the values a solution needs along the boundary of the domain. In addition to this, Neumann boundary conditions were also employed along the insulating walls $\frac{\partial \phi}{\partial n} = 0$, this particular BC specifies the value of the derivative a solution is to take on the boundary of the domain, defining the electric potential at the fluid/wall interface. In effect, allowing the quasi static equation derived in the previous section to be fully determined. As this investigation dealt with the effects of fluid flow within a stationary duct, no derivations will proceed for boundary walls which are transient. Therefore at a stationary wall with an outward normal unit vector $\boldsymbol{n}$, we state that BC are satisfied by the no slip conditions:

$$\boldsymbol{u} = 0 \quad at\ \Gamma, \tag{2.50}$$

where Γ is a solid boundary. Due to the fact that we are dealing with an electrically conducting fluid passing through an external magnetic field, electromagnetic boundary conditions are dominated by current and electrical conductivity of the duct wall material σ_w.

Insulating walls

If the duct walls are insulating ($\sigma_w = 0$), no electrical current can penetrate them. Therefore, the normal component of the current density in the fluid at such walls disappears:

$$\boldsymbol{J} \cdot \boldsymbol{n} = J_n = 0, \quad at\ \Gamma \tag{2.51}$$

which can be rendered in a condition on ϕ in expressing Ohm's law at the solid boundary walls, taking into account (2.50);

$$\boldsymbol{J_n} = -\sigma \frac{\partial \phi}{\partial n} = 0 \rightarrow \frac{\partial \phi}{\partial n} = 0 \quad at\ \Gamma. \tag{2.52}$$

Perfectly conducting walls

The electrical potential of a perfectly conducting wall $\sigma_w = \infty$ has to be uniform in order to keep the electrical current to a conditioned value. The potential at the wall can be set to zero:

$$\phi = 0 \quad at\ \Gamma. \tag{2.53}$$

Conducting Walls

If the walls have a finite conductivity, the electrical current flowing into the duct wall has to be coupled to that in the outer bounded domain. This is determined by the continuity condition at Γ. Allowing also for thin conducting walls, the thickness of which we will denote as t_w , a simpler boundary condition can be drawn in a quasi-two-dimensional way. In order

to fully comprehend this discharge, we can draw upon the charge conservation equation in the form:

$$\frac{\partial j_n}{\partial n} = -\nabla_\tau \cdot \boldsymbol{j_\tau}, \tag{2.54}$$

where τ represents the tangential co-ordinate to the thin duct wall, giving $\boldsymbol{j} = \boldsymbol{j_\tau} + j_n \boldsymbol{n}$ or $\nabla = \nabla_\tau + \boldsymbol{n}\frac{\partial}{\partial n}$. By applying Ohm's Law and taking into account that the electric potential does vary across the thin wall of the domain and integrating, we have the relationship:

$$-\boldsymbol{J} \cdot \boldsymbol{n} = \sigma \frac{\partial \phi}{\partial n} = \boldsymbol{\nabla}_\tau \cdot (\sigma_w t_w \boldsymbol{\nabla}_\tau \phi_w) \quad \text{on} \quad \Gamma, \tag{2.55}$$

where $\boldsymbol{n}, \phi$ and t_w represent outward normal to the wall, electric/ fluid interface and wall thickness respectively. If there is no contact resistance we can write:

$$-\frac{\partial \phi}{\partial n} = \boldsymbol{\nabla}_\tau \cdot (c \boldsymbol{\nabla}_\tau \phi) \qquad \text{on } \Gamma, \tag{2.56}$$

where c is the wall conductance ration and is expressed as:

$$c = \frac{\sigma_w t_w}{\sigma L}. \tag{2.57}$$

Kinetic energy

The density for kinetic energy of a flow enclosed within a domain *V* without a magnetic field can be defined as;

$$e = \frac{1}{V}\int \frac{u_i u_i}{2} dV \tag{2.58}$$

The kinetic energy development over time can be calculated by multiplying (2.58) by $\boldsymbol{u_i}$, but in order to achieve this it is advantageous to convert (2.58) into tensor notation:

$$\rho \frac{\partial}{\partial t}\frac{u_i u_i}{2} + \rho u_i u_j \nabla_j u_i = u_i \partial i \rho + \mu u_i \partial_j \partial_j u_i + \rho u_i g_i$$

By integrating over the volume *V* and applying Gauss Law, we can remove the 1st, 2nd and 3rd term on the right as they equate to zero due to stationary boundaries, which leaves:

$$\rho \frac{\partial}{\partial t}\int \frac{u_i u_i}{2}\frac{\partial V}{V} = -2\mu \int S_{ij} S_{ij} \frac{\partial V}{V} + \rho \int u_i g_i \frac{\partial V}{V}$$

Finally, dividing through by ρ gives the kinetic energy in tensor notation omitting any magnetic field

$$\frac{\partial}{\partial t}\int \frac{u_i u_i}{2} = -2\omega \int S_{ij} S_{ij} \frac{\partial V}{V} + \int u_i g_i \frac{\partial V}{V}$$

Boundary Layers

We will now discuss the effect an externally applied magnetic field has on the boundary layers in a laminar channel flow. Once this particular case has been studied, we progress further to a flow where an additional pair of walls are added, thus changing the channel to a duct. The reason for explaining the two different flow regimes in this manner is to provide a more comprehensive, rounded view in which to compare the magnetic effects in different media.

We begin by considering a channel with walls $z = \pm 1$, which are perpendicular to the externally applied magnetic field, here defined as $\boldsymbol{B} = b\mathbf{1}_z$ and taking the flow direction as *x*, we can omit all derivatives with respect to *x*, except for the pressure gradient. Moreover, we cannot leave aside the span-wise induced electric field as the flow is homogeneous in the *y*-direction, therefore this gives $\mathbf{u} = u(z)\mathbf{1}_x$, where u and ϕ submit to:

$$-\frac{\partial p}{\partial x} + \rho v \frac{\partial^2 u}{\partial z^2} + \sigma b\left(\frac{\partial \phi}{\partial y} - bu\right) = 0 \tag{2.59}$$

$$\frac{\partial^2 \phi}{\partial z^2} = 0 \tag{2.60}$$

At $z = \pm 1$ the boundary condition for the velocity of the fluid is $u = 0$, we can also further state that the electric potential is continuous along the fluid-wall interface, which leads us to:

$$u = \frac{1}{\rho v}\left(-\frac{\partial p}{\partial x} Ha^{-2} + \sigma b A\right)\left(1 - \frac{\cosh(Ha_z)}{\cosh(Ha)}\right) \tag{2.61}$$

$$\phi = Az + B \tag{2.62}$$

Within (2.62) A and B are constants of integration. The constant A is determined by the total current which is in the wall-fluid domain which integrates to zero. B on the other hand is arbitrary, which all leads to a velocity profile of:

$$u = \frac{1}{Ha}\frac{1 + c}{cHa + \tanh(Ha)}\frac{1}{\rho v}\frac{\partial p}{\partial x}\left(1 - \frac{\cosh(Ha_z)}{\cosh(Ha)}\right) \tag{2.63}$$

As *Ha* is increased, the thin exponential boundary layers, known as Hartmann Layers, decrease in thickness and scaled as Ha^{-1}. The scaling of the Hartmann Number with the fluids velocity can be understood in the following manner. With a channel of conducting walls, i.e. $\phi = 0$, the magnitude of the Lorentz force density is $\sigma u b^2$. Within a high Hartmann regime, the force dominates the core of the fluid flow, the core velocity therefore

will scale to $u \propto -\partial_x p(\sigma b^2)^{-1} \propto -\partial_x p Ha^{-2} \frac{1}{\rho v}$. If however the channel walls are electrically insulating. A span-wise electric potential gradient is induced, counteracting the effects of $\boldsymbol{u} \times \boldsymbol{B}$. The Lorentz force retards the flow within the core and accelerates the fluid within the boundary layers, thus the integral between $z = 1$ and $z = -1$ is therefore zero. In order to determine the scaling we are required to integrate the remaining terms in the momentum balance, again between $z = 1$ and $z = -1$:

$$\int_{-1}^{1} \frac{\partial p}{dx} dz = \rho v \int_{-1}^{1} \frac{\partial^2 u}{\partial z^2} dz = \rho v \left(\frac{\partial u}{\partial z}\middle| z_{=1} - \frac{\partial u}{\partial z}\middle| z_{=-1}\right) \tag{2.64}$$

It is evident from (2.64) that the pressure gradient compensates for the viscous losses at the boundaries. This is due to the fact of large viscous losses, a consequence of the steep profile of the boundary layers, making the magnitude of the velocity an order *Ha* smaller than in a Poiseuille flow for the same pressure gradient.

The geometry which depicts the present study involves a duct and therefore requires an additional pair of walls, compared to channel flow. The additional pair of boundary walls are positioned at $y = \pm 1$ and are known as side walls. Within a duct where walls are all insulating, the interaction between the fluid flow and the magnetic field drives a current in the *z* – direction, retarding the flow. A solution to this is given in [105]. In this particular regime the current lines bend at the walls and close through the Hartmann layer, due to the walls insulating properties. At the side layers, the currents are almost parallel to the magnetic field, making the Lorenz force in this region weaker. The side layers being of thickness $O\left(Ha^{-\frac{1}{2}}\right)$, similar to the channel regime with insulating walls. The magnitude of velocity is of order *Ha* smaller than in a hydrodynamic case, driven by the same pressure gradient. The ratio between the amplitudes of velocity in the side layers and that in the core scales to $O(Ha^0)$, with the core velocity itself scaling as $\frac{1}{Ha^2} \partial_x p$.

The third and final is a duct with perfectly conducting Hartmann walls and perfectly insulating side walls. By making a direct comparison to the fully insulating regime, the strength of the electrical currents can be large, forming closed loops by entering the Hartmann layers. At the side layers, the current flows parallel to the externally applied magnetic field, thus the Lorentz force is greatly reduced within this region resulting in a

much high fluids velocity compared to that within the core. The comparative amplitude between the core flow and the higher velocity fluid at the side walls scales to $O(Ha)$. As mentioned previously, as the thickness of the side layers scales to $O(Ha^{\frac{1}{2}})$ and as such we observe that at high *Ha* values the mass flow rate carried within the core is small in respect to the mass flow rate in the side layers. It has also been witnessed within this study that there is a reversed fluid flow close to the inner velocity jet region at $Ha > 100$. The reversed fluid flow has been deemed as a non-trivial phenomenon within this investigation and the influential effects that this occurrence has on the transition to turbulence will be discussed in detail with in Chapter 4.

3 Direct Numerical Simulation.

3.1. Numerical Simulation.

The fluid flow with or without magnetic field is governed by a system of Partial Differential Equations (PDE). Analytical solutions to fluid flow can only be obtained for the most basic of laminar flows. For turbulent flows, as in most cases, analytical solutions are inadequate. A complete description of a turbulent regime, where flow variables are known as a function of space and time, can only be obtained through computer modelling of the Navier-Stokes equations.

Depending on the purpose of the investigation, two widely known simulation methods can be employed for general fluid flow, Large Eddy Simulations (LES) and Reynolds Averaged Navier-Stokes (RANS). Both methods can allow fluid flow investigations at very high Re, but in order to achieve this, numerical resolution, in most cases needs to be decreased as a consequence, thus resulting in approximations to the classic flow. In this study we are attempting to look deeper into an MHD flow regimes to determine the physical process which occur as the flow transitions from laminar to turbulent. Direct Numerical Simulation (DNS), in general gives a greater degree of numerical resolution, albeit simulation times are greatly increased as flow parameters are increased. However, due to the specific physical processes under investigation, DNS was exclusively employed in this present study.

3.2. Finite difference methods.

Finite difference methods (FDM) are the dominant approach in numerical modelling. In order to approximate the derivatives of u, the x-axis is divided into intervals of h of constant or variable length. The division (grid) points along the x-axis will be denoted as x_{i-1} (preceding), x_i (central), and x_{i+1} (subsequent). If $u\ \ (x)$ is smooth, it is possible to quantify the error of approximation of $u'(x)$ through the use of Taylor's theorem

$$f(x) = f(a) + f'(x-a) + \frac{f''(a)}{2!}(x-a)^2 + \cdots + f^n\frac{(x_0)}{n!}h^n + R_n(x) \qquad (3.1)$$

We can employ the Taylor's theorem to estimate the finite difference approximation for the first derivative of a forward and backward scheme respectively:

$$f'(x_i) \approx \frac{f(x_i) - f(x_{i-1})}{h} + O(h) \tag{3.2}$$

$$f'(x_i) \approx \frac{f(x_{i+1}) - f(x_i)}{h} + O(h) \tag{3.3}$$

More accurate is the central difference approximation whose error according to Taylor series expansion is proportional to h^2:

$$f'(x_i) \approx \frac{f(x_{i+1}) - f(x_{i-1})}{2h} + O(h^2) \tag{3.4}$$

By divide through by h^2 and making $f''(x_i)$ the subject in Eq. 3.1, we arrive at the approximation of the second derivative:

$$f''(x_i) \approx \frac{f(x_{i+1}) - 2f(x_i) + f(x_{i-1})}{h^2} \tag{3.5}$$

Assuming that f is now a function of two variables x & t, we divide the domain into a uniform grid with sides $\delta x = h$ and $\delta t = k$. The co-ordinates x, t of the point P are $x = ih$ and $t = jk$, where i & j are integers. Then the value of f at P are $f(ih, jk) = f_{i,j}$. By using the forward, backward and central difference approximations respectively, we arrive at the first derivative with respects to x:

$$\frac{f_{i+1,j} - f_{i,j}}{h} + O(h) \tag{3.6}$$

$$\frac{f_{i,j} - f_{i-1,j}}{h} + O(h) \tag{3.7}$$

$$\frac{f_{i+1,j} - f_{i-1,j}}{2h} + O(h^2) \tag{3.8}$$

In addition, we can derive the first derivatives with respects to t of the forward, backward and central difference respectively:

$$\left(\frac{\partial f}{\partial t}\right)|i,j = \frac{f_{i,j+1} - f_{i,j}}{k} + O(k) \tag{3.9}$$

$$= \frac{f_{i,j} - f_{i,j-1}}{k} + O(k) \tag{3.10}$$

$$= \frac{f_{i,j+1} - f_{i,j-1}}{2k} + O(k^2) \tag{3.11}$$

The higher, second order derivatives are thus:

$$\left(\frac{\partial^2 f}{\partial x^2}\right)|i,j = \frac{f_{i+1,j} - 2f_{i,j} + f_{i-1,j}}{h^2} + O(h^2) \tag{3.12}$$

$$\left(\frac{\partial^2 f}{\partial t^2}\right)|i,j = \frac{f_{i,j+1} - 2f_{i,j} + f_{i,j-1}}{k^2} + O(k^2) \tag{3.13}$$

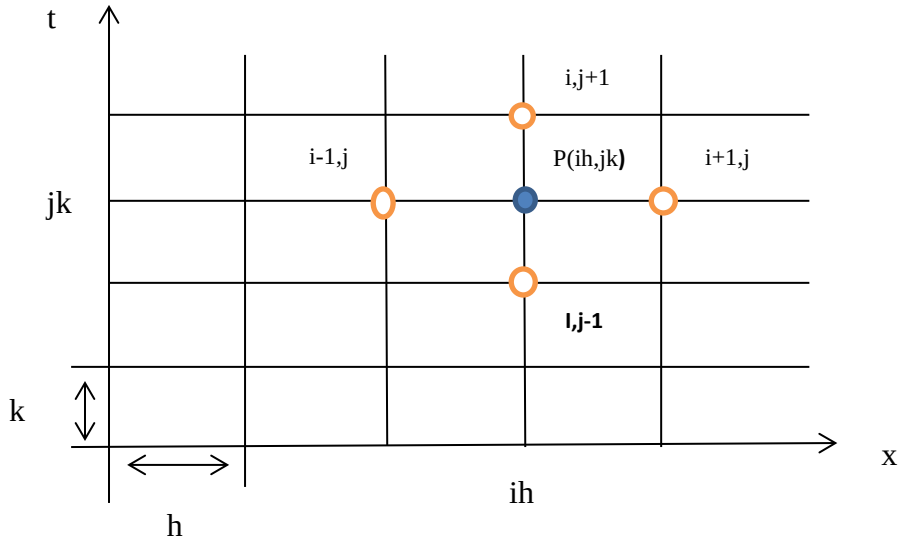

FIGURE 7. A arbitrary grid in the (x, t) plane.

3.3. Explicit and Implicit time discretization schemes.

The purpose of time discretization schemes is to solve the unsteady equations by marching in time. There is a maximum allowable time step (M_{max}) within a numerical scheme beyond which this the scheme becomes unstable and diverges. Therefore if $M > M_{max}$, the errors in the numerical scheme exponentially grow, causing divergence. The value of M_{max} will obviously depend upon the particular numerical discretization scheme used and these particular schemes are commonly referred to as either implicit or explicit schemes. The explicit scheme involves an updating procedure which is dependent on the previous time step explicitly. The implicit scheme however does not require the time advancement to be explicitly defined from the previous time step. This advantage makes the implicit scheme more attractive when dealing with fluid motion, allowing improved stability properties. An explicit method is easy to implement for parallelisation purposes and has a lower time step cost, therefore making it a good starting point for the development of numerical schemes, but conversely an explicit method requires time steps to be small in order to achieve a greater degree of stability, this is especially when the mesh size of the domain is varying strongly.

An implicit method on the other hand is much more stable over a wider range of M and constitutes excellent iterative solvers for a steady-state problem. It is for this reason why the implicit method has mainly been employed in this work. However, implicit methods are

difficult to implement when dealing with parallelization and quite often incur high time step costs. In order for the implicit method to reach a steady state, if must first go through a convergence period of the iterative solver and it is here where the accuracy and stability of the implicit method wane. This is especially so at high M as the convergence of the linear solvers deteriorates as the time step increases, mainly due to the unsteady viscous terms within the Navier-Stokes equations.

There are various finite difference methods which are used to approximate time derivatives of ordinary and partial differential equations including, the Crank Nicolson, Adam-Moulton, Runge-Kutta and Adam-Bashforth methods. All methods vary in approaches and all differ in advantages and disadvantages to the problem. Crank-Nicolson, for example, adopts an implicit method, thus making it robust over a larger number of time steps, but a tri-diagonal matrix is required to solved at every time step, which incurring large computational costs. The method which is used to approximate the time derivatives concerning this work has employed the fully explicit Adam-Bashforth / backwards multi step method of second order;

$$\frac{1}{M}\sum_{j=0}^{k} a_j u^{n+1-j} = \sum_{j=0}^{k-1} b_j H(u^{n-j}) \tag{3.14}$$

The terms a_j and b_j can be determined by setting the first term in the truncation error to zero, calculated via a Taylor expansion around $(n+1)M$ and their values are for second order;

$$a_0 = \frac{2+r_n}{1+r_n}, \quad a_1 = -1 - \frac{1}{r_n}, \quad a_2 = \frac{1}{1+r_n}$$
$$b_0 = 1 + \frac{1}{r_n}, \quad b_1 = -\frac{1}{r_n}, \tag{3.15}$$

where $r_n = (t_n - t_{n-1})/M$. For a full derivation the author guides the reader to [106]. By implementing this particular numerical approach, it gives a good degree of the

approximations, as they are based on historical points within the domain, thus re-solving the derivatives as the time progresses.

3.4. Hunt's Flow Finite Difference Solver.

The Hunt's Flow DNS solver used within this work was developed by Dr Krasnov [107, 108]. A flow of a conducting fluid with the velocity $\boldsymbol{u} = (\boldsymbol{x}, t)$ passing through a fixed external magnetic field $\boldsymbol{B_0}$, induces the electromotive force (emf) $\boldsymbol{u} \times \boldsymbol{B_0}$ and drives drives the electrical current $\boldsymbol{J}$, which is governed by Ohm's law.

The interaction of the induced electrical current and the total magnetic field $\boldsymbol{B} = \boldsymbol{B}_0 + \boldsymbol{b}$, where $\boldsymbol{b}$ denotes the induced magnetic field, produces a Lorentz force affecting the fluid flow. The interaction between the fluid flow and the induced electromagnetic fields can be written in the form of a quasi-static approximation (2.47) – (2.49) The Lorentz force can then be represented as $\boldsymbol{j} \times \boldsymbol{B}$.

The DNS solver has been developed to numerically simulate MHD flows in a rectangular duct with ideally conducting Hartmann walls and ideally insulating side walls (see Fig 2). It is based on a FDM with a collocated grid arrangement, uniform at the core and non-uniform at the side walls. The boundary conditions are periodic in the stream-wise (x) direction and standard no-slip conditions are applied at the solid *y* & *z* boundaries (2.50).

At the walls MHD boundary layers develop, their structure being dependent upon the balance between viscous, inertial and the Lorentz forces as described in Chapter 2. In regimes where Ha is high, as is in the case of a nuclear fusion reactor, i.e. $Ha = 4000 - 8000$, very strong shearing and wall friction characterizes the instabilities found within these developed layers. In addition to the Hartmann layers, boundary layers parallel to the external magnetic field are observed; these are commonly referred to as Shercliff layers. The thickness of the Hartmann and Shercliff layers were described in section 2.5. An imposing challenge for the DNS of this particular flow regime was satisfactory resolution of these thin boundary layers via grid refinement at the walls. Mainly this is because insufficient numerical resolution leads to errors within the charge conservation and an inadequate balance of the kinetic energy. Nevertheless, tight clustering at the side walls was deemed to be an expense that was worth incorporating, as most if not all instabilities were found to reside there. The balance which

was optimized between the computational cost against the tight clustering is describe further on within this chapter.

The finite difference scheme used within this work was used to approximate equations (2.47) – (2.49). The DNS utilizes a time discretization method based on (3.16). The incompressibility condition is satisfied by applying the standard projection method [109], which requires that any vector field $\boldsymbol{u}$ can be decomposed onto two components, a divergence free solenoidal vector field $\boldsymbol{u}^*$ and the gradient of a scalar, which would be the pressure in the system. This decomposition method is both unique and orthogonal. As the solver advances from time step n to $n+1$ the following procedure is carried out:

Solve the electric potential equation $$\nabla^2\phi^n = \nabla\cdot(\boldsymbol{u}^n \times \boldsymbol{B}) \tag{3.16}$$

Compute electrical current $$\boldsymbol{J^n} = -\nabla\phi^n + (\boldsymbol{u}^n \times \boldsymbol{B}) \tag{3.17}$$

Compute $$\boldsymbol{F^n} = -(\boldsymbol{u}^n\cdot\nabla)\boldsymbol{u}^n + \frac{1}{Re}\nabla^2\boldsymbol{u}^n + N(\boldsymbol{j}^n \times \boldsymbol{B}) \tag{3.18}$$

Compute intermediate velocity field $$2\boldsymbol{F}^n - \boldsymbol{F}^{n-1} = \frac{3\boldsymbol{u}^* - 4\boldsymbol{u^n} + \boldsymbol{u^{n-1}}}{2M} \tag{3.19}$$

Solve pressure equation $$\nabla^2 p^{n+1} = \frac{3}{2M}\nabla\cdot\boldsymbol{u}^* \tag{3.20}$$

Add pressure correction $$\boldsymbol{u^{n+1}} = \boldsymbol{u}^* - \frac{2}{3}\mathrm{M}\nabla p^{n+1} \tag{3.21}$$

The boundary conditions for the pressure at the solid walls are gained via direct projection of (3.21) on the wall normal:

$$\frac{\partial p^{n+1}}{\partial n} = \frac{3}{2\mathrm{M}}\boldsymbol{u}_n^* \tag{3.22}$$

Moreover, the computational grid is orthogonal, uniform in the core and non-uniform at the boundary of the domain, thus allowing for clustering at the walls in the y & z directions. The clustering and non-uniformity is to aid in fully resolving the flow in the MHD boundary layers, especially at high Ha. The non-uniform grid is generated by applying a coordinate transformation, i.e. hyperbolic tangents or sine. There are currently two forms of grid stretching that can be applied in the code, either a hyperbolic tangent, or a modified Gauss-Lobatto distribution:

$$z = L\frac{\tanh(A\varphi)}{\tanh(A)} \quad or \quad z = L\left(Asin\left(\varphi\frac{\pi}{2}\right) + (1-A)\varphi\right), \tag{3.23}$$

In (3.23) L is the duct half-width, $-1 < \varphi < 1$ is the uniformly distributed co-ordinate and A is the parameter which accounts for the strength of clustering and z represents the wall normal coordinate. For the *y*-coordinate stretching is similar.

A highly conservative, second-order spatial discretization scheme for incompressible fluids in the low-R_m approximation [110, 111, 112] has been adopted. The discretization is performed directly on to a non-uniform grid with a partially collocated arrangement. The equations within this domain are approximated via the standard formula of derivatives, i.e. co-ordinate transform $z = z(\varphi)$ the partial derivatives $\frac{\partial^2 f}{\partial z^2}$ and $\frac{\partial f}{\partial z}$ are $\frac{\partial f}{\partial z} = \frac{1}{c_1}\frac{\partial f}{\partial \varphi}$ and $\frac{\partial^2 f}{\partial z^2} = \frac{1}{c_3} = \left(c_1\frac{\partial^2 f}{\partial \varphi^2} - c_2\frac{\partial f}{\partial \varphi}\right)$, where c_1 and c_2 are defined as $c_1 = \frac{\partial z}{\partial \varphi}$, $c_2 = \frac{\partial^2 z}{\partial \varphi^2}$. There are two methods which are used to solve (3.16) and (3.20) for both electric potential and pressure. One method can be applied if periodic boundary conditions are used in the stream-wise *(x)* direction. This method employs the Fast Fourier Transform (FFT) in the periodic co-ordinate. Additionally, the 2D Poisson equation is written as a general separable elliptic partial differential equation of second order in terms of the transformed co-ordinates, by central difference, part of the Fishpack library [113]. The second method is applicable in an arbitrary three dimensional domain with arbitrary boundary conditions, i.e. no periodic boundary conditions in the stream-wise direction It is again based on a central difference of second order which is applied to all three transformed co-ordinates as implemented in the Mudpack library [114 the non-linear term in the momentum equation is skewed, i.e. $\frac{1}{2}\frac{\partial(u_i u_j)}{\partial x_i} + \frac{1}{2}u_i\frac{\partial(u_j)}{\partial x_i}$. The first term

is discretized via a fourth order central difference scheme, i.e. $\left(\delta_{\varphi} f\right)_i = \frac{f_{i-2} - 8f_{i-1} + 8f_{i+1} - f_{i+2}}{12h}$ and by the third order upwind formula for the second term [114], where h is the grid step along φ.

Staying with the momentum equation, the Laplace operator within the viscous term is discretized by using central difference of fourth order and applied to $\nabla\phi^n$, ∇p^{n+1} in addition to the divergence operators within (3.17), (3.19), (3.21), (3.16) and (3.20) respectively. A central second-order scheme is applied to the Laplace operator in the right hand side of (3.14) (3.16) and (3.20).

The discretization of the non-linear term, divergence and gradient operators are modified at interior grid points close to the walls and as a four point central stencils are not available within this case, asymmetric solutions are required to give approximate solutions to the normal derivatives of the mean velocity at the wall; which are used to evaluate the mean wall shear stresses, thus determining the overhaul mean pressure gradient. Therefore to evaluate related derivatives, we employ a third-order finite difference scheme based on the boundary point and the three nearest internal points as suggested in [114].

$$\left(\delta_{\varphi} f\right)_0 = \frac{-11f_0 + 18f_1 - 9f_2 + 2f_3}{6M} \tag{3.24}$$

$$\left(\delta_{\varphi} f\right)_1 = \frac{-2f_0 - 3f_1 + 6f_2 - f_3}{6M}, \tag{3.25}$$

where φ and M are the uniform coordinate and step size respectively, the indices 0 represent the wall and 1 represents the first interior points. However there is a drawback to the discretization in the transformed coordinates as it limits the choice of grid clustering at the walls by omitting the singularity $c_1 = \frac{\partial z}{\partial \varphi} = 0$. However, this gives rise to an issue to the

solution for the pressure Poisson equation. In order to overcome this, the boundary condition (3.20) in the transformed coordinates is replaced by $\frac{\partial p}{\partial \varphi} = c_1 \frac{\partial p}{\partial z} = c_1 \frac{3}{2M} u_n^* = 0.$

The non-uniform grid is a highly conservative for incompressible fluid flows of low R_m MHD, directly discretized in the physical coordinates. The solution variables $\boldsymbol{u}, p, \boldsymbol{j}$ *and* ϕ are all stored at the same grid point, as well as (3.16) – (3.20). As the grid is collocated, half integer points located midway between the regular points are employed, in a staggered formation aiding in the computations of the spatial velocity and current fluxes. The half integer points give an approximation to the divergence operator located within (3.16) and (3.20) and discretize the non-linear term in the momentum equation.

The derivatives of the first order are approximated by the following discretization formulas

$$\left.\frac{\delta_2 f}{\delta_2 x}\right| x_i \equiv \frac{1}{2}\frac{f_i - f_{i-1}}{x_i - x_{i-1}} + \frac{1}{2}\frac{f_{i+1} - f_i}{x_{i+1} - x_i} \tag{3.26}$$

$$\left.\frac{\delta_1 f}{\delta_1 x}\right| x_i \equiv \frac{f_{i+1/2} - f_{i-1/2}}{x_{i+1/2} - x_{i-1/2}} \tag{3.27}$$

$$\left.\frac{\delta_1 f}{\delta_1 x}\right| x_{i+1/2} \equiv \frac{f_{i+1} - f_i}{x_{i+1} - x_i} \tag{3.28}$$

The above formulas (3.26) and (3.27) are based upon regular grid points, staggered grid points and (3.28) for staggered grid points. In addition to these formulas we also require linear interpolation between the regular and staggered grid points Fig 8;

$$f_{i+1/2} \approx \widetilde{f^x}|x_{i+1/2} \equiv \frac{f_i + f_{i+1}}{2} \tag{3.29}$$

$$f_i \approx \overline{f^x}|x_i \equiv f_{i+\frac{1}{2}} - \left(f_{i+\frac{1}{2}} - f_{i-\frac{1}{2}}\right)\frac{x_{i+\frac{1}{2}} - x_i}{x_{i+\frac{1}{2}} - x_{i-\frac{1}{2}}}, \tag{3.30}$$

where tilde represents interpolated values at the staggered grid points and the bar symbolises interpolated values at the regular grid points, while the upper index x denotes in which way the interpolation is performed. At the velocity correction sub-step (3.21) the velocity fluxes at the half integer points are calculated using;

$$F_i^{n+1} = u_\iota^{*x_\iota} - \frac{\widetilde{2M}}{3}\frac{\delta_\iota p^{n+1}}{\delta_1 x_\iota} \tag{3.31}$$

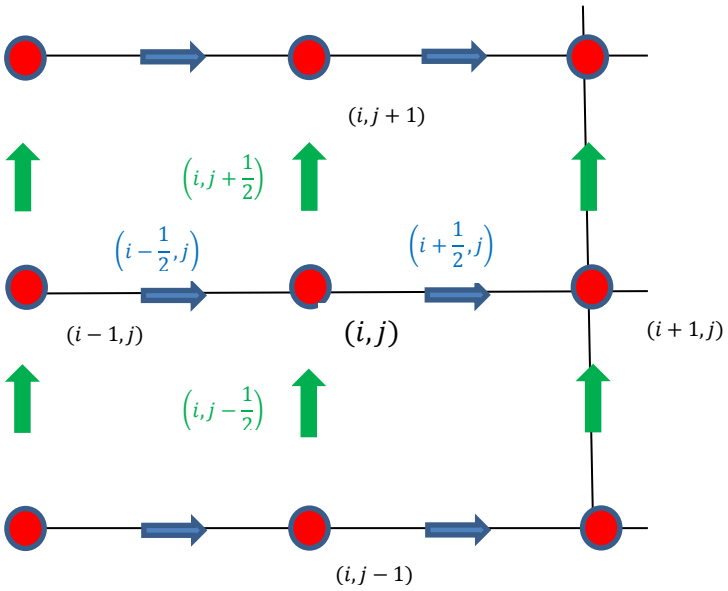

FIGURE 8. A collocated grid arrangement in 2-D. The red dots represent integer points where u, p, j and φ are approximated. Blue and green arrows denote the half integer points for the velocity and electrical current flux quantities in the x_i and x_j directions.

By substituting (3.31) into the incompressibility, which is enforced using the velocity fluxes, i.e. $\frac{\delta_1 F_i}{\delta_1 x_i} = 0$, we achieve the consistent form of (3.20):

$$\frac{\delta_1}{\delta_1 x_i}\left(\frac{\delta_1 P^{n-1}}{\delta_1 x_i}\right) = \frac{1}{M}\frac{\delta_1 u_i^{*x_i}}{\delta_1 x_i} \tag{3.32}$$

Within (3.32) the left hand side is the central difference discretization of the Laplace operator. The advantage of its now compact form ensures the absence of numerical pressure oscillations. By employing the discretized fluxes and velocity interpolations at the neighbouring half-integer points, the non-linear term can be rendered in divergent form. An example of this in the i-th momentum equation is

$$\frac{\delta_1(\widetilde{F_j u_\iota^{x_J}})}{\delta_1 x_j} \tag{3.33}$$

If the incompressibility condition is observed, then (3.33) is deemed to be conservative for the transport of kinetic energy. The viscous terms within the momentum equations are discretized using the central difference scheme of second order, based on the velocities integer grid points. The pressure gradient however, of the momentum equation which appears in (3.21) is approximated by using grid point values of pressure as;

$$\frac{\delta_2 p^{n+1}}{\delta_2 x_i} \tag{3.34}$$

But as is noticed, it is inconsistent with (3.30) in the kinetic energy equation and the use of (3.34) leads to errors of $\sim 0[M(\Delta x)^2]$ within the kinetic energy balance. However the error can be tolerated as it is of third order and dissipative, thus not affecting the stability

properties of the scheme. The method of discretization for the electromagnetic terms takes advantage of the electric current fluxes at the half integer points;

$$G_i^n = -\frac{\delta_1 \phi^n}{\delta_1 x_i} + (\boldsymbol{u^n} \times \boldsymbol{B})_i^{x_i}, \tag{3.35}$$

where the approximation of the divergence operator which expresses the current conservation is

$$\frac{\delta_1 G_i^n}{\delta_1 x_i} = 0. \tag{3.36}$$

The Poisson equation for the electric potential is obtained by the substitution of (3.35) into (3.36), resulting in;

$$\frac{\delta_1}{\delta_1 x_i}\left(\frac{\delta_1 \phi^n}{\delta_1 x_i}\right) = \frac{\delta_1}{\delta_1 x_i}\left[(\boldsymbol{u^n} \times \boldsymbol{B})_i^{x_i}\right] \tag{3.37}$$

By implementing (3.14) – (3.16) it includes the solution to (3.37), calculations to (3.35), the interpolation of current fluxes to integer grid points $j_i^n = \overline{G_i^{n_{x_i}}}$ and the calculations of the Loretz force $N(\boldsymbol{j^n} \times \boldsymbol{B})$.

There are other issues which need to be highlighted within this scheme, namely boundary conditions. As to not lose conservation properties, the collocated grid is extended across the boundaries by one step. By extending the boundaries in this manner, it allows the application of the central difference and central interpolation to the boundary points. The position therefore of the *ghost* points is defined as

$$z_{-1} = z_0 - (z_1 - z_0) \tag{3.38}$$

A third-order extrapolation based upon the cubic Lagrangian polynomial fit to four points of the non-uniform grid is used to calculate the solution variables at the ghost points. The third order extrapolation ensures the second order approximation of the viscous term at the walls. An additional issue that requires addressing is the solution to the Poisson equation for pressure and potential on a non-uniform grid and this additional issue is resolved with the help of high level libraries, provided by either [113] or [114] libraries, which solve a separable elliptic PDE. In a 2-D the equation therefore is

$$a_2(\gamma)\frac{\partial^2 f}{\partial \gamma^2} + a_1(\gamma)\frac{\partial f}{\partial \gamma} + a_0(\gamma)f + b_2(\varphi)\frac{\partial^2 f}{\partial \varphi^2} + b_1(\varphi)\frac{\partial f}{\partial \varphi} + b_0(\varphi)f = r(\gamma, \varphi) \tag{3.38}$$

The coefficients of (3.39) are determined by the coefficients of the coordinate transformation, i.e. c_1 and c_2 which were denoted in previous calculations. There are evidently some coordinate transformations within (3.39), i.e. grid stretching, and (3.26 leads to the Poisson problem in this form. The derivatives of the unknown function *f* within [113] and [114] are approximated on a uniform grid with second order central stencils;

$$(\partial_\varphi f)_i = \frac{f_{i+1} - f_{i+1}}{2h}, \qquad (\partial_{\varphi\varphi} f)_i = \frac{f_{i+1} - 2f_i + f_{i-1}}{h^2} \tag{3.40}$$

As we need to retain the conservation properties of the scheme, there has to be an equivalence between the approximation of the Laplace operator on the non-uniform grid and the discretization of the uniform grid of the transformed (3.39). Therefore at this point the methodologies used in resolving (3.16) and (3.20) will be described in more detail in order to show the scheme retains both conservation properties and periodic boundary conditions in at least one direction of the flow.

The derivative of a function f is derived via a coordinate transformation of the second derivative operator with second-order accuracy on a non-uniform z-grid as demonstrated below

$$(\delta_{zz}f)_i = \frac{(f_{i+1} - f_{i+1})(z_i - z_{i-1}) - (f_i - f_{i-1})(z_{i+1} - z_i)}{\left(\frac{1}{2}\right)(z_{i+1} - z_{i-1})(z_{i+1} - z_i)(z_i - z_{i-1})} \tag{3.41}$$

Here, in (3.41) the Poisson equations (3.16) and (3.20) are obtained as a direct result of subsequent applications of (3.27) and (3.28), applied to the gradient and divergence operators respectively. Therefore (3.41) is the only guaranteed assumed formula which results in *u* and *j* being divergence free and maintains the schemes conservation properties. The transform coefficients are written with three coefficients as a different approximation of $\partial z/\partial\varphi$ on a different stencil

$$\frac{\partial^2 f}{\partial z^2} = \frac{1}{c_3^3}\left(c_1\frac{\partial^2 f}{\partial \varphi^2} - c_2\frac{\partial f}{\partial \varphi}\right) \tag{3.42}$$

If we re group (3.41), we can substitute in (3.42) into its left hand side. The right hand side however we substitute (3.42) of the partial derivatives $\partial f/\partial\varphi$ and $\partial^2 f/\partial\varphi^2$ on a uniform grid. After some final regrouping and manipulation we finally arrive at;

$$(\delta_{zz}f)_i = \frac{f_{i+1}\left(c_1 h - \frac{c_2 h^2}{2}\right) - 2c_1 h f_i + f_{i-1}\left(c_1 h + \frac{c_2 h^2}{2}\right)}{c_3^3 h^3}, \tag{3.43}$$

where c_1, c_2 and c_3 are found as demonstrated in (3.40) the grid is always arranged so that $z_{i+1} \neq z_i \neq z_{i-1}$. Thus the coefficient c_3^3 will never be zero:

$$c_1 = \frac{z_{i+1} - z_{i-1}}{2h},\ \ c_2 = \frac{z_{i+1} - 2z_i + z_{i-1}}{h^2},\ \ c_3^3 = \frac{z_{i+1} - z_{i-1}}{2h}\frac{z_{i+1} - z_i}{h}\frac{z_i - z_{i-1}}{h}. \tag{3.44}$$

We now progress to the issue of the flow with periodic boundary conditions. The Fast Fourier Transform is applied to one direction and the 2D problem of the Fourier expansion is solved via the libraries described in [113] and [114]. The issue initially produces a problem for the correct evaluation of the wave number α, in the periodic *x*-direction. If the *x*-direction is periodic, the Poisson problem in the *k*th Fourier mode can be thus written as;

$$\left[\frac{\partial^2 \tilde{f}_k(y,z)}{\partial z^2} + \frac{\partial^2 \tilde{f}_k(y,z)}{\partial y^2} - \alpha_k^2 \tilde{f}_k(y,z)\right] = \tilde{r}_k(y,z) \tag{3.45}$$

The stream wise wave number is defined as $\alpha_k = k2\pi/L_x$ for $k = 0 \ldots, N_x/2 - 1$ and $\tilde{f}(y,z)$ and $\tilde{r}(y,z)$ are the Fourier coefficients for the unknown function. The Fourier Transform is applied in discrete forms of (3.32) and (3.37). As the derivative in Fourier space is not equivalent to the finite difference of the derivative used in (3.27) and (3.28), it therefore introduces an error into the divergence free constraint of the velocity and electrical current. So to ensure that the solenoidal character of the mentioned fields, α is replaced with α_{eff} in the following manner and provides an exact match between (3.45) and the 3-D finite difference discretization of the Poisson equation.

$$\alpha_{eff} = \frac{\sin\left(\alpha \frac{1}{2}\delta x\right)}{2\delta x} \tag{3.46}$$

3.5. Modifications.

Throughout the course of the extensive number of simulations performed, modifications have been implemented by the author of the code to optimize simulation run times. The first modification to the solver concerns the diffusive terms $\frac{1}{Re}\nabla^2 \boldsymbol{u}$**.** The main advantage to this initial modification was that the diffusive term could now be treated explicitly as in (3.18) or implicitly, via again through the Adams-Bashforth multistep method of second order, thus

involving a linear *L(u)* and non-linear part *N(u)*, which could be dealt with more efficiently at low Re & high Ha flow regimes. The truncation error of (3.47) is of order $O(M^k)$ [107].

$$\frac{1}{M}\sum_{j=0}^{k} a_j u^{n+1-j} = \sum_{j=0}^{k-1} b_j N\left(u^{n-j}\right) + L(u^{n+1}) \tag{3.47}$$

In both regimes, the viscous term proved to be the cause of numerical instability, mainly owing to strong clustering at the wall or low Re values where viscous term would dominate. Strong clustering at the walls posed severe limitations on the implemented values of M, as the three elliptic problems for all three components of velocity needed to be solved. A disadvantage to the implicit modification though, resulted in the simulations to be resolved on average two to three times slower than the explicit scheme alone. But for $Re < 2{,}000$ or $Ha > 200$ the M parameter could be up to 10^2 higher. This results in, for certain parameter combinations, associated with strong clustering at the walls, an increased computer efficiency up to a factor of 20.

In addition to the implicit modification, a second modification was included which consisted of imposing different types of boundary conditions for the solution of the Poisson problem for electric potential ϕ. For the case of ideally conducting walls, a Dirchlet boundary condition $\phi = 0$ was implemented, as the wall normal component $\boldsymbol{j_n}$ of the electric current is non-zero, thus currents flow into the walls. Finite wall conductivity is treated following the thin wall approximation [112] meaning that the MHD equations have to be solved only within the fluid domain. The current flow within the wall therefore is taken into account by employing a particular boundary condition for ϕ:

$$\frac{\partial \phi}{\partial n} = C_w \Delta_\tau \phi, \tag{3.48}$$

where n, τ and Δ_τ are the wall-normal, wall parallel directions and Laplacian in the plane of the wall respectively. Here C_w represents the ratio between the fluids conductivity and the thickness of the walls.

The elliptic solver, in part, from the Fishpack library [113] only has the ability to solve simple forms of boundary conditions, i.e. Dirichlet and Neumann non-homogeneous or a mixed conditions $\partial\emptyset/\partial n + \alpha\emptyset = r$, where α is a constant. Therefore to satisfy (3.48) additional iterations were required. Details are extensively provided in [106]. This resulted in the increased computational time for each M. In order to accommodate for this, the method employed in [114] was implemented, but here we solve the Poisson problem with the Neumann boundary conditions, opposite to the method adopted in [114]; by updating the normal derivative at every iteration. The advantage to this modification improves the iterations as they can now be part treated semi-implicitly, thus the wall normal derivative and the Laplacian operator in (3.48) can be jointly employed, resulting in a mixed boundary condition for the Fishpack solver. This greatly improves the convergence of the regime and after preliminary simulations convergence is achieved after only 5 -8 iterations.

3.6. Preliminary results of simulations.

Since the Hunt's flow is a new application for this solver, certain verifications were needed in order to be able to have full confidence in the results. . Therefore numerous test simulations we conducted on varying grid resolutions and grid clustering at the walls before engaging into full simulation runs. The laminar duct flow simulations, described in more details in Chapter 4, were fixed at values *Re* = 1000, *Ha* = 100. *Re* was fixed in this manner since laminar solutions do not depend upon *Re*. Grid resolution and grid clustering at the walls was varied including $64^3, 128^3, 256^3$ and 512^3 in the *x, y & z* directions. The parameters of grid clustering at the ducts walls ranged from $A_y = 1.5 - 3.0$ & $A_z = 1.5 - 3.0$. As can be seen from Fig. 9 the side wall jets become gradually thinner and the maximum velocity increases with *Ha*. Therefore with these apparent numerical difficulties, testing the simulations at varying grid resolutions and stretching coefficients becomes non-trivial. All simulations were conducted upon Coventry Universities in-house cluster computer.

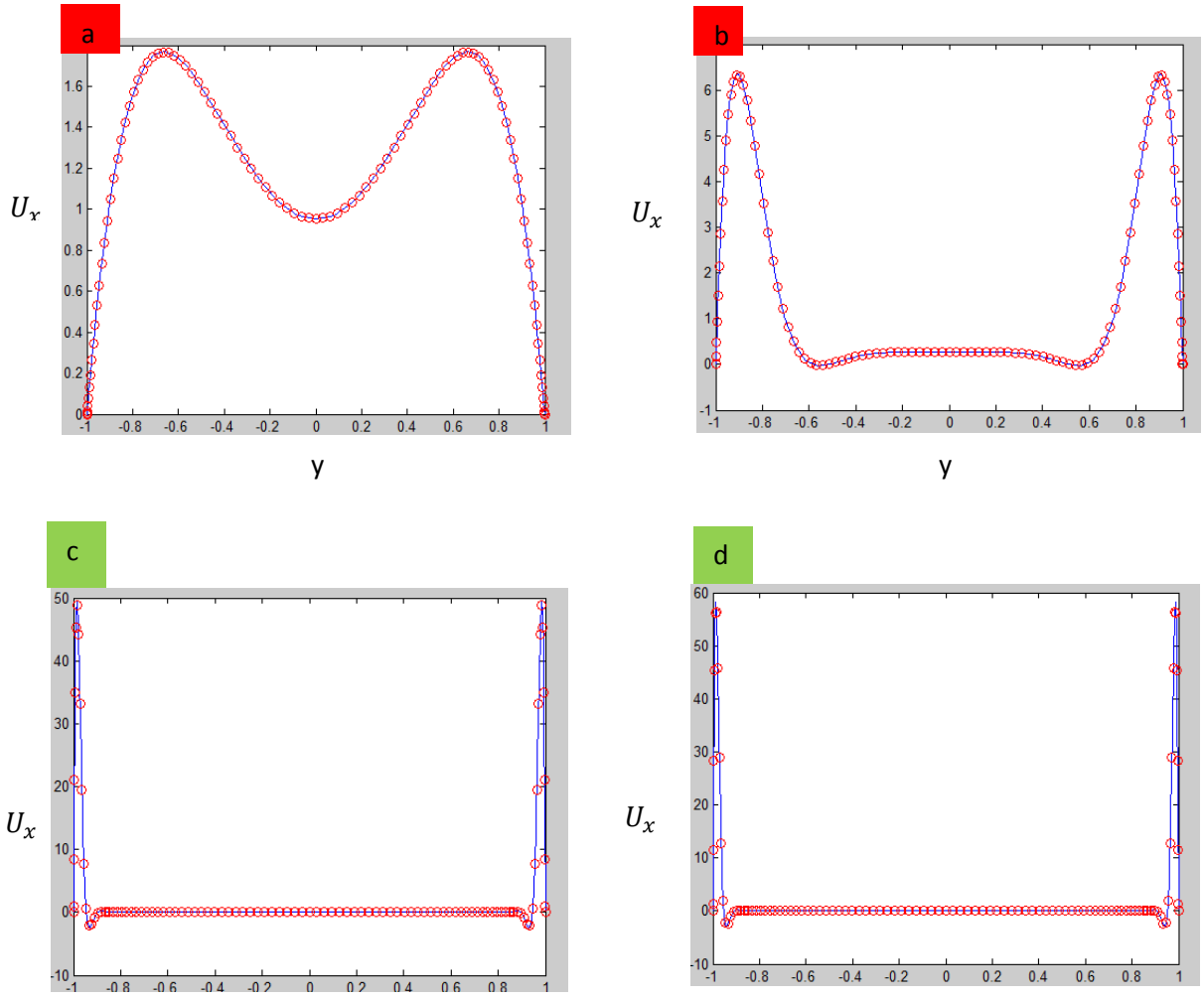

FIGURE 9. Comparative results of numerical (red circles) verses analyitical solutions blue line for laminar Hunt's flow. Grid resolution of 128×128 points in the $(x - y)$ – plane and grid clustering is set by the hyperbolic tangent with stretching coefficients $A_y = 2.5$ and $A_z = 3.0$ in the y and z directions correspondingly. (a) $Re = 500, Ha = 10\ (implicit)$, (b) $Re = 1{,}000,\ Ha = 100\ (implicit)$, (c) $Re = 4{,}000,\ Ha = 4{,}000\ (explicit)$. (d) $Re = 6{,}000,\ Ha = 5{,}500\ (explicit)$.

Fig 9 demonstrates a good agreement between analytical and numerical solutions, albeit at a fixed grid resolutions and stretching coefficient. Therefore to further determine whether the Hunt's flow code was as robust for varying grid resolutions and stretching coefficients, further laminar Hunt's flow tests were computed and comparisons made. Within this further test, we had fixed values of *Re* = 1000, *Ha* = 100. Grid resolutions were altered, between each separate simulation run at $64^3, 128^3, 256^3$ and 512^3, accompanied by varying stretching coefficients on each simulation between $1.5 \leq A_y \leq 3.0$ and $1.5 \leq A_z \leq 3.0$.

Contained within Fig. 10 we can conclusively provide substantial evidence that altering the grid resolution and stretching coefficients provided no noticeable alteration to the laminar base flow and in all accounts provides good agreements to the analytical solution.

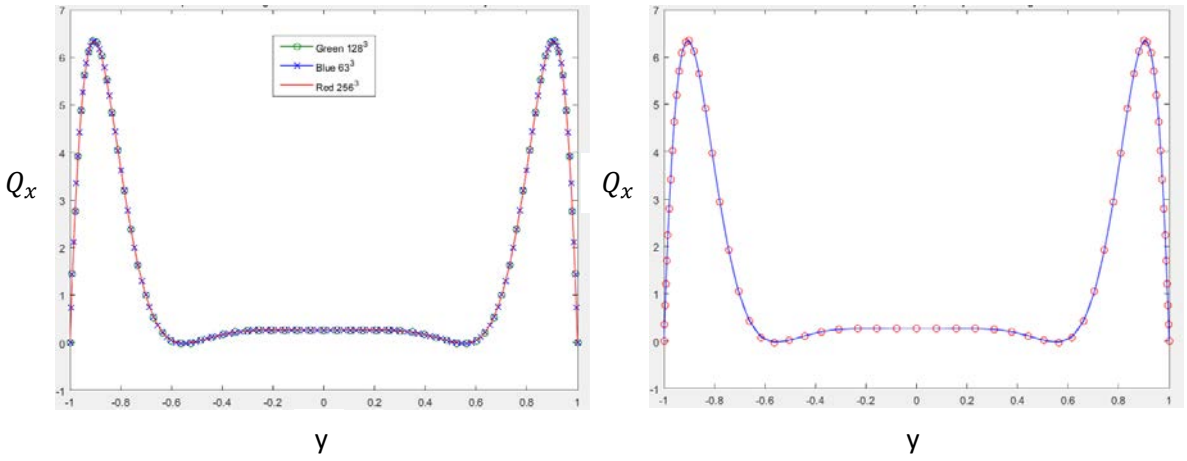

Figure 10: Example comparative results of varying grid resolutions and stretching coefficients. Both figures (a) and (b) demonstrate a fixed *Re* = 1000, *Ha* = 100. (a) demonstrates a comparative in grid resolution, including $64^3, 128^3$and 256^3 with stretching coefficient $A_y = 2.5, A_z = 2.5$. (b) displays a fixed *Re* = 1000, *Ha* = 100, grid resolution 128^3 with stretching coefficients $A_y = 1.5$ & 3.0, $A_z = 1.5$ & 3.0.

It is also worth noting that additional tests were also undertaken to benchmark versions of the code with explicit and implicit treatments of the viscous term $\frac{1}{Re}\nabla^2 v$. Preliminary runs were conducted on a lower grid resolution, 256×128^2 in the $x.y,z$ direction respectively, and the grid stretching coefficients were set by a hyperbolic tangent were fixed at $A_y = 3.5$ and $A_z = 4.0$. The base line simulations at *Ha* = 1000 For example demonstrated that the implicit treatment of the viscous term was beneficial for the overhaul performance of the code. Moreover, ΔM (integration time step), could be increased by a factor of 100 without the loss of numerical stability. But this situation changed as we increased further to *Ha* = 4,000. At this point the explicit treatment of the viscous term becomes computationally faster. The main reason for this development is that at high Ha, or more precisely, at large interaction parameter $N = Ha^2/Re$, the stability of the scheme and correspondingly ΔM, is governed by

the MHD term [115]. The MHD terms are fully explicit, thus making the specific treatment of the viscous term irrelevant at larger *N* values.

The implemented boundary conditions for the electric potential, corresponding to finite wall conductivity also required verification. This has been done by reproducing some test cases from previous work stated in [114], conducted on a grid of 96×96 in the *y* and *z* directions respectively, employing the implicit solver with a conductance ration of $C_w = 0.1$. The grid stretching, set by the hyperbolic tangent was $A_y = 3$ & $A_z = 3$. The comparative results of the finite and ideally conducting Hartmann walls are shown in Fig 11. The numerical results obtained through this investigation demonstrate maximum velocities and mid-cut distributions in perfect agreement to those results obtained through [114]. The solver has also been successfully applied and tested on MHD flows in ducts with insulating walls although results demonstrating this will not be provided in this work.

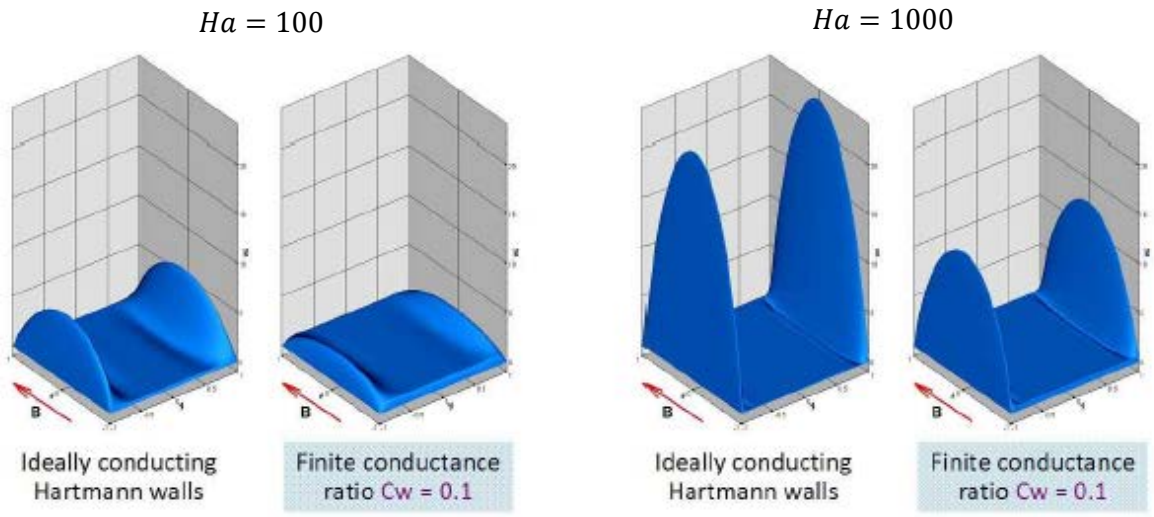

FIGURE 11: A comparative of laminar Hunt's flow through the use of DNS. *Ha* = 100 (left) and *Ha* = 1000 (right). Two cases are shown for each *Ha* number, these are ideally conducting Hartmann walls, in addition to the case of walls having finite conductivity. Wall conductance ratio is $C_w = 0.1$.

Once this in-depth study baseline laminar flow regime on the Hunt's flow code had concluded, it was found to be found robust over a wide range of grid resolutions and stretching coefficients. However a compromise had to be determined between grid resolution and computation time. As can be expected an increase in grid resolution greatly increased the computational time of each simulation. Therefore an average value was determined for both grid resolution and stretching coefficients, set by a hyperbolic tangent, in order to enable the most efficient way of completing future simulations in order to produce best results The values therefore to be determined on all subsequent simulation runs were 265^3 grid points in the *x, y, z* respectively and stretching coefficients A_y & $A_z = 2.5$. Fully accredited simulation runs could now commence, with each proceeding simulation running for approximately 200 CTU, i.e. $M = 2{,}000{,}000$ * $\Delta M = 0.0001$ to complete.

3.7.Time dependence of the fluid flow simulation.

Flow being subjected to an externally applied constant magnetic field, as in the present investigation, adequate numerical approximation of the viscous and non-linear term as well as of the Lorentz force in the non-dimensional Navier-Stokes equation becomes a pressing issue. An example of this would be a fully turbulent flow at high Re and low Ha. Such a regime would be dominated by the convective transport of momentum. The numerical instabilities of such a regime are thus produced by the non-linear term, which in turn has a significant influence on the admissible time steps ΔM. In contrast, at low *Re,* or laminar flow, the cause for numerical instability would be the domination of the viscous term, again if treated fully explicit, thus ΔM must be kept as small as possible. Flows of high Ha & Re, are likely to approach the limit of instability produced by the Lorentz force. Therefore to detect these major causes of numerical instabilities early on in the flow regime, the value of *M* was kept low. If there were instabilities in the flow regime, only a small amount of real time was indulged to reach a diverged regime. The governing parameters could then be altered and a new flow regime initiated with a reduced ΔM to compensate for the sensitivity of the regime.

As the flow is periodic in the stream-wise (x) direction, continual simulations at a low value of M were undertaken for each targeted Ha & Re parameter set. Once each low M value simulation had completed, an analysis was taken via the use of the total full scale kinetic

energy variable, i.e. $Q_{tot} = q_x^2 + q_y^2 + q_z^2$. If the targeted simulation had been deemed to converge, M could then be increased, i.e. $100000 \leq M \leq 200000$ for each subsequent simulation. This process was repeated until a steady state had been reached. The next stage to verify the simulations steady state could then be undertook and determined through the implementation of the Simpsons Rule

$$\int_a^b f(x)dx \approx \frac{\Delta x}{3}(y_0 + 4y_1 + 2y_2 + \cdots + 4y_{n-1} + y_n), \text{ where } \quad \Delta x = \frac{b-a}{n} \tag{3.49}$$

n is always even.

Once the peaks and troughs of the q_x^2 component of Q_{tot} had seemed to have abated, two Simpsons rule comparisons tests were taken. If the result of the comparatives were equal, the simulation was deemed to have reached its steady state and a full investigation could then be undertaken. The process of the Simpson rule comparative is demonstrated in Fig 12. The domain dimensions of early simulations were $4\pi \times 2 \times 2$, but this was later altered to $8\pi \times 2 \times 2$, the reasons for which will be explained in more detail further on in this study. As a *rule of thumb*, assuming 100% parallel implementation efficiency for each arbitrary $M = 20000$, it took on average 40 hrs to complete, employing 4 nodes, equating to 32 CPU's. To calculate the real time taken for one value of M requires the following procedure: 40hrs / 200000 = 0.0002 hours or 0.72 seconds of real time per *M*. As these calculations are based on 32 CPU's, for 1 CPU it would of course be 32 times longer. Therefore, 0.0002 * 32 = 0.0064 hrs or 23.04 seconds per *M*, thus giving, on average the required CPU-hours per value of M. We can correspond this information to virtual flow time. Therefore, if we choose ΔM = 0.0006, we multiply by M, giving 120 Convective Time Units (CTU), .i.e. 0.0006 * 200000. This means that we spend 40 hrs on 32 CPU's, i.e. 40*32 = 1280 CPU hrs to calculate 120 CTU. To calculate each CTU required, we need to divide the CPU hrs by 120 CTU, i.e. 1280/120 = 10.6 CPU hrs for each CTU, on average. Therefore in real, actual time at $M = 200000,\ \Delta M = 0.0006$ we need 120*10.6 = 1272 CPU hrs and 1272/32 = 39.75hrs or 1.65 days. So, for a simulation to reach a steady state where an analysis could be done, it takes on average 2 million time steps which equates to 16.5 days to complete. Some simulations took longer, i.e. 5 million time steps. It must be re-iterated that the above

calculations are only a guide and differing times of completion were obviously heavily dependent on $Ha,\ Re, \Delta M$ and M.

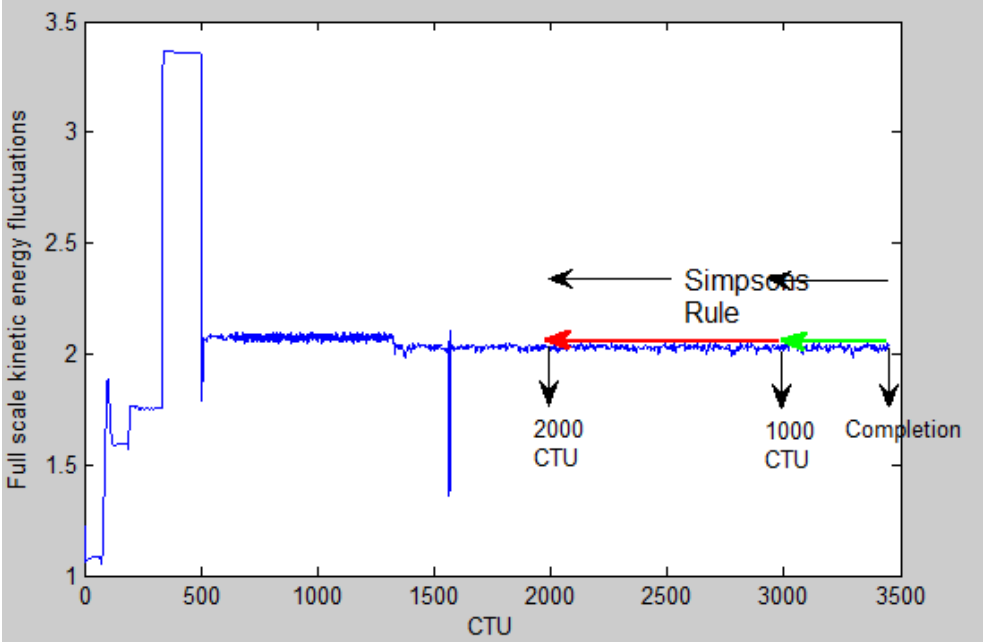

FIGURE 12. The Implementation of Simpson's rule to the q_x^2 component of the full scale kinetic energy graph, i.e. $Q_{tot} = q_x^2 + q_y^2 + q_z^2$, here we demonstrate *Ha* = 100, *Re* = 5000. If the integration results from the green line and the red line matched, the simulation was deemed to have reached converged statistics.

4. Variation of the Reynolds number.

Within this chapter we initially, as a benchmark investigation, describe laminar duct flow and then progressively continue the study further into time dependent turbulent flow. Additionally, one also demonstrates the effects of the Lorentz force (2.16), and its influence on a conducting fluid flow, altering the velocity profile in such a way not inherent with hydrodynamic flow Fig 13.

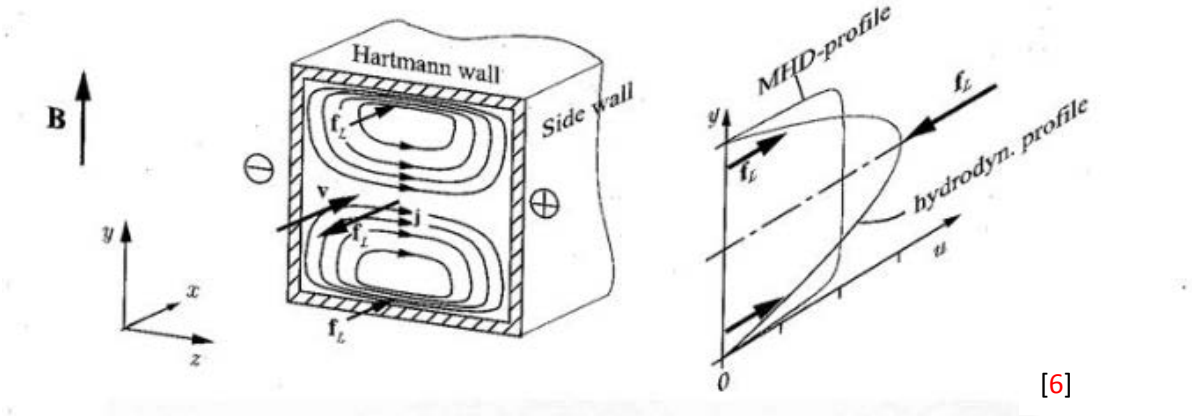

[6]

FIGURE 13. Cartoon of the effects of MHD duct flow (left). The effects the Lorentz force has on the viscous velocity profile within the duct in comparison to a hydrodynamic flow regime (right).

Muller and Buhler reviewed various aspects of MHD flow in channels of varying shapes [125]. Within the context of this investigation, we only consider ducts of rectangular cross section. By considering a steady, laminar flow within a duct of cross section $2\delta \times 2\delta$, we drive an electrically conducting fluid through a duct with constant pressure gradient. The fluid flow is un-directional, $\boldsymbol{u} = (x_1, 0,0)$. The applied external magnetic field $\boldsymbol{B} = (0,0,\boldsymbol{B})$ is perpendicular to the flow in the z-direction. Walls perpendicular to the magnetic field are referred to as Hartmann Walls ($\sigma_{HW} y = \pm\delta$) and the walls parallel to the magnetic field are known as the side walls ($\sigma_{SW} z = \pm\delta$). In the centre of the duct, commonly referred to as the core region, the magnetic field interacts with the conducting fluid, through the fluids motion, thus inducing an electrical field $\boldsymbol{u} \times \boldsymbol{B}$, with electrical current $\boldsymbol{J}$. As a *priory* to the interaction, a voltage is produced between the walls parallel to the magnetic field. The

induced currents depend on the conductivity of the duct walls. Figure 14, for example, where all duct walls are perfectly insulating $\sigma_w \to 0$, no electrical currents may leave the domain of the fluid [113] and must close their path within the fluid. Alternatively, if all duct walls are electrically conducting $\sigma_w \to \infty$, the currents close through the duct walls and the boundary side layers which reside there. The current experiences no resistance in a fully conducting duct and consequently the pressure drop in the core is much greater than in an insulating duct. Finally, assuming that the side walls are perfectly insulating and the walls perpendicular to the magnetic field are perfectly conducting $\sigma_{HW} = \sigma_{SW} = \infty$, the electrical currents are thus compelled to turn almost parallel at the side walls, closing their path within the Hartmann layer. We will be studying this latter duct electrical composition in greater depth as it is the only focus in the context of this study.

[7]

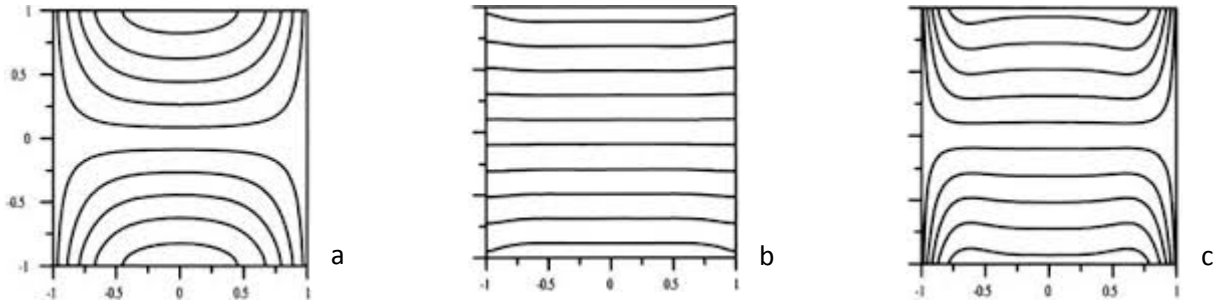

FIGURE 14. Electrical current paths in a duct of rectangular cross section with walls of various electrical conductivities: (a) all walls electrically insulating, (b) all walls electrically conducting and (c) Hartmann Walls (top and bottom) electrically conducting, side walls electrically insulating.

In all MHD flows, the fluid within the core of the duct experiences a force which opposes the flow and is referred to as the Lorentz force. This force homogenizes the fluid flow profile and determines the momentum balance within the core. Consequently, the force has a tendency to damp instabilities and supress turbulence, and as such, it is a major contributor to the pressure drop within a MHD system. In environments where magnetic fields are strong, the electromagnetic contribution brought by the Lorentz force dominates over the viscous contribution. To this end, it can therefore be suggested that the greater the external magnetic field, the greater the Lorentz force, which in turn increases the pressure drop within the duct.

4.1. Instabilities in MHD duct flow and a word on the transition to turbulence.

Included in this section we will be investigating the development of instabilities within Hunt's flow, particularly those close to and within the jet region of the flow. It is important to focus on the origins and development of the side wall jet instabilities as their inherent structures have been regarded as the first stage in the transition to turbulence in a time dependent flow not only in MHD fluid flow, but also in purely hydrodynamic environments [85, 117]. Turbulence alters the properties of a flow regime and understanding, or more importantly, the predictions of such flows are crucial in the realization of proposed cooling systems for thermo-nuclear fusion reactors. It is important to state that turbulence within such a specific concept as liquid metal blankets design is not a phenomena which should be avoided. Turbulence enhances in the mixing process of the fluid, thus improving heat and mass transfer. This helps to keep the blanket modules first wall, operating within acceptable temperature limits and promotes optimum heat extraction.

by the Kolmogorov theory [93]. According to this theory, the fluctuating part can be viewed as a broad random collection of different size vortices with the energy passing down from larger to smaller vortices in a cascade like manner. The larger vortices, decompose under inertia and evolve into. The transition to turbulence has been very briefly introduced in Section 1.6, but the importance of this phenomenon is in many different applications, not just liquid metal blankets. Laminar fluid flow is, in principle, is a solution to Eq. (2.30). But in order for the laminar flow to be physical, it must be stable, meaning that perturbations in the flow should vanish over time, reverting the flow back to its laminar state. Generally speaking, there is usually a critical *Re* parameter, i.e. Re_{cr}, where a laminar fluid state can no longer exist. Turbulence however, develops when inertia forces are predominant over viscous forces, or when *Re* is sufficiently large. The nature of turbulence makes predicting the flow very difficult, if not impossible. This is a consequence of the governing Navier-Stokes equations, which result in a small change to initial conditions, producing large changes to the motion of the fluid. As problematic as this maybe, statistical quantities within the flow such as mean velocity can be determined. This suggests that it is possible to separate a velocity field into a mean part and a fluctuating part.

A deeper understanding of turbulence is provided smaller vortices, so passing energy down to ever smaller vortices and thus giving rise to a cascade of kinetic energy. However, towards the latter part of the energy cascade, as the smallest vortices approach a *Re* value of unity, the effects of viscous dissipation becomes important. Kolmogorov theory assumes that turbulence is isotropic, which may not always be the case especially at the larger scales, velocity jets and boundary layers, *etc.*

MHD turbulence is different to hydrodynamic turbulence, as Ohmic losses, which are a result of the circulation of electric currents through the flow, lead to additional dissipation of kinetic energy. A laminar flow is basically a solution to the Navier-Stokes equations, irrelevant of the value of *Re*, but to determine that this solution is physical, it must be checked that it is in fact stable with respects to either imposed, or inherent perturbations. If this is not the case, a more complex laminar or turbulent flow sets in. Critical value of *Re* or *Ha* can be found by studying the condition under which linearized equations result in perturbations with a positive growth rate: a method more commonly referred to as a linear stability analysis.

Sterl [116] found that for an inviscid flow the inflexion point in the velocity profile was a condition for instability. The transition to turbulence according to this approach occurs as the linearly unstable mode grows until a point where the non-linear effects produce a secondary instability, and so on until the flow becomes completely turbulent. In the case of a circular pipe, linear stability predicts the flow remains stable even as $Re \to \infty$. But contradictory experiments demonstrate turbulence at a *Re* value of $Re \approx 3000$. Large perturbations could find their origins as a combination of two decaying linear modes and cases are available where the combination of these modes result in large amplitude, transient growth before decaying at $t \to \infty$. If for example these amplitudes become large enough, a non-linear transition occurs, thus generating turbulence [119]. This goes some way as to explaining why in the scenario of a Hartmann flow, the critical values are much lower than linear stability predicts, a phenomenon known as a subcritical bifurcation.

Furthermore, Joule dissipation has a tendency to damp out turbulence and an applied magnetic field, as in the case of this investigation, has the ability to alter the fluids velocity profile: resulting in the development of steep gradients, sheer, obstacles, inflexion points and most importantly, jets. Therefore the magnetic field can itself become a large source of instability to a flow which would otherwise be classed as stable; this was first demonstrated by Lenhert [120, 121] and later by Buhler. Due to the M-shaped velocity profile caused by

the magnetic field, Hunt [42] anticipated that the instabilities within the flow regime would be at large *Re* values, at several inflexion points, which lead to non-decaying, inviscid instability modes. Note that the M-shaped velocity profile is not limited to the square duct. The same type of profile is also observed at the inlet and outlet regions of the magnetic field and also in bends of ducts [72, 83, 84].

The evidence of jet instabilities in MHD duct flow have been experimentally reported in numerous studies [68, 69, 82, 99]. Reed and Picologlou [82] used probes to measure the velocity fluctuations in a square duct and found strong periodic fluctuations in the vicinity of the side walls. Determining that the onset of instabilities were explicitly dependent on the value of *Re*, with a critical *Re* in the range of $1300 < Re_{cr} < 2500$ at $Ha = 5 \times 10^3$. Subsequently, Ting *et al.* [85] employed asymptotic side layer solutions developed by Walker [123] as a base flow. They concluded that the transition to turbulence is expected at $Re_{cr} \approx 313$, which is an order of magnitude smaller than what was previously observed.

Buhler however stated that on the basis of this experiments, the transition to turbulence in the region of the velocity jet occurred via two successive bifurcations [99]. The first of which is that at low *Re,* where the flow is laminar and when *Re* is increased beyond this first Re_{cr}, small perturbations are observed. Pushing *Re* further, he also saw that beyond a second Re_{cr} an additional transition occurs which is characterized by perturbations of a much lower amplitude. Throughout the experimental results so far [82, 99, 122] a direct comparison between them is a touch ambiguous, as wall conductivities and aspect ratios differed. But nevertheless, all experiments predicted a stable Hartmann layer as the criterion of instability was $Re/Ha \approx 350$ [124, 101]. Recently, Priede *et al.* [103] studied a linear stability of Hunts flow, resulting in a myriad of velocity patterns as *Ha* was increased from zero. Curiously their results demonstrated that for low values of *Ha*, flow instabilities occur in the form of streaks across the entire duct cross section. At $Ha > 46$ they observed the same type of unstable modes as Ting *et al.* [85].

Throughout MHD flows, the applied magnetic field has the ability to damp turbulence within a conducting fluid. Also the interaction of the magnetic field with the electrical currents alters the velocity profile, producing a relatively flat, essentially laminar core flow; being more pronounced in duct regimes where we see fully conducting and semi-conducting (Hunt's flow) duct wall environments. Viscous effects in MHD flows are confined at the walls, which is a consequence of the electromagnetic interaction. This in turn produces strong

shearing effects at the walls as the fluid adheres to them. The electromagnetic interaction leads to the formation of boundary layers parallel to the magnetic field, the thickness of which has scales as $\delta_{sh} \sim Ha^{-\frac{1}{2}}\delta$. The side layers have received little attention over the years, with only one other investigation being conducted into their relative thickness [82]. However, in section 4.8 we take a closer look into previous results and demonstrate that in turbulent Hunts flow regime, the thickness of the side layers may differ from that determined in [82] Furthermore to the walls parallel to the magnetic field, walls which are perpendicular to the magnetic field also produce boundary layers, which were first predicted by Hartmann [37, 38]. Hartmann established that the thickness of these boundary layers is inversely proportional to the magnetic field, or to be more specific (2.54), $\delta_H = \sqrt{\rho\nu/\sigma B^2} = Ha^{-1}\delta$. The effect that the Hartmann layers has on the development of turbulence was studied much later in 1982 [98] and it was observed that the circulating electrical currents within the Hartmann layers closed their paths in the core of flow, which in turn lead to the damping of turbulence within this region of the flow.

In many studies into the transition to turbulence the most common approach is to perturb an initial laminar flow either by random noise or a combination of specially constructed modes [118]. In either case, the transient evolution and inherent thresholds are governed by perturbation amplitude and shape. This study computes unsteady solutions for chosen $Ha \,\&\, Re$ parameters starting from a zero-velocity initial state which is then allowed to naturally evolve and result in a plethora of new flow regimes. The subsequent analysis is based on the fluctuating KE of the transverse velocity components described in section 3.7. The flow regimes have been simulated for many CTU as described in Chapter 3 and the extended period of time in all simulation cases involved in this investigation has been a necessary requirement in order for the flow regime to reach converged statistics.

All simulations in this study have been conducted on a domain of $8\pi \times 2 \times 2$ to aid in fully resolving the instabilities which develop within the flow. Early simulations, were conducted on a domain of $4\pi \times 2 \times 2$, but as can be seen from Figure 15, this preliminary domain length shows only one detachment from the side wall, thus not giving a full representation of the flow regime. By increasing the domain length to 8π in the x – stream wise direction also confirmed that the periodicity of the side wall instabilities remained intact as Figure 15 demonstrates.

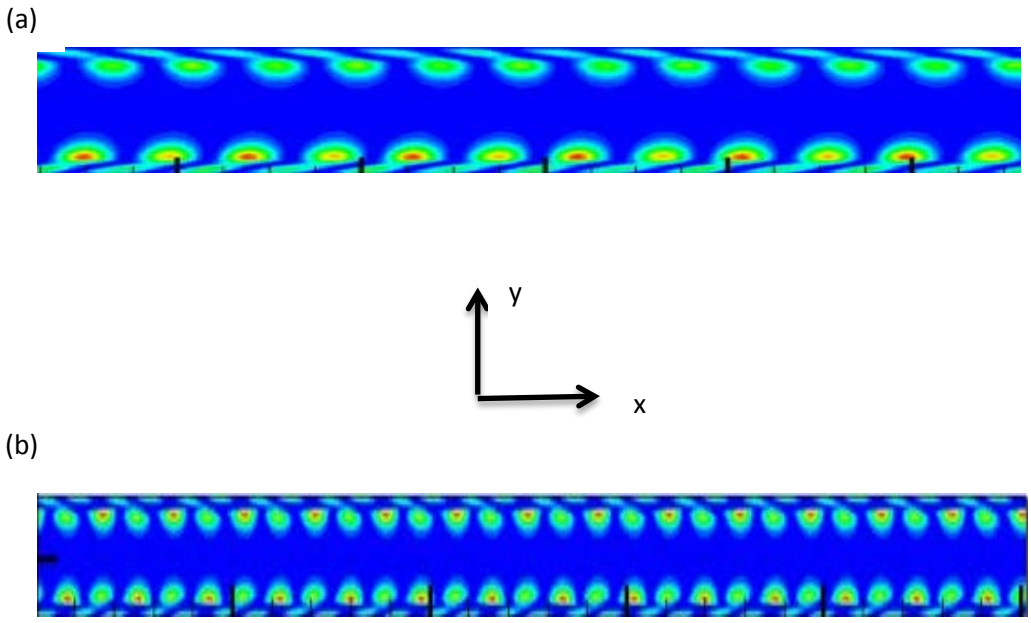

Figure 15. The side-wall instabilities for *Re* = 1000, *Ha* = 100 obtained with (a) 128^3 and (b) 256^3 resolutions, in addition to stretching coefficients $A_y = 2.5$ and $A_z = 2.5$

The smaller domain resulted in a premature appearance of jet detachment from the side walls. This is typical for certain combinations of flow and geometry parameters. For example, short domain essentially cuts *off large* wave length perturbations, which is clearly demonstrated in Fig. 16. As a result, the KE of perturbation will be different for long or short domains, as the longer domains can accommodate longer-wave perturbations. Additionally, the KE within the longer domain may stagnate for longer periods of time before it begins to propagate down the scale and populate smaller eddies.

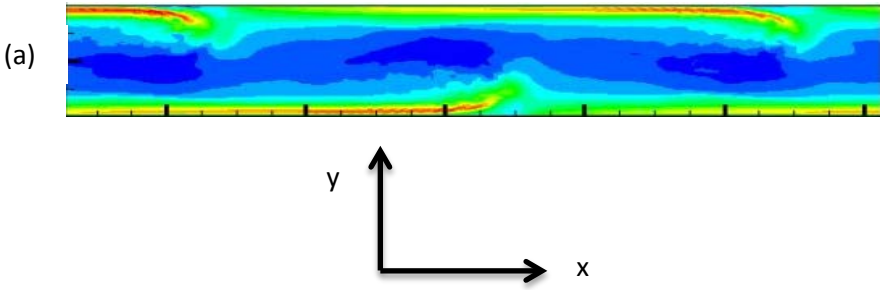

(b) 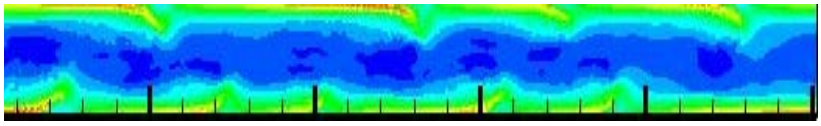

FIGURE 16. The full stream-wise velocity u_x in the (x, y)-mid-plane at z = 0 with the jet detachments at *Re* = 1700 and *Ha* = 100 for computational domains of length $L_x = 4\pi$ (a) and $L_x = 8\pi$ (b). Magnetic field is perpendicular to the (x, y) plane and the flow direction is from left to right.

4.2. Variation of Re at $Ha = 100$.

With each moderate Ha value, i.e. $Ha = 100, 200, 300$ the target value for each *Re* value was pre-determined as a single shot regime, as explained in section 4.1. By adopting this approach, initial parameters were immediately determined and the flow regime developed with the magnetic field applied from the outset. To determine at what point flow had reached a steady state, the procedure set out in chapter 3 was applied. Over time, the results of each KE investigation, described in section 3.7 and Fig 12 deemed the simulation to have reached a steady state. Table 1 demonstrates a small sample of CTU and real time values for converged statistics to be attained in *Ha* = 100 and varying *Re* simulations.

Table 1

Hartmann No	Reynolds No	M	CTU	CPU Hours	Days
100	500	5 Mil	8,960	85,106	57
	1000	4.7 Mil	8,521	82,843	52
	1500	4.1 Mil	3,482	31,126	27
	2000	4.4 Mil	3764	34,128	29
	3000	6.7 Mil	5,361	51,120	44
	4000	7.1 Mil	5,696	31,520	41
	5000	5.6 Mil	4,520	38,976	42
	10000	5.3 Mil	3,216	16,368	28

TABLE 1. The time taken for each individual simulation, as well as time steps, CPU hours and the real time taken for the flow regimes to reach a steady state at $Ha = 100$.

The flow regimes which will now be discussed further until section 4.8 is reached, will demonstrate new forms of instabilities located near the side walls parallel to the external magnetic field. The initial parameters for each separate simulation were set with a fixed *Ha* and *Re* value from the outset. As in other MHD studies, the presence of any time dependant fluctuation can be confirmed by measuring the KE of all three components of velocity. In Fig 17 the first increase or transitional phase in all three components of KE is associated with the first linearly unstable modes which were predicted by Ting *et al.* [85]. The second, more distinctive transitional phase can be further associated with the instability, involving partial jet detachment from the side wall. The pronounced spikes in all three components suggest the transition from one regime to the next, albeit the greatest transition can be undoubtedly seen in the q_x^2 component at t = 500 and 4500.

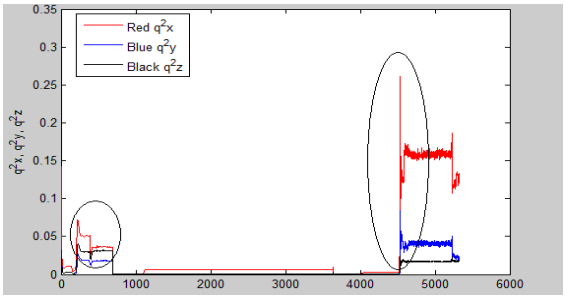

FIGURE 17. The temporal evolution of all three transverse velocity components, q_x^2, q_y^2 and q_z^2, for *Ha* = 100, *Re* = 3000. Transitional phases from initial unstable modes through to multiple side wall jet detachment are clearly highlighted with corresponding ellipsis.

The small scale instabilities near the side walls at the first transitional phase, which were predicted by Ting *et al* [85] and are viewed to exhibit anisotropy in the vertical *z* – direction, especially pronounced near the Hartmann walls. This can be viewed by the region negative λ_2, the second largest eigenvalue of the symmetric tensor $C_{i,j} = S_{i,j}^2 + \Omega_{i,j}^2$. Where $S_{i,j}$ and $\Omega_{i,j}$ are the symmetric and anti-symmetric parts of the velocity gradient tensor $\partial_j u_i$ [119]. The geometry of the developed anisotropic instabilities resembles a columnar structure, arranged in an almost parallel, periodic formation, comprising of clockwise (CW) and counter clockwise (CCW) rotating vortices travelling downstream in the *x* - direction. The CCW vortices can be observed slightly closer to the core of the flow, while the CW vortices tend to say closer to the side walls. These structures are now commonly referred to as Ting and Walker vortices (TW) [85]. An example of these side wall instabilities can be seen in Figure 18 for a low *Re* value, i.e. $Re = 500$.

FIGURE 18. Appearance of Ting-Walker vortices in the MHD side wall jet region for Hunts flow using DNS for *Ha* = 100, *Re* = 500. Streamlines are shown in the (*x*, *y*) mid-plane on the left and the iso-surfaces of the second eigenvalue of tensor λ_2 $C_{i,j} = S_{i,j}^2 + \Omega_{i,j}^2$ on the right

Since their discovery, these small columnar structures have been consistently observed at low-*Re* regimes and are viewed as the first stage of an unstable MHD flow. Even though TW vortices are present within a MHD flow, their inherent KE is so low, i.e. KE ~ 0.033% in comparison to the total KE within the entire flow regime, that they do not have any significant impact on integral flow patterns, i.e. walls stresses τ_w and total friction coefficient C_f. In the context of this investigation, TW vortices have been present in all differing *Ha* and *Re* flow regimes, i.e. $Ha = 100, 200, 300, 800 \,\&\, 2{,}000,\ 500 \leq Re \leq 20{,}000$, thus we can

conclusively state that TW vortices are a common feature within a Hunt's flows study at these parameters. A particularly new feature should be noted at this present time in that as Ha is increased, the appearance and structure of the TW vortices alters. The structures appear to become elongated in the x – stream-wise direction, close to the side walls of the duct. This can clearly be seen within Fig 19 and this phenomenon will be re-visited in Chapter 5.

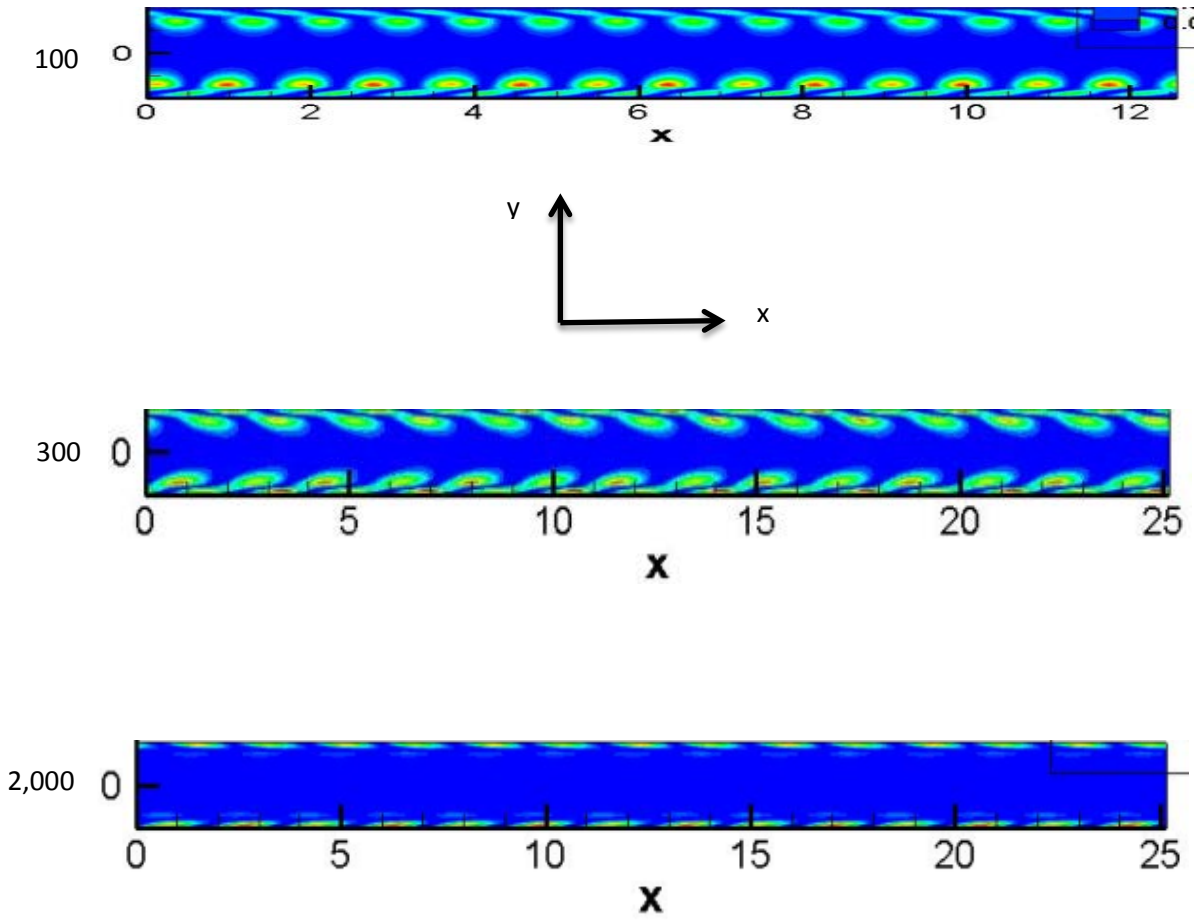

FIGURE 19. Instantaneous snap shots of Ting Walker vortices at different *Ha* values, i.e. *Ha* = 100, 300 and 2000 in the (*x*- *y*) mid-plane *z* = 0, flow from left to right. The same iso-surfaces are displayed here as in Fig 18 although here we shown them in 2-D . The *Re* value is fixed at *Re* = 2,000. Flow is from left to right.

The presence of TW vortices for a range of different Ha & Re parameters at the beginning of each simulation further confirmed the results from previous studies. Although in prior investigations, the stretching of the TW vortices in the U_x direction had not been noticed.

Before progressing, it has to be noted that the TW vortices were only observed at the beginning of each simulation. Now, re-visiting $Ha = 100$, we increase velocity from $Re = 500$ to $Re = 1000$. In doing so, an interesting and rather unusual flow regime is produced. We observe the initial TW vortices beginning to dissipate and eventually disappear completely after only 100 CTU, exhibiting a relatively un-perturbed laminar flow regime. This can be seen in Figure. 20 as a sharp drop in all three components of KE.

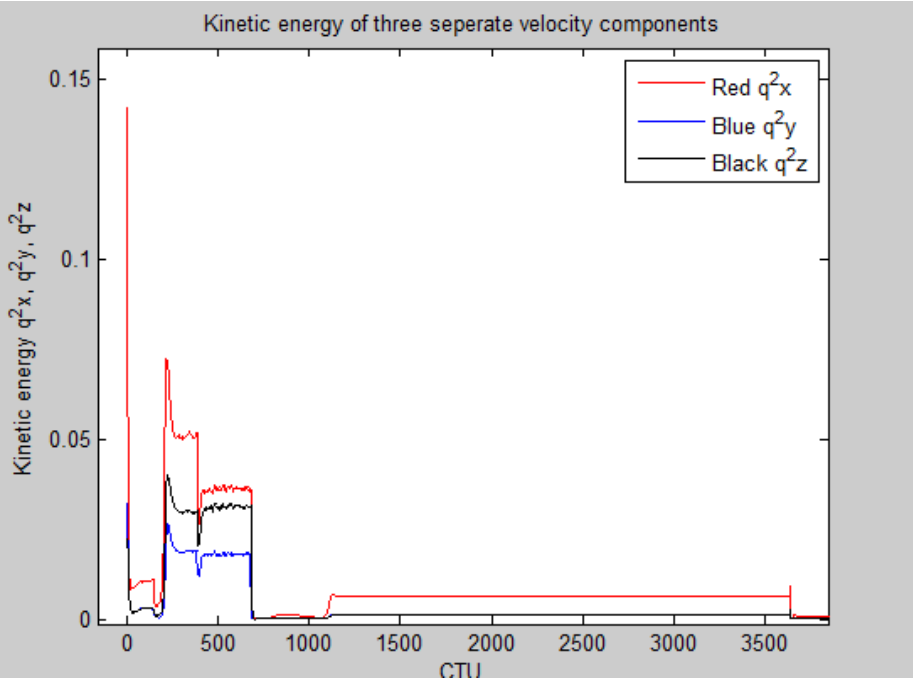

Figure 20. Time evolution of three components of the full scale kinetic energy, $Q_{tot} = q_x^2 + q_y^2 + q_z^2$. *Re* = 1300, *Ha* =100.

However, this situation alters through additional temporal development and new instabilities develop at the side walls, replacing the earlier TW vortices. The new instabilities are initially very similar in structure to TW vortices, but as they develop, they become much larger, both in size and KE. In fact, concerning inherent KE, the new structures contribute approximately 0.1% of the total KE within the flow, which in direct comparison to the KE exhibited by the

TW is almost three times as large and associated with the stream-wise velocity component, u_x. The newly developed structures are elongated in the stream-wise direction and once fully developed occupy 60 – 80% of the total flow domain (see Fig. 21). They are seen to follow the same pattern for increasing values of Ha, although as Ha is increased to greater levels, the new structures develop at a much faster rate. Evidence of the appearance of these larger structures have also been observed in purely hydrodynamic flows [118, 126]. Once these larger structures have developed, they remain for the full duration of the simulation.

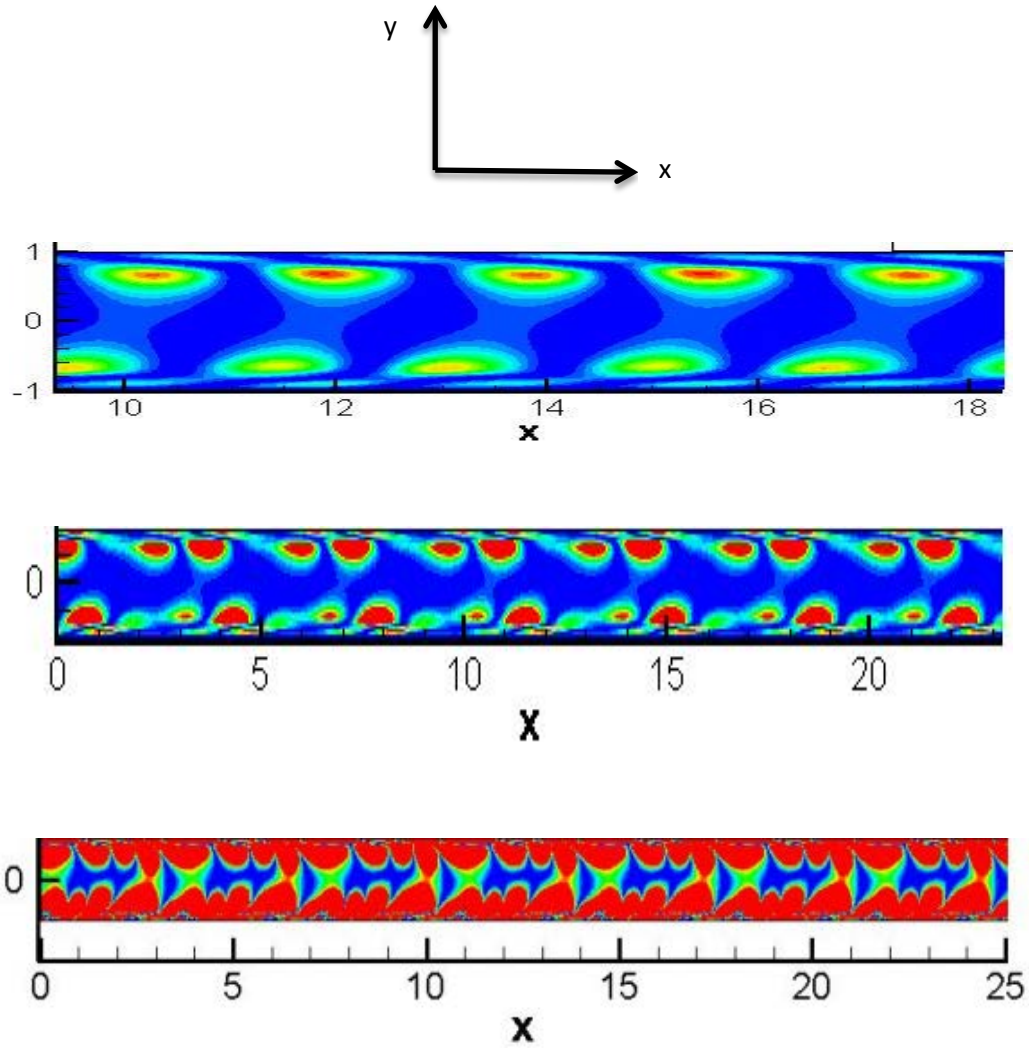

FIGURE 21. Temporal distribution of the full scale KE, $Q_{tot} = q_x^2 + q_y^2 + q_z^2$. Here we see the development of new instabilities located near the side walls in the (*x*, *y*) mid-plane *z* = 0 for *Ha* = 100, *Re* = 1,300.

4.3. Pike Teeth.

Progressing through to *Re* = 1400, there is again a further unusual development near the side walls. Additional new structures develop in the form of small-scale CW & CCW rotating vortices, located within the new larger vortices found at $1000 \leq Re \leq 1{,}300$. Upon initial inspection of the new smaller structures, there are a few remarkable insights. As can be seen in Figure. 22, they are very small structures, elongated in the vertical direction, travelling along the *x* - stream-wise direction, Their structure closely resembles that of "*pike teeth*", staggered in a periodic arrangement along each side wall in respect to the mid-plane symmetry *z* = 0. In order to verify that the *pike teeth* are not numerical artefacts, an additional investigation was undertaken at a greater grid resolution of 2048×384^2. Even at this resolution, the *pike teeth* structures remained.

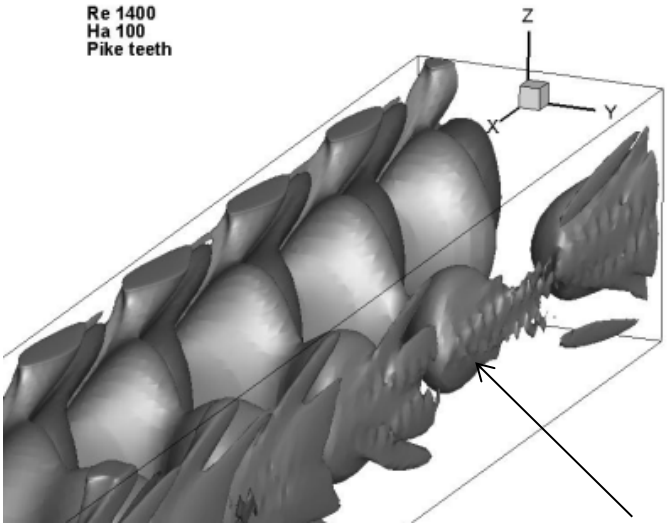

FIGURE 22. 3-Dimensional representation of iso-surfaces of the second eigenvalue λ_2 at *Ha* = 100, *Re* = 1,300. The new larger instabilities demonstrate a CCW (dark grey) & CW (light grey) formation close to the side walls. "*pike teeth*", elongated in the *z*-direction can be seen housed within the new unstable structures.

Since these in bedded small structures arose when the simulation was initiated from a turbulent flow state, they are not numerical artefacts. Therefore upon analysing the structures on a more deeper level, it was uncovered that the KE contained within them is approximately two times smaller than that found in the new temporally evolved larger instabilities observed

at $Re \leq 1300$, contributing 0.05% of the total KE within the flow, slightly greater than the contribution given by TW vortices as demonstrated in Table 2. However, the specific distribution of KE over the velocity component changes. The stream-wise u_x component is still dominating, but the energy associated with the vertical u_z component increases by a factor of two, producing strong anisotropy in the vertical direction, demonstrated via the transvers velocity component of KE $q_t = q_{z/q_y}$, again in Table 2.

Table 2

Re	q/Q_{tot}	q_t/Q_{tot}	q_y/q	q_z/q	q/Q_{tot}	q_t/Q_{tot}	q_y/q	q_z/q
	Incremental Simulations				**Decremental Simulations**			
300	Laminar				2.8%	0.45%	13.7%	2.4%
500	0.033%	0.0081%	11.0%	13.5%	6.3%	1.2%	16.1%	2.9%
1000	0.10%	0.0125%	4.0%	18.0%	9.5%	2.1%	18.0%	4.0%
1400	0.05%	0.0110%	4.0%	18.0%	Not Performed			
2000	10.0%	2.7%	19.0%	8.0%	Same as Incremental Run			
5000	3.5%	1.5%	17.0%	26.0%	Same as Incremental Run			

Table 2. TKE of velocity perturbations relative to the total kinetic energy of the flow Q_{tot} for different velocity components. Listed are the TKE $q = \langle u_x^2 + u_y^2 + u_z^2 \rangle$ and transverse part $q_t = q_y + q_z$, where $q_y = \langle u_y^2 \rangle$ and $q_z = \langle u_z^2 \rangle$ which taken from the hysteresis results. The brackets $\langle\rangle$ represent volume averaging and u_x is without mean flow.

In other words, the "*pike teeth*" can be viewed as being quiet strong in amplitude, but short in physical size in the *z* - direction. The first appearance of the "*pike teeth*", is seen at *Ha* = 100, *Re* = 1400 and CTU~240. Once the *pike teeth* set into the flow regime, they persist until the simulation has completed (see Figure 23). At $Re = 1{,}500$, the "*pike teeth*" do not disappear, but develop at an accelerated rate, stretching even further in the *z*-direction, demonstrating the same alternating behaviour as described at *Re* = 1,400. At $Re \geq 1{,}550$ there is no data to support the observation of "*pike teeth*" further, therefore concluding that they only appearing in a finite *Re* range, i.e. $1400 \leq Re \leq 1550$. Beyond *Re* = 1550 a different type of instability is observed. It can be viewed then that given their appearance, within such a small *Re* range, in addition to their gradual increase in their KE, that "*pike teeth*" maybe viewed as a catalyst

or nuclei for a new subsequent flow regime, namely partial jet detachment from the side walls.

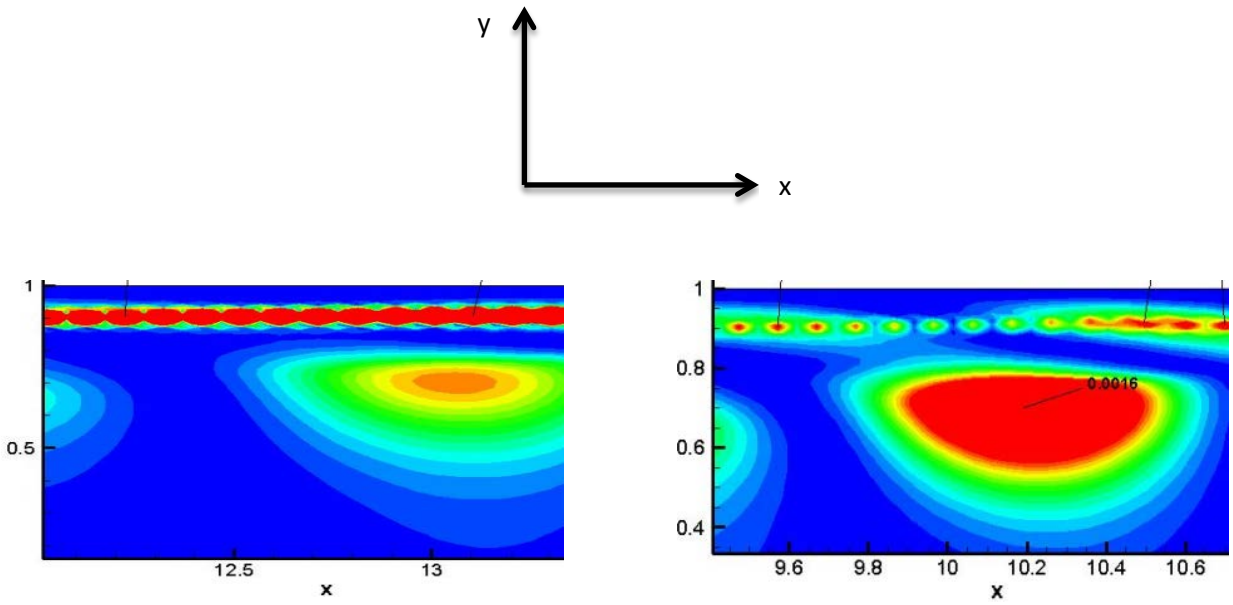

FIGURE 23. A close instantaneous 2-D snap shot of $Q_{tot} = q_y + q_z$ only, demonstrating "*pike teeth*" at the outer region of the domain (small red circles) moving in the *x*-direction at $Ha = 100, Re = 1{,}540$ in the (*x*, *y*) mid plane at $z = 0$ plane. Flow is from left to right.

Summary

An MHD transition to turbulence study was undertaken for, $500 \leq Re \leq 1000$ at $Ha = 100, 200, 300, 400, 800, 2000$ & 4000. The results have confirmed that TW vortices are present at the beginning of all flow regimes in this parameter range. Secondly, at $Ha = 100$, three separate flow regimes with $Re = 500, 1000$ & 1300 were studied. It was observed that between $1{,}000 \leq Re \leq 1{,}300$, TW vortices were replaced by larger time dependent flow structures near the side walls. These new structures occupying between 60 – 80% of the entire fluid domain once fully developed are much larger in both amplitude and physical appearance than the TW vortices. Again, for $Ha = 100$, Re was further increased in an additional five separate simulations, i.e. $1{,}300 \leq Re \leq 1{,}550$. In doing so, yet another new type of flow structures developed at $Re = 1430$, housed within the proceeding new structures found at $1{,}000 \leq Re \leq 1{,}300$. These new structures were found to be small in

size but not in amplitude. The structure of these in bedded vortices closely resemble *"pike teeth"* contributing 0.055% of the total KE within the entire targeted system, demonstrating increased anisotropy in the vertical z - direction. For $Re \geq 1{,}550$ there was no further evidence of "*pike teeth"* persisting within the flow.

4.4. Partial Jet Detachment.

Next, we shall try to establish if the existing and new instabilities described in section 4.2 & 4.3 have any significant effect on the flow regime, and if so, at what *Re* value it occurs. With this new focus, single investigations were carried out at fixed $Ha = 100$ and varying *Re* values, as in previous simulations. As there was no visual evidence of a further development occurring prior to $Re = 1{,}550$, the study was continued from this point. Four separate simulations were simultaneously initiated at $Re = 1600, 1700, 1800$ & 1900, each allowed to develop for a total of $M = 50^5$ time steps. In the previous work [122], it has been discovered that a new forms of instabilities occurred within a fully conducting duct MHD flow at $Re > 3500$, namely jet detachment from the side walls. The conductivity of duct walls in this present study was different but, nevertheless, jet detachment was expected at approximately around the same *Re*. Moreover, as we were attempting to attain at which point, if any, jet detachment could occur from the side walls, the range of Re stated above where initial detachment could possibly occur was reduced considerably, along with computational costs.

After initial results it was determined that at *Re* = 1700, 1800 and 1900, there was a second sharp increase in KE within all three velocity components, especially q_x^2, which was not observed at *Re* = 1600, as Figure 24 demonstrates. Upon visually studying the flow, it was concluded that jet detachment had indeed occurred at $Re = 1{,}700$, 1,800 & 1,900, but not at $Re = 1{,}600$. Based on this result, ten subsequent simulations were carried out focusing on $1{,}600 \leq Re \leq 1{,}700$ in incremental steps of $Re = 10$. In these additional simulations jet detachment was observed in Hunt's flow for the first time at $Re \approx 1{,}630$ (see Figure. 24.)

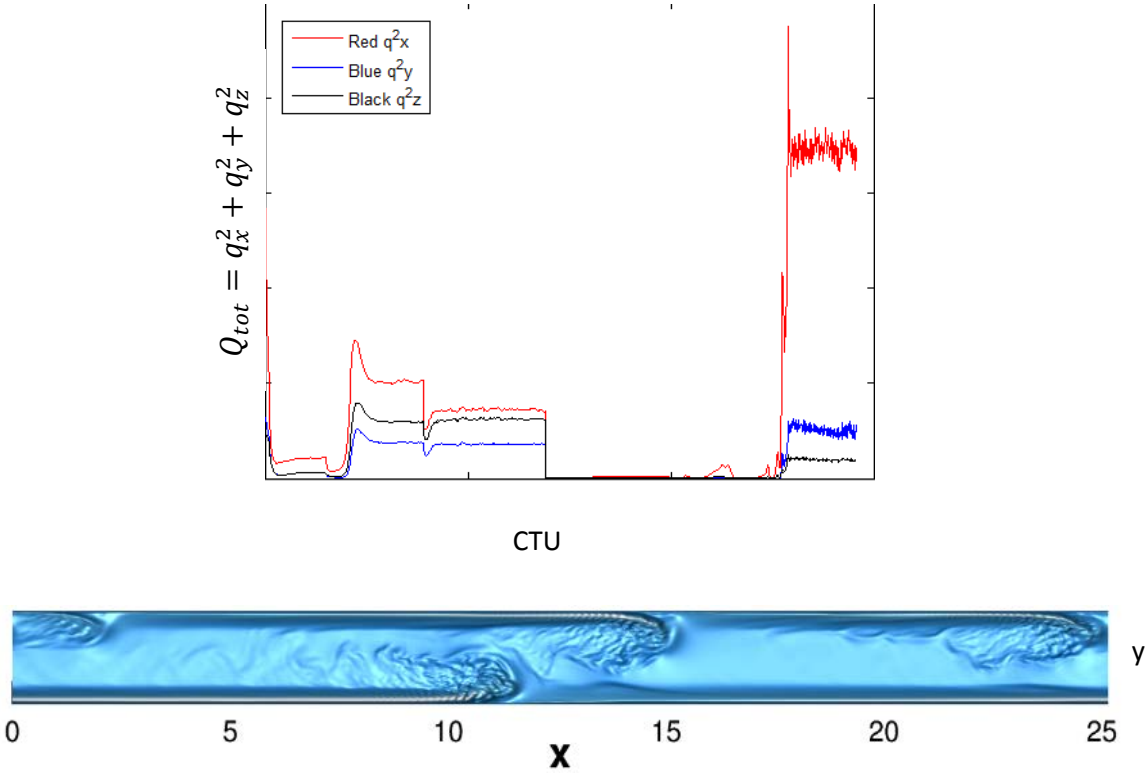

FIGURE 24. Distribution of $q_x^2 + q_y^2 and\ q_z^2$ along the flow with spikes coinciding with partial je detachment (top). Full stream-wise velocity u_x in domain $L_x = 8\pi$ of the first appearance of jet detachment in the (*x*, *y*)-mid-plane at *z* = 0 for *Ha* =100, *Re* = 1630. Flow is from left to right and the magnetic field is perpendicular to the (*x*, *y*) plane

As can be clearly seen in Fig. 24, the almost periodic jet detachment itself is dominated by a centre turbulent CCW rotation located behind the detachment, towards the core. Subsequently, the CCW rotations behind the detachments will prove to be non-trivial. However, having now determined the *Re* value at which jet detachment appears for the first time, the next step is to investigate why jet detachment occurs at these *Ha* and *Re* parameters. As mentioned previously, prior studies have observed jet detachment both within an MHD environment and a purely hydrodynamic environment [102, 117] but these investigations have been unable to produce a definitive description as to why this phenomenon occurs. Therefore the investigation into the cause of such a phenomenon is imperative for the following reason. The duct flow studied in this work is related to a blanket design in a proposed cooling system within a nuclear fusion reactor. An important aim of the blanket is to promote fluid mixing thus increasing heat and mass transfer by the flow.

As the time dependent flows for every simulation in this section are allowed to develop at a targeted Ha = 100 value, residing within the inner region of both velocity jets are small, periodic CCW vortices, producing small, time dependent instabilities. The first time that these small CCW vortices were observed within the context of this study is at $Re = 500$, Figure 25, below this *Re* value, no CCW we seen. The velocity of the fluid in the outer region of the jet, near the side walls, has accelerated to a much greater degree compared to the mean velocity of the core, thus producing strong shearing effects within these regions.

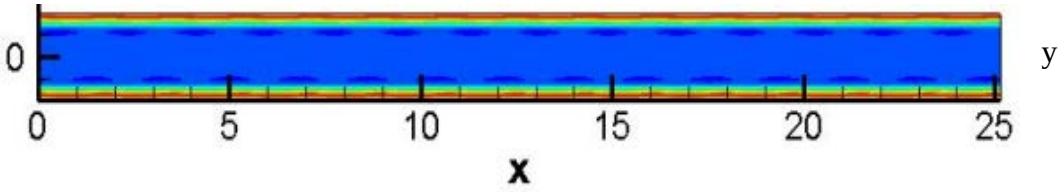

FIGURE 25. Full stream-wise velocity u_x is demonstrated in the (*x*, *y*)-mid-plane at $z = 0$. Demonstrating small periodic temporal instabilities of CCW vortices (dark blue) at the inner region of the velocity jet at $Ha = 100, Re = 500$. Flow from left to right and magnetic vector field is perpendicular to the (*x*, *y*) plane.

Combining the accelerated fluid within the velocity jet with the slower moving fluid in the core initiates a CCW vortex or reverse motion of the fluid in the outer region of the jet. As time develops, the now inherent CCW vortices begin to have a retarding and destabilizing effect on the side wall velocity jet. By increasing Re further, we observe that the small CCW vortices develop in both size and amplitude and begin to have a more dramatic effect on the fluid within the jet in its entirety.

We now use the fixed values of *Ha* = 100, *Re* = 1700 to demonstrate why jet detachment occurs as this give a good representation as to the phenomena. However, the influence, structure and behaviour of the CCW vortices in the lee of the detachment changes its influence as *Re* is increased in value. This change in appearance and influence will be addressed further on in the study. This is an important stage in development, as not only does the CCW vortices effect one side of the fluid domain, but they determine the flow pattern of both sides of the duct, as well as the core as *Re* increases. This detachment process will now be demonstrated in six phases, Figure 26. Close to the outer region of the jet, the now more localized CCW vortices begin to elongate in the x-stream wise direction, influencing larger

areas of the fluid along the jet than were initially detected at $Re = 500$, Figure 26 (a). As the flow evolves, the CCW vortices lose their periodic nature, becoming increasingly more localized and isolated. The structures increase in amplitude, fluctuating the fluid in the jet in both y & z-directons, Figure 26 (b). The CCW vortices now begin to develop more intensely, exhibiting stronger areas of localized reversed fluid, dramatically altering the relatively smooth appearance of the jet. This action results in sporadic areas of fluctuating fluid velocities Figure 26(c). We now observe their develop into much large structures and in doing so, effect a larger proportion of the surface area of the outer fluid within the jet, reducing its velocity over a greater area Figure 26 (d). The effects of this time dependent development begin to break up the continual high velocity fluid within the jet, lifting the jet away from the side wall. This finally results in total separation in the jet fluid, thus giving the immature development of partial jet detachment Figure 26 (e).

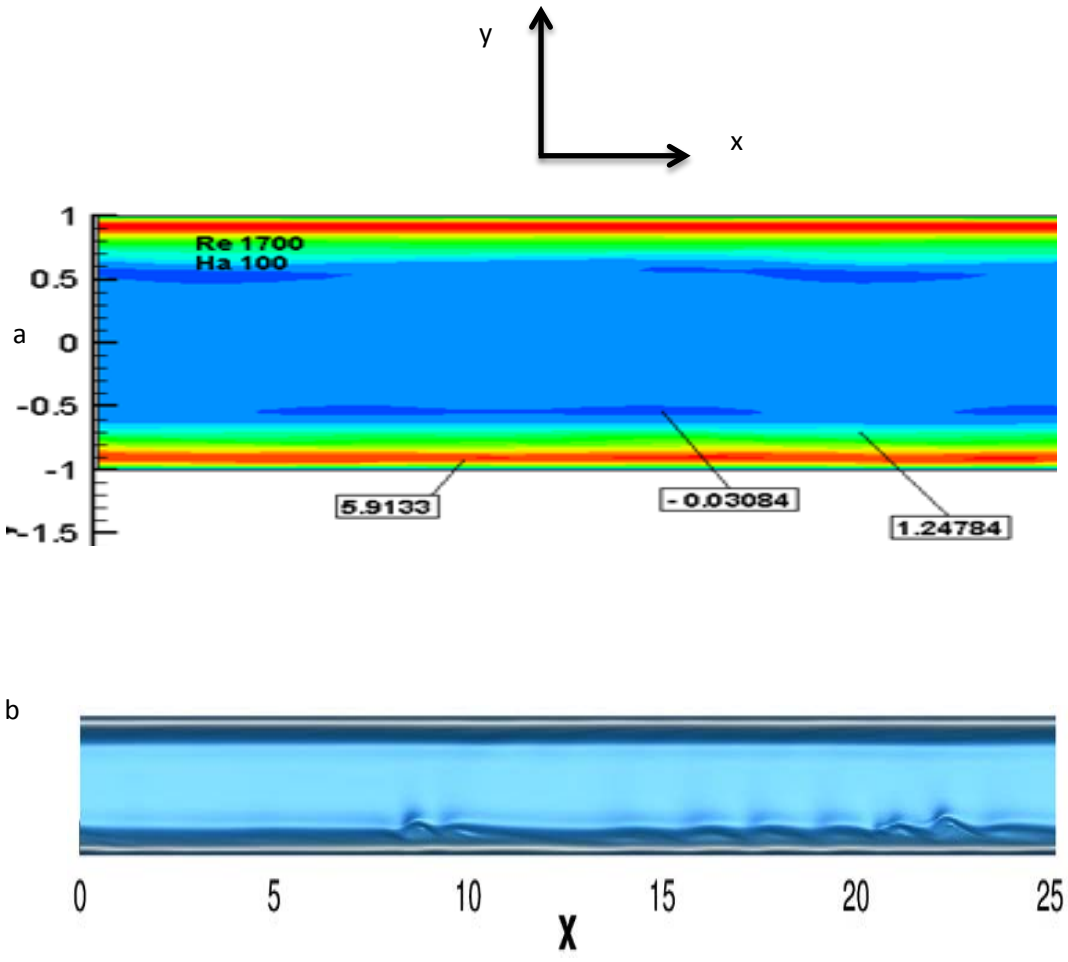

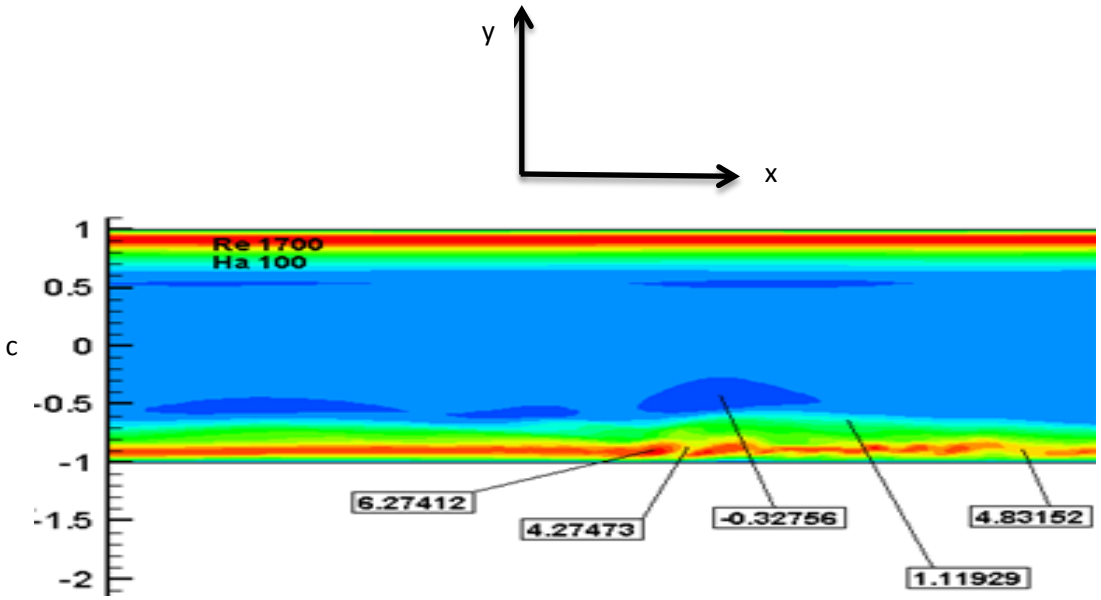
y
x
c
Re 1700
Ha 100
1
0.5
0
-0.5
-1
-1.5
-2
6.27412
4.27473
-0.32756
4.83152
1.11929

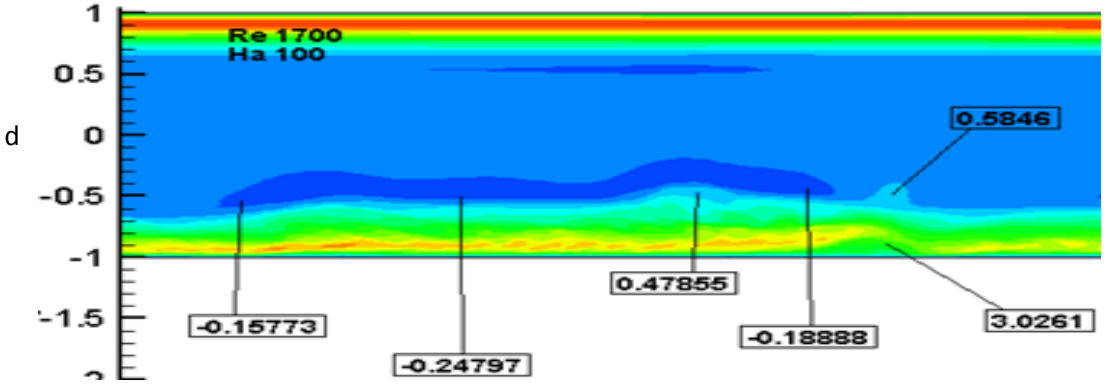
d
Re 1700
Ha 100
1
0.5
0
-0.5
-1
-1.5
0.5846
0.47855
-0.15773
-0.24797
-0.18888
3.0261


e

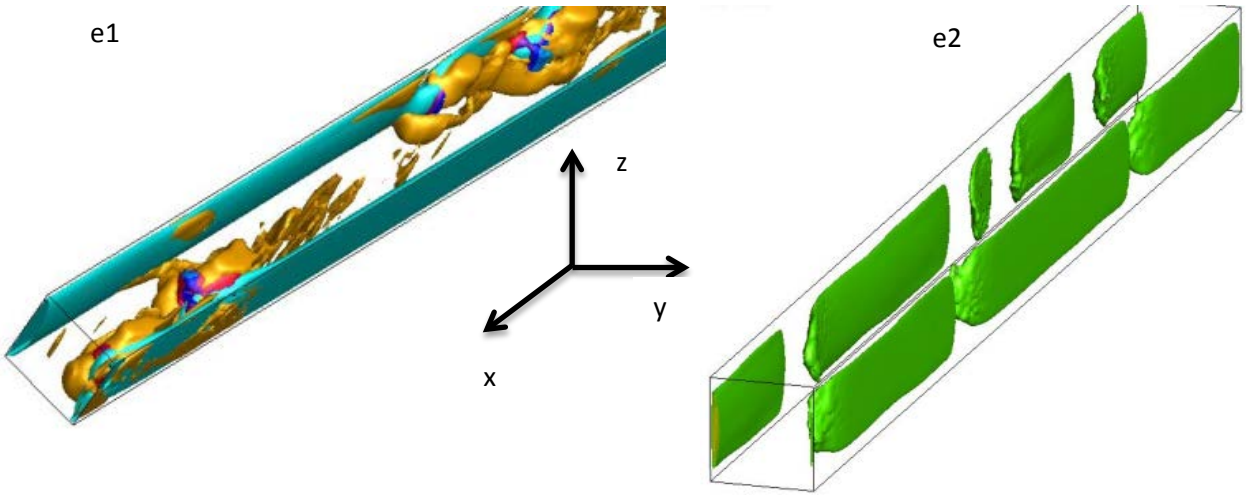

FIGURE 26. (a – e) demonstrates the temporal evolution of jet detachment at *Ha* = 100, *Re* = 1700. **:** Full stream-wise velocity u_x is demonstrated in the (*x, y*)-mid-plane at $z = 0$. Cartoons a, c and d show gradually increasing negative values of the flow which are responsible for jet detachment as they mature. Cartoons b and e show the same image but at a higher grid resolution. The flow is from left to right and the magnetic vector field is perpendicular to the (*x, y*) plane. Cartoon e1 gives a 3 – D representation of the flow including the iso-surfaces of λ_2, CCW (gold), CW (blue) and e2 shows jet detachment in the u_x plane.

It is apparent from the description above that there are two distinct features concerning the jet detachment process: the first being that the CCW vortices must cover a large portion of the outer jet domain in order to be able to slow it sufficiently, not only retarding the fluid, but also lifting it away from the sidewall. The second feature is that the detachment initially occurs one side of the fluid domain, the jet on the adjacent wall is as yet unaffected by the original process. It would therefore be natural to postulate that the jet detachment on the adjacent wall would occur in the same manner. However, through this investigation it has been discovered not to be the case and the proceeding description demonstrates the process in which both jets detach from the side walls, exhibiting a much more complex flow regime than initially thought, Figure 27. The results of this next descriptive development have bought to light an unexpected aspect in the flow, but at this stage it would be injudicious to demonstrate this feature, as the present investigation into jet detachment has yet to be fully concluded.

Continuing from stage Figure 26 (e), the CCW vortices have now lifted the velocity jet away from the side wall and have developed in both amplitude and structure Figure 27 (f). In the proceeding stage Figure 27 (g), two distinct features of the entire development can be observed. The CCW vortices have reached a peak amplitude, completely lifting and separating the fluid within the jet and secondly, due to the complete lift, the geometry of the jet changes, tending to curl the jet in the y-direction. In doing so, the curl of the jet pushes the CCW vortices, housed in the lee of the detached jet, towards and through the core of the fluid. This striking occurrence makes the developing transitional movement non-trivial as now the core of the fluid domain is no longer deemed laminar Figure 27 (h). The CCW vortices in the lee of the detachment shed their inherent KE in the same manner as described in Kolomogros theory. They move across the fluids core and dissipate in KE as they travel, bought about by the Lorentz force attempting to balance the pressure within the system. The CCW vortices travel in the y - direction through the core of the fluid towards the adjacent side wall. As they near the adjacent wall they interact with the smaller CCW vortices which are already housed there, merging together, thus increasing in KE and display the same effect on the adjacent jet as the original Figure 27 (i). The combined amplitude of both sets of CCW vortices are now again strong enough to slow the adjacent jet down, lifting it too away from the side wall. Once this transient phenomenon has concluded , the regime of both detached jets persists for the full duration of the simulation, irrelevant of M Figure 27 (j). Establishing the mechanism which leads to both side wall jets detaching has not been determined in previous studies, ether within a hydrodynamic or MHD flow environment. The specific method continues until Re = 5000 is reached. At this much higher Re value, the flow regime is completely different, but within the parameter $1630 \leq Re \leq 5000$ the transition to a fully turbulent jet regime must be carefully described , as various new flow patterns have been observed on the way to a full turbulent regime which will now be described in the following section

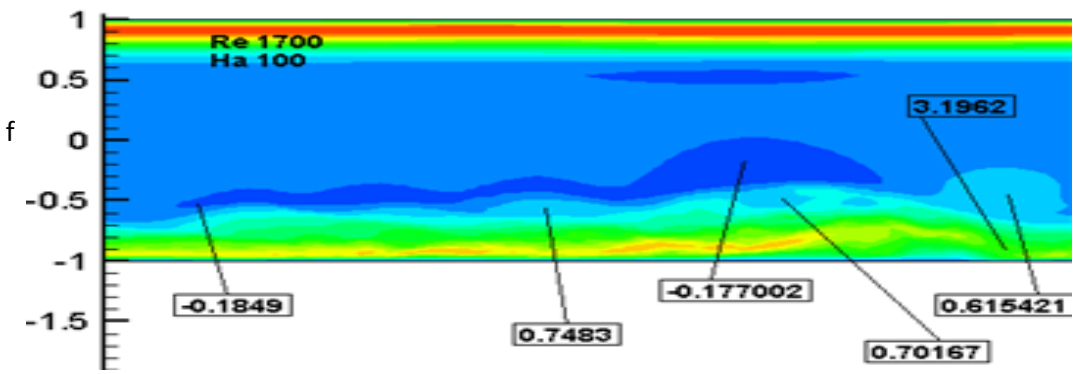

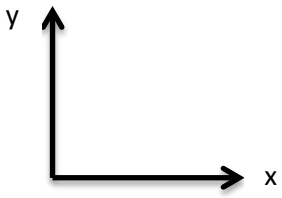
y
x

g

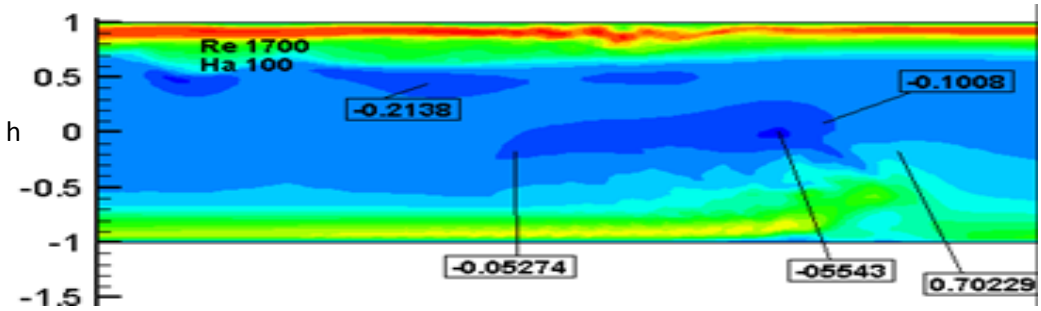
Re 1700
Ha 100
-0.2138
-0.1008
-0.05274
-05543
0.70229
1
0.5
0
-0.5
-1
-1.5

h

I

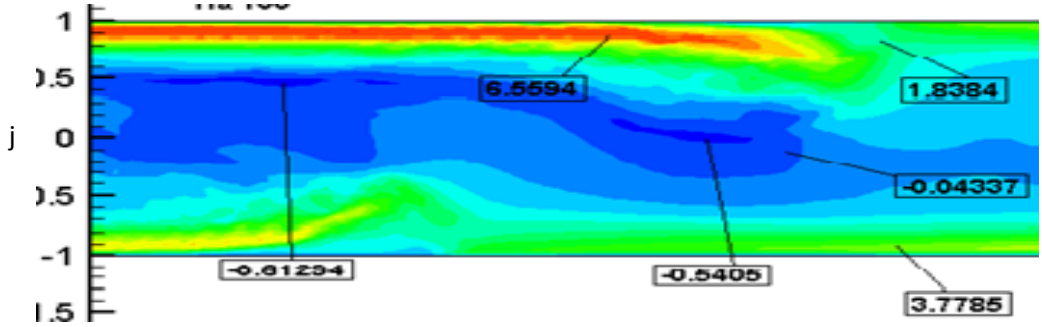
6.5594
1.8384
-0.04337
-0.5405
3.7785
1
0
-1

j

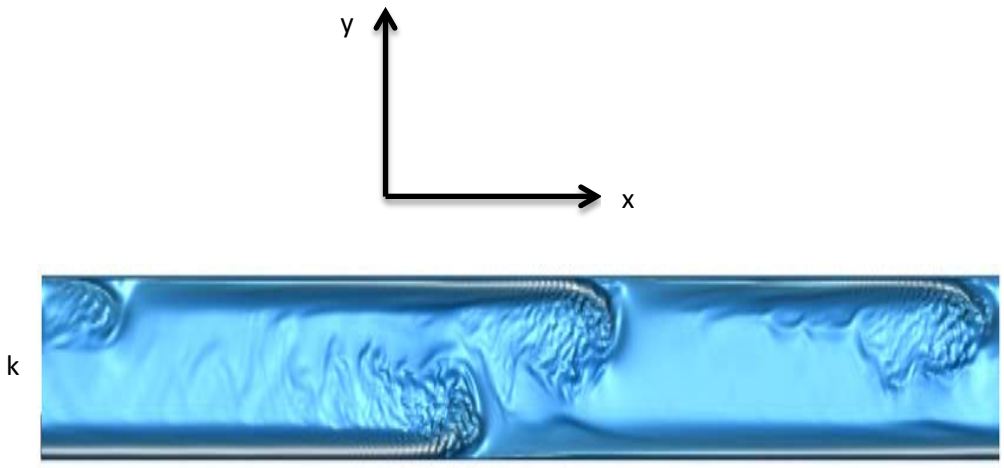

FIGURE 27. Here cartoons (f – j) demonstrate the increasing continuing development of the CCW of the stream-wise velocity component u_x in the (x, y)-mid-plane at $z = 0$ through completion of side wall jet detachment at Ha = 100, Re = 1700. Cartoon (k) displays the final fluid flow state after 1345 CTU. The flow is from left to right and the magnetic vector field is perpendicular to the flow, within flow domain $L_x = 8\pi$. Data points describe the fluids velocity at various points in the flow.

4.5. Higher Reynold Numbers.

A hydrodynamic turbulent regime is well known and verified to commonly occur at $Re >$ 3,500. In an MHD regime however, this can be greatly reduced as the magnetic field suppresses instabilities within the flow. It would be interesting then to determine to what extent the magnetic field does in fact supress instabilities within such a Hunt's flow regime and moreover, attain whether jet detachment persists when increasing to moderate Re values up to a maximum of $Re = 10{,}000$. Therefore to investigate this further, a mirrored approach is adhered to as laid out in the section 4.3. The Re values therefore for the proceeding investigation were now at targeted values Ha = 100, $1{,}800 \leq Re \leq 10{,}000$. The simulations were allowed to develop until they were determined to have reached their individual steady states in the same manner set out in previous sections.

As the results of this additional investigation began to develop, it was viewed that when Re was increased, an additionally unusually flow pattern developed, both within the side domain of the duct and within its core. In section 4.3 it was beheld that jet detachment, once set into

the flow regime, did so in a repetitive almost alternating, staggered formation. But now however, as we increased Re further, their uniformity began to dissipate, forming increasingly multiple staggered detachments on either side of the duct domain, Figure 28.

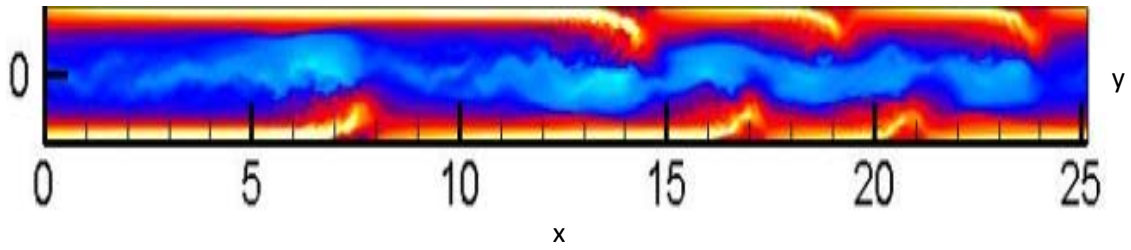

Figure 28. Full stream-wise velocity u_x is demonstrated in the (*x*, *y*)-mid-plane at $z = 0, Re = 1800$, *Ha* = 100. The flow is from left to right. Here we show the increased effect of *Re* as now multiple jet detachments can be clearly seen. Magnetic vector field is perpendicular to the flow, within flow domain $L_x = 8\pi$

The increased number of velocity jet detachments are a result of now multiple CCW vortices in the outer region of the jet, a result of progressively stronger shearing effects at the side walls at *Re* = 2,000 Figure 29 (a). Now, increasing the value of *Re* in incremental steps of $Re = 1000$, we witness the decline in the number of jet detachments. Instead, the jets become increasingly elongated in the *x*-stream wise direction. Even though this phenomenon develops, there persists CCW vortices within the lee of the outer jet region, travelling through the core of the flow domain, shedding vortices in the same manner found at lower *Re* values found in section 4.3, Figure 29 (b). At *Re* = 4000, a distinct difference in the flow regime associated within the side wall instabilities is seen. Here it can be viewed that the jet detachments begin to lose their, up to this point, characteristic profile, instead they now tending to stay closer to the side walls. There is still evidence of continued vortex shedding within the core, but this has also reduced in intensity Figure 29 (c). Increased velocity fluctuations within the side domains are now more apparent and the core is adopting a more laminar profile. The definitive vortex shedding observed at lower values of *Re* is no longer apparent. Moreover, it has been discovered within this study that at a value of $Re \geq 5{,}000$ a

Hunt's Flow regime unequivocally displays fully turbulent side wall jets, with an almost laminar, stabilized core Figure 29 (d).

a *Re* = 2,000

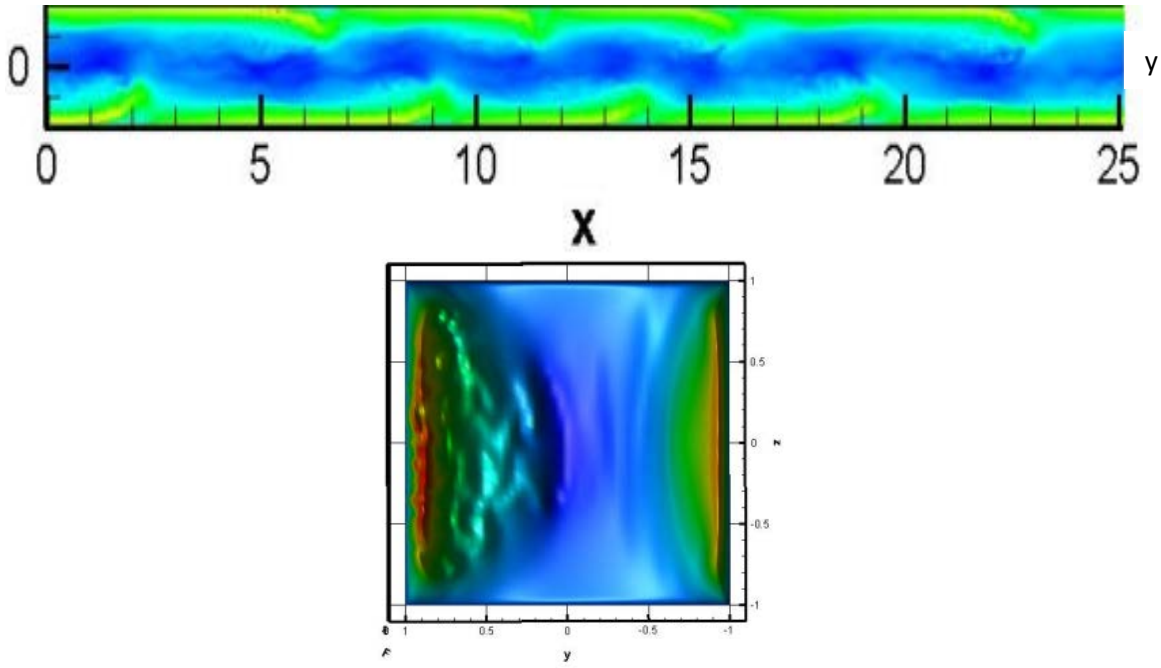

b *Re* = 3,000

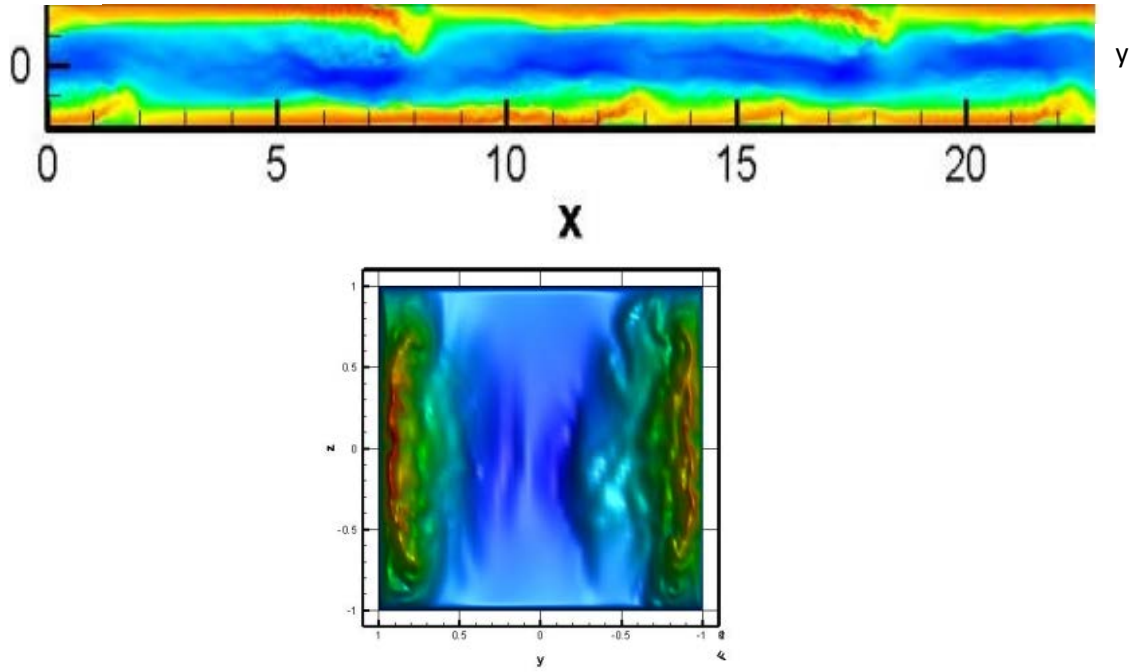

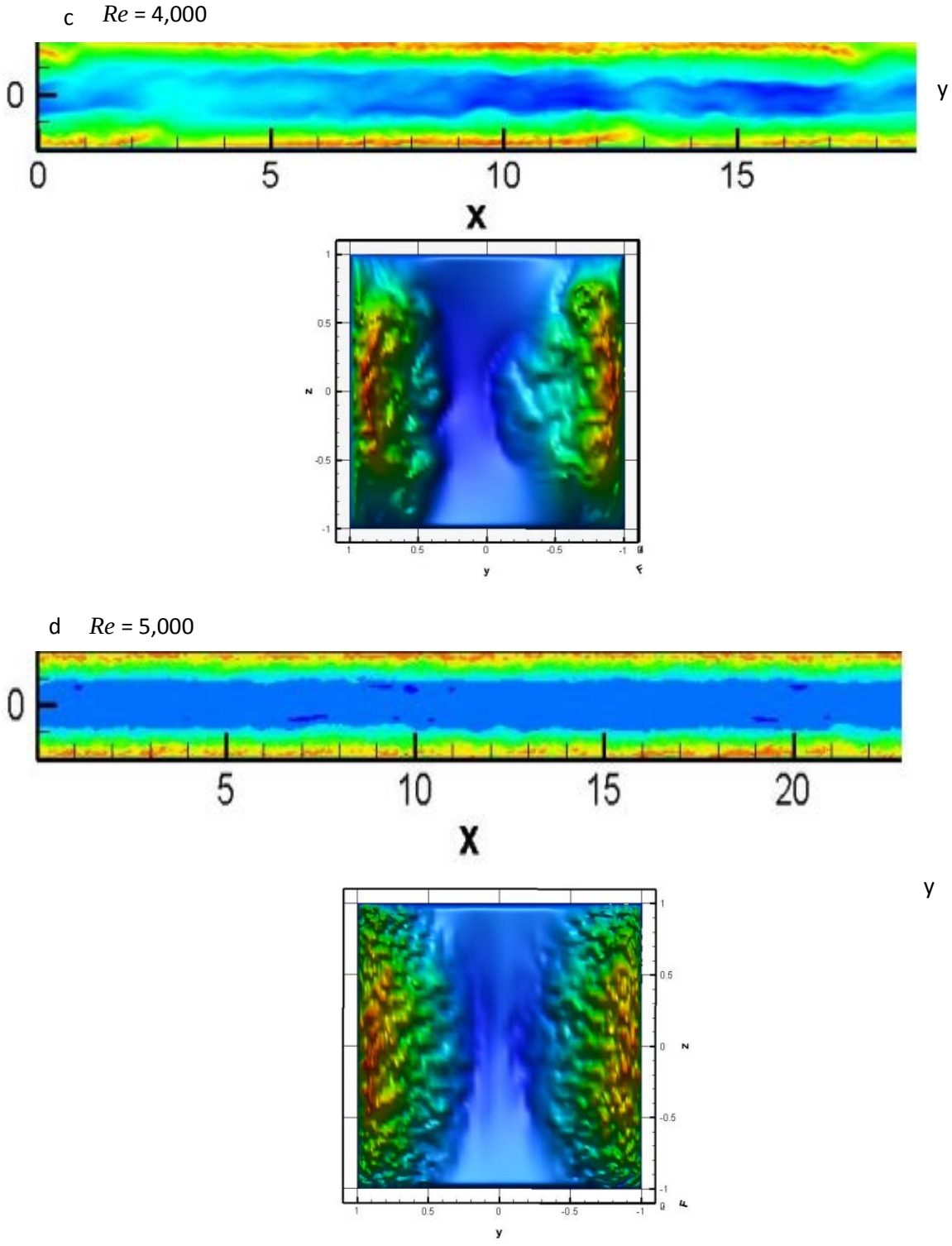

Figure 29. Here, snap shots of instantaneous distribution of stream wise velocity at increasing values of *Re*. Here are shown they ars shown in (y, z) cross-section at $x = L_x/2$, below. Also are shown are the instantaneous corresponding velocity patterns in the (*x*, *y*) mid-plane, *z* = 0, which are visualized by the full scale stream-wise velocity component, above.

Summary

Side wall jet detachment, within a square duct is not a new phenomenon. Previous studies into the occurrence have been conducted with ducts walls being fully conducting $\sigma_w = \infty$, or fully insulating $\sigma_w = 0$. Little work is available on systems where there is a combination of both conducting and insulating walls, i.e. Hunt's flow. This investigation addresses this issue by employing single shot investigations into variable Re parameters with a fixed Ha value. As a result, jet detachment within a Hunt's flow regime has been observed for the first time at $Re = 1{,}630$. Additionally, we have determined there resides an immature band of almost periodic CCW vortices housed within the outer region of the jet domain at $Re \sim 500$. Once Re is increased, the immature CCW vortices develop in both size and amplitude due to strong shearing effects along the outer region of the jet, fluctuating the fluid within this region in the *y*-direction. Ultimately, the temporally evolved CCW vortices partially lift the fluid contained within the outer region of the jet away from the side wall in the *y*-direction. Once partial detachment occurs on one side of the domain, the CCW vortices, now housed within the lee of the partially detached jet, move through the core of the fluid in the *y*-direction, shedding vortices as they travel, a consequence of the residing Lorentz force. Eventually, after approximately 50 CTU, the travelling CCW vortices merge with the adjacent CCW vortices. The KE through this merger is increased and the now merged CCW have the same destabilizing effect on the fluid contained in the adjacent jet, thus bringing about partial detachment here also. Once partial jet detachment sets into the flow, it remains for the entire duration of the simulation. As Re is further increased, i.e. $1630 \leq Re \leq 2000$, we observe multiple partial detachments within the domain, in addition to the detachments losing their almost periodic formation found at lower values of *Re*. In adopting $Re \geq 3000$ the partially detached jets begin lose their characteristic curved profile in the *y*-direction and there is no evidence of the CCW vortices moving through the core of the flow as they did previously. Instead, the jets become increasingly turbulent, tending to stay closer to the side walls, although a historical partial detached jet profile can still be seen. Moreover, the fluid contained within the core of the fluid domain becomes increasingly laminar. At $Re \geq 5{,}000$ the side wall jets are now completely turbulent, in addition to the flow exhibiting a relatively laminar core. The fully turbulent side wall jets continue to exhibit fully turbulent properties at $Re \geq 10{,}000$, the maximum *Re* value attained in this section of the study. The results for *Ha*

= 100 in a Hunt's flow regime demonstrated here have been recently accepted for publication into EPL [130] Appendix A.

4.6. Ha = 200

The investigation carried out within this section is based on the work in a prior study of $Ha = 200$ [102]. In order to attempt to alleviate confusion between the subsequent study and the present, past work stated will be referred to as (P) and the present study will be referred to as (Q). Instabilities at the side wall region observed in P determined jet detachment at $Re \geq 3{,}700$, albeit the conductivity of the duct walls were different to the present study, Q. This section will give a direct comparison between the two investigations, with the view to determining as to what extent differing duct conductivity alters the flow regime and at what flow parameters.

Once the present investigation, Q, had begun to develop early results, it gave a surprising difference concerning the point at which partial jet detachment was first observed. But before the jet detachment comparative can be demonstrated, the study into KE must be first demonstrated, as the imminent presence of any time dependent fluctuations within a flow regime can be confirmed by measuring the three components of KE, i.e. q_x, q_y and q_z. Within P, the mean value of the three separate components of velocity are viewed as a function of Re. From the results documented in P [102], it can be clearly viewed that there are two transitional phases of instability. The first instability threshold is suggested at $1000 \leq Re \leq 2500$ and tends to agree with the results found by Ting *et al* [85]. The second instability threshold witnesses a sharp increase in all three components of KE by two orders of magnitude and is seen at $Re \geq 3500$.At this increase, side velocity jets detach themselves from the duct walls. The KE component closest to the external magnetic field, q_y, was determined to be the weakest component, thus distributing less influence on the mean flow.

If we now study and compare the three components of KE within this present study, Q, we witness a similar instability threshold as in P; in so far as that the sharpest increase in intensity is $1000 \leq Re \leq 2000$ within all three components. Therefore confirming previous instability threshold ranges. It should be gently reminded that within the threshold limits stated above in Q, that there have been three different new flow phenomena: the replacement

of TW vortices by new instabilities, *pike teeth* and jet detachment, making this particular transition point in Hunt's flow development an interesting stage in which to study further. The first comparative difference that we find is that within this particular regime Q, we observe that jet detachment occurs within this first stage of transition and not within the second stage of transition stated in the study of P, a difference of $Re = 1870$. Moreover, as *Re* is increased further, we observe the q_x component continuing to increase by almost another other of magnitude, giving two in total, whilst the q_y and q_z components dissipate. At $Re = 3000$ the q_x component begins to sharply drop by one order of magnitude, whilst q_y and q_z becomes constant and increasing respectively. In fact, as can be seen from observing Figure 30, the q_x component can be viewed has having the greatest amount of KE energy within all differing *Re* values. However, q_z continues to steadily increase between $3000 \leq Re \leq 5000$, thus suggesting an anisotropic flow regime. Upon reaching *Re* = 5,000, all three components essentially do not alter up to *Re* = 10,000. Therefore at $1630 \leq Re \leq 5000$ it can be viewed that this is indeed a second transitional phase in flow development, equally as important as the first transitional stage described in the previous section. It is important because here, within this *Re* range, jet detachments alter their appearance several times until fully turbulent side layers are observed. This result suggests that as in previous work P, there are two phases of transition to turbulence, but at different *Re* values. An interesting result, as once fully turbulent side layers develop in the flow we observe the same flow regime through to $Re = 10000$, the maximum *Re* value used in this section and this can be further observed in Figure 30. However, although the side wall jets become increasingly turbulent as *Re* is increased, the opposite effect is occurring within the core of the flow and will be discussed next

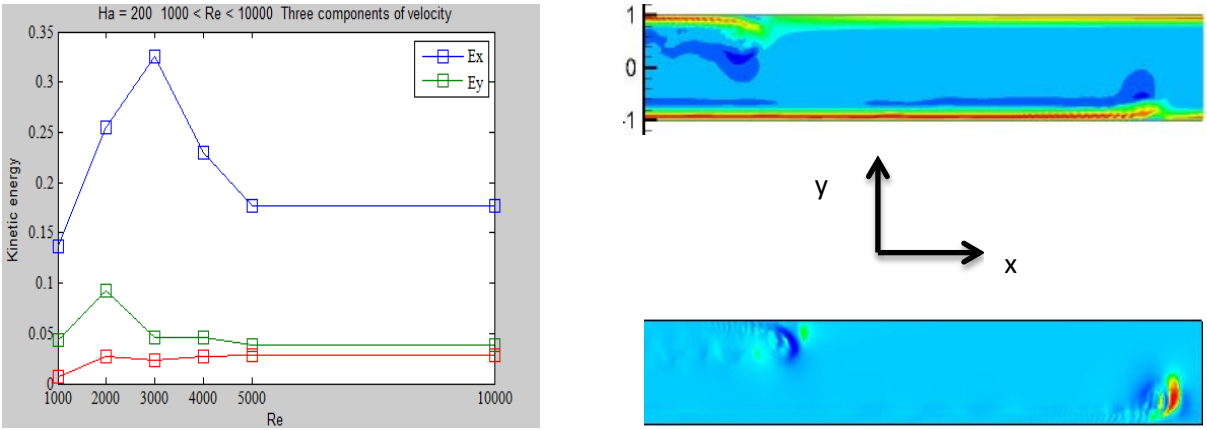

FIGURE 30. Three separate components of KE (Ex^2), (Ey^2) & (Ez^2) are plotted as a function of *Re* (left). Instantaneous snap shot of the full stream-wise velocity u_x demonstrated in the (*x*, *y*) mid-plane cut at $z = 0$, *Ha* = 100, *Re* = 2,000 (right). Grid resolution set at 128^3 (top) and 256^3 (bottom). The flow moving from left to right. Magnetic vector field is perpendicular to the flow, within flow domain $L_x = 8\pi$

In addition to the KE within a system, the pressure gradient produced by different flow regimes is also an important part of any investigation and is a fundamental concern for any proposed system. Within the context of this investigation the pressure gradient is evaluated through the force required to deliver the mass flow rate at a constant value, $-\frac{\partial p}{\partial x} = \bar{f}$. The analytical calculations for this process do not need to be conducted within the scope of this work, as the numerical calculation has been included within the code used. The calculated pressure gradient Figure 31, can be represented as a function of several values of Re. It can clearly be seen that as Re is increased, the pressure gradient within the system also increases. This result ties in with the observation found within the KE investigation and mirrors its result somewhat. At approximately the point of where we observe the first transitional phase, i.e. jet detachment, we witness the sharpest increase in the pressure gradient. The gradient continues to increase, past the second phase of transition through to *Re* = 10000. By studying both Figures 30 and 31 simultaneously, we can determine that the Re value which has most influence on the stability of the Hunt's flow regime, at this particular Ha value is approximately within the first transitional phase, i.e. $1{,}000 \leq Re \leq 3{,}000$. This is not surprising, as the increase in the fluids mean velocity strongly suggests increased stronger instability development within the flow. In should be noted also that the increased pressure

gradient within the system conversely gives rise to a stronger Lorentz force. As the effects within the core of the flow attempts to balance inertia, therefore stronger velocity jets are assumed to develop at the side walls compared to the jets found at *Ha* = 100.

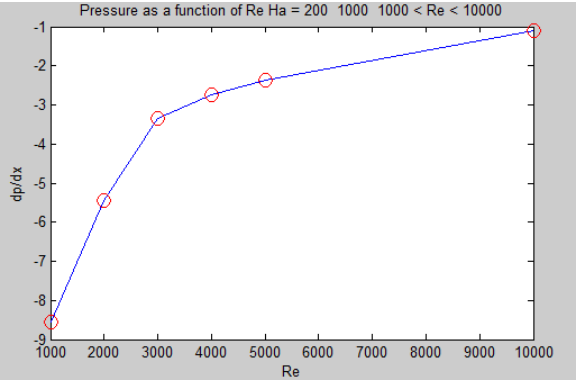

FIGURE 31. Distribution of the pressure gradient as a function of Re for. *Ha* = 200, $1{,}000 \leq Re \leq 10{,}000$.

We will now develop the study further to determine whether the comparative results demonstrated within the KE and pressure gradient investigation do in fact coincide with the two transitional turbulent phases. Also we will demonstrate through Figure 32 (a - e) the effect the Lorentz force has on the flow regime. At *Re* = 1,000 the flow is essentially laminar Figure 32 (a), but as demonstrated In section 4.2, instabilities within the side layers are developing in the form of CCW, both at the outer region and within the jet itself. As we have already seen from Figures 30 and 31 the greatest increase in all three components of KE and pressure gradient can be found at $1{,}000 \leq Re \leq 2{,}000$. Within Figure 32 (a) *Re* = 1000, it is clear that the flow is essentially laminar, although side wall jets and two bands of CCW vortices can be seen residing, however at this stage there is no jet detachment. At *Re* = 2,000 Figure 32(b) there is detachment, but only on one side of the flow domain, At this *Re* value, the movement of the CCW vortices through the core of the flow shown in section 4.1 does not occur, demonstrating the effects a stronger magnetic field has on the flow. Additionally, the study in P stated jet detachment at a much higher *Re* value, i.e. $Re \geq 3500$, a comparative difference of $Re \approx 1500$. Multiple jet detachments however now develop at *Re* = 3000, Figure 32 (c), but coinciding with the increasing pressure gradient and consequently the increasing Lorentz force, the core of the flow regime is now exhibiting a more laminar

appearance, the cause thus justifying the suggested predictions of the KE and pressure gradient graph. A second stage which can be identified in Figure 32 is the observation of multiple detachments from the side walls at approximately *Re* = 3,000 Figure 32 (c), again as is predicted in the Figures 30 and 31. The KE within the system from $5{,}000 \leq Re \leq 10{,}000$ Figure 32 (d and e) is essentially identical, suggesting that the flow at these very different *Re* parameters are very similar. But, this is a surprising phenomenon as the flow regime at *Re* = 5,000 is visually noticeably different, still exhibiting jet detachment compared to the fully turbulent side wall jets shown at *Re* = 10,000.

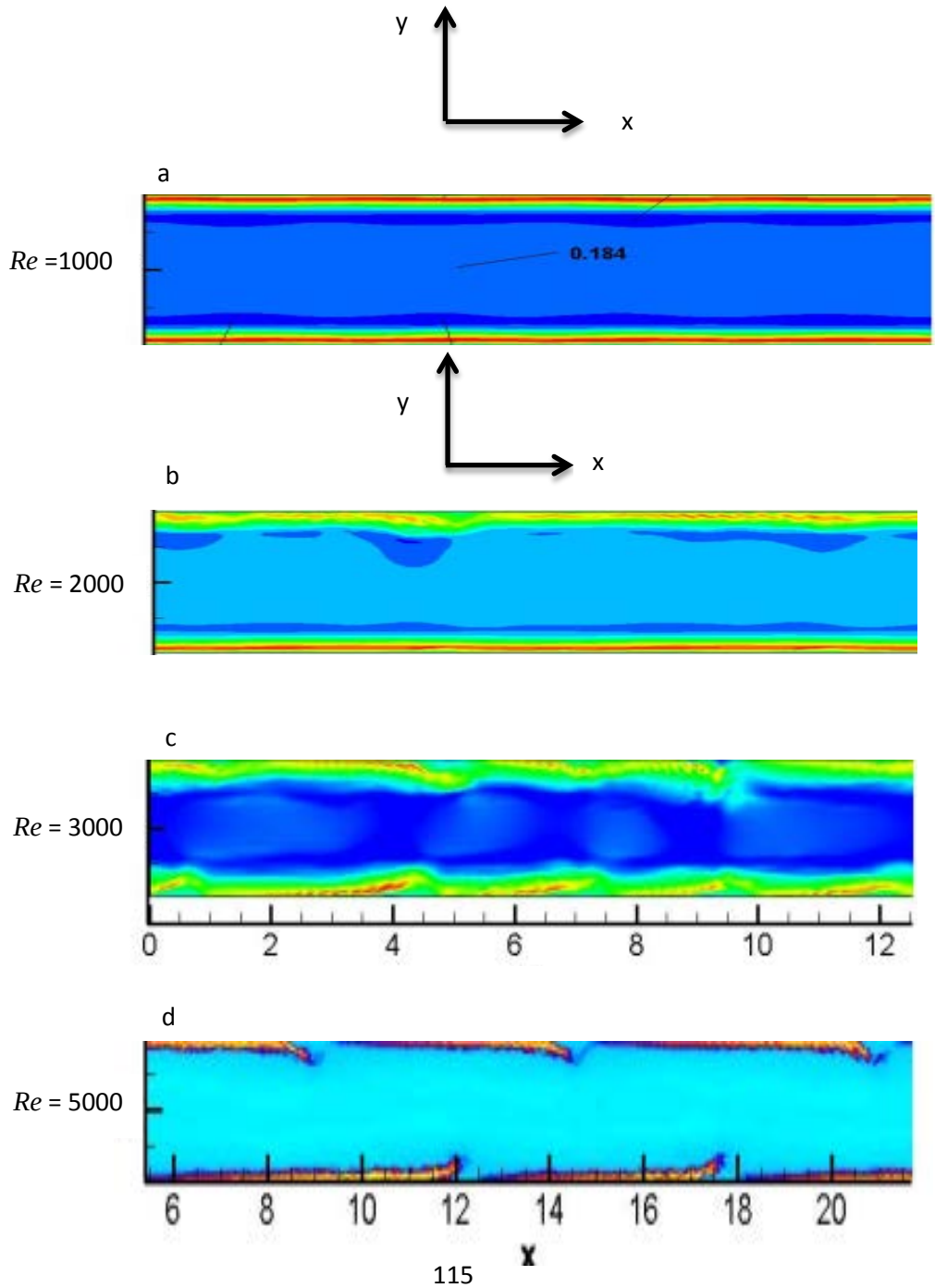

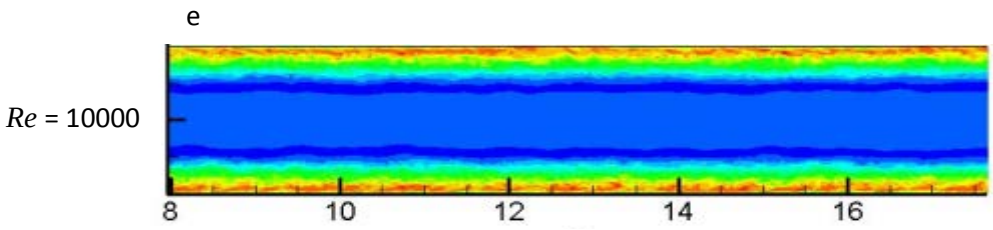

FIGURE 32. Transitional states of jet detachments moving towards fully developed turbulent side wall jets at *Ha* = 200, *Re* = 1,000, 2,000, 3,000, 4,000, 5,000 & 10,000. Instantaneous patterns in the (*x*, *y*) mid-plane are visualized by the full scale stream-wise velocity component. Flow direction is from left to right and the magnetic field vector is perpendicular to the (*x*, *y*) plane

Taking this study one step further, the natural advancement would be to determine at what *Re* value we have jet detachment at $Ha = 200$, having already established the event between $1{,}000 \leq Re \leq 2{,}000$. To this end, four additional simulation were conducted and it was determined that jet detachment was initialized between $1{,}550 < Re < 1{,}600$, this can be seen in Figure 33. The same CCW vortices housed at the outer region of the jet were again responsible for detachment mechanism of both walls.

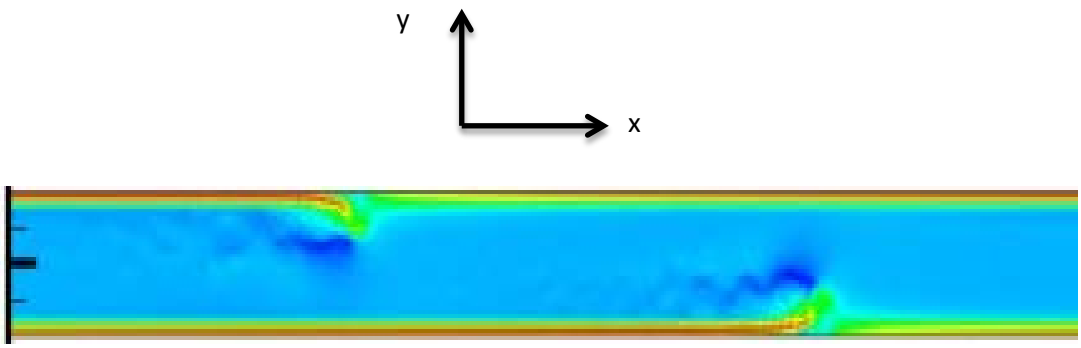

FIGURE 33. Full stream-wise velocity component u_x is demonstrated in the (*x*, *y*) mid-plane at *z* = 0. Jet detachment is witnessed for the first time in a Hunt's flow regime at *Ha* = 200, $1{,}550 < Re < 1600$. Vortex shedding is also observed in the lee of the detachment (dark blue). Flow is from left to right

Summary

Therefore to briefly summaries what has been observed so far in this section: the initial graphs in this section Figures 30 & 31, predicted that instabilities within the flow would be observed in the temporal mean velocity flow at approximately $1{,}000 < Re < 3{,}000$, thus bringing forth instabilities. Having determined the KE and pressure gradient predictions, we then progressed to the visual representation of the flow regime in the x- stream wise direction at the z = 0 plane. The observations demonstrated within the graphs, Figures 30 & 31, proved to coincide with Figure 32, demonstrating a change in regime from a laminar state to a turbulent regime through the occurrence of side wall jet detachments, re-confirming that any time dependent fluctuations within a flow regime can be confirmed by measuring the three components of KE. By evaluating the results in Q, we can now make a direct comparison to the results obtained in P. Within P, a rectangular cross sectional duct was used with a wall conductance ratio of $c = 0.7$, which to all sense of purposes exhibits a fully conducting duct. Initial conditions comprised of a non-MHD regime, which after temporal evolution, the magnetic field was applied, i.e. Ha was implemented. The results witnessed in P demonstrated that the values of $Re \ll 1{,}000$ TW vortices were present at the side walls. Increasing $2{,}500 \leq Re \leq 3{,}500$ P*'s* study witnessed the three components of velocity increase to values between 10^{-5} to 10^{-4}. Assuming that the stability threshold for P was between these Re values. At $Re \geq 3{,}700$ the study conducted in P witnessed a sharp increase in the full scale KE fluctuations, which eventually lead to jet detachment. Jet detachment was witnessed for the first time not only at these parameters, but the first time in its entirety.

The situation however has changed within this present study, Q. We still witness an essentially laminar flow regime $Re < 1{,}000$, but where this study differs is the stage in which instabilities are detected in the KE profile. The values witnessed here show the transition to turbulent instabilities at values of $1{,}000 \leq Re \leq 3{,}000$. In addition to this, the present study has determined that jet detachment from the side walls has occurred at $1{,}550 \leq Re \leq 1{,}600$, this is almost a 90% difference compared to P*'s* study. As Re is further increased, multiple jet detachments are witnessed, eventually leading to fully turbulent side wall jets similar to that observed at Ha = 100. The present study can therefore demonstrate the importance and influence that the wall conductance ratio has on the mean velocity profile, noticeably the implementation of insulating walls and perfectly conducting Hartmann walls. As we have now made direct comparisons to earlier studies in MHD flow, it would be natural

to embark on a comparable investigative into one's own research. We have already demonstrated the differing flow instabilities and phenomena for two *Ha* values, but to give an even better, more rounded comparable account, *Ha* = 300 will be now investigated and a full comparison between all three values of *Ha* will be given.

4.7.Comparing low to moderate Ha values.

Contained within this section will be the comparative study of three different Ha values. We have already demonstrated the differing flow regimes for $Ha = 100 \,\&\, 200$, therefore rather than separately demonstrate an additional Ha value, we will combine all three values into one complete study. The aim of which will be to construct direct comparison between all involved. This particularly different approach to this section, one feels, will better demonstrate the differing mean flow regimes that each Ha value brings. The comparative will include the previously applied initial conditions set out in the sections which included $Ha = 100 \,\&\, 200$ and Re parameters will also mirror the previous studies within this thesis. For the sake of continuity, the temporal flow simulation will be given towards the end of the study, first focusing on the inherent vital contributors to a turbulent regime. All comparatives will be set into the same graphical results, thus giving the reader an increased dynamic pattern in determining the results gained. The values which will be compared in this section will be $Ha = 100, 200 \,\&\, 300$, $1{,}000 \leq Re \leq 10{,}000$.

Beginning with the study into the pressure gradient within each regime: the greater the effects of $\boldsymbol{J} \times \boldsymbol{B}$, the greater the pressure distribution throughout the flow regime. This can clearly be viewed in Figure 34. Interestingly though, as the value of Re increases, the pressure within each regime begins to dissipate rather sharply at the initial stages, then eases, this is done at an almost identical rate for each Ha value. If by purely studying the Figure 34 alone, we would assume that if Re was increased even further than is demonstrated here, that the pressure gradient contained within all three Ha values would eventually converge to the same Re value. This situation though is at present beyond the scope of this thesis and should be investigated further to see if low-moderated *Ha* value regimes do in fact converge into the

same pressure gradient. If however, assuming that we have the information to make such a statement, then this would suggest that the pressure within a system would eventually be the same, irrelevant of Ha. At present it can only be determined on an assumption.

Therefore the pressure gradient within the system is predictably the greatest at the highest level of *Ha* investigated here, as one would expect. We can assume, using the information provided Figure 34, and the fact that the Lorentz force is reduced at the side walls because of insulation properties, that one would expect to see elongated side velocity jets compare to *Ha* = 100 & 200 velocity profiles in the same *x*-stream wise direction. By making this initial assumption we can plot the differing time and domain averaging velocity profiles as mid-plane cut in the *z* = 0 plane, Figure 35.

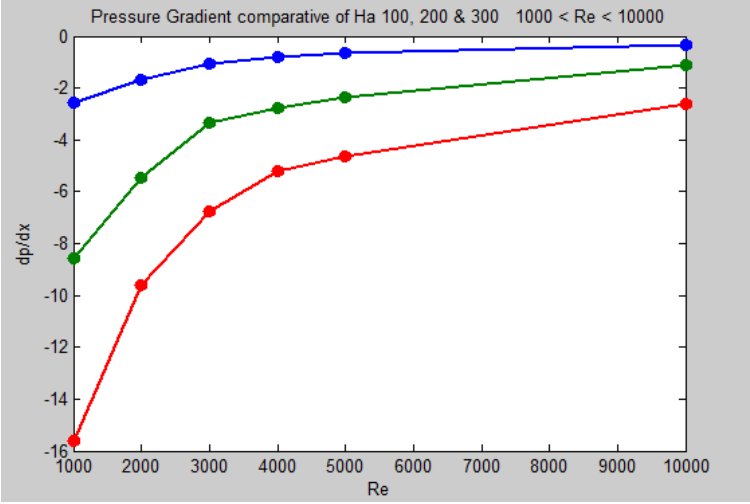

FIGURE 34. Here we demonstrate the pressure gradient distribution, $\partial p/\partial x$ for $1000 \leq Re \leq 10000$, Ha = 100 (blue), 200 (green) and 300 (red) as a function of *Re.*

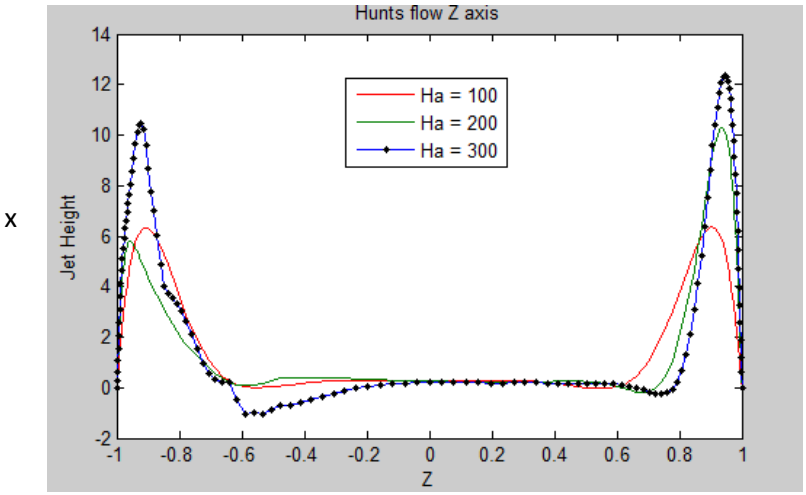

FIGURE 35. Comparative results for laminar Hunt's flow for *Ha* = 100 (red), 200 (green) and 300 (blue), *Re* = 1,000. A basic velocity profile along the *y* – direction demonstrating the effects of the varying strength of the magnetic field on the flow. The resolution in the (*y*, *z*) plane is 256^3points, grid clustering is set by hyperbolic tangent with stretching coefficient $A_y = 3.0$ and $A_z = 3.0$ in the *y* and *z* directions correspondingly.

Here the visual representation of the jet profile differs to the investigations in $Ha = 100\ \&\ 200$, in so far that Figure 36 demonstrates the mean velocity profiles as a function of *Ha*, rather than *Re*. The predicted increase in the length of the velocity jets at *Ha* = 300 stipulated earlier can be viewed as being justified. It should also be noted that the width of the velocity jets has decreased in size also, due to $\boldsymbol{J} \times \boldsymbol{B}$. Later on in this study will be an in depth analysis into the width of velocity jets at differing N & Re values: to determine whether the predicted scaling laws demonstrated in [82] do in fact scale to $N^{-\frac{1}{3}}$. Presently, initial results into this particular scaling law are somewhat contradicting. Revisiting Figure 35 we also note that the velocity jet on the left hand side of $Ha = 300$ is distorted and does not follow the same smoother pattern as $Ha = 100\ \&\ 200$ for the same $Re = 1000$ value. This demonstrates the initial evolution of a turbulent regime at *Ha* = 300, which would suggest that this is the second different observation within this comparative study. The three figures on the right Figure 36, all demonstrate a dip in the velocity profile at the base of the outer region of the jet. The dips are attributed to the reversed flow in the regime. Therefore if there is reversed flow, it strongly suggests CCW vortices and this can evidently be seen in Figures 36.

Ha = 100, *Re* = 1000

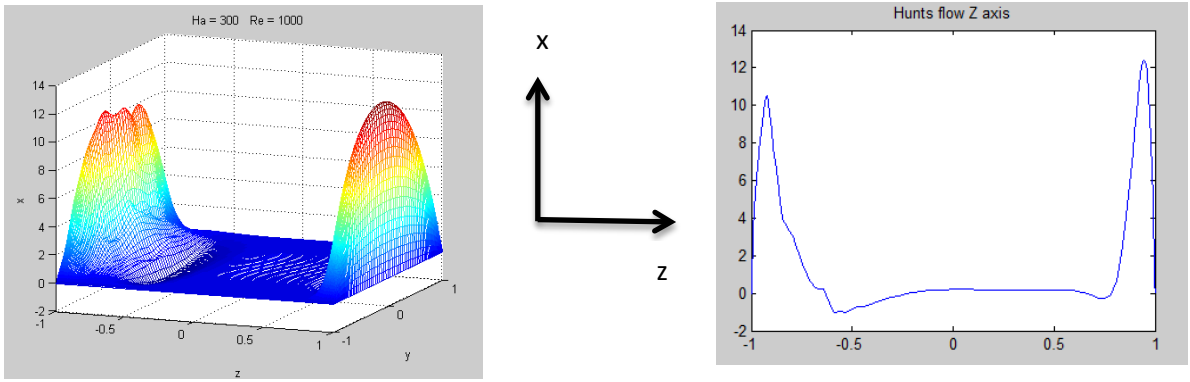

Ha = 200, *Re* = 1000

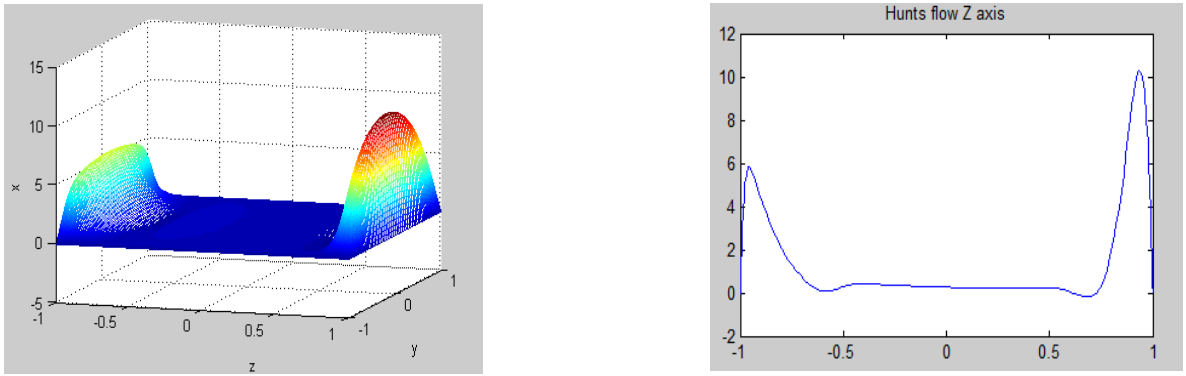

Ha = 300, *Re* = 1000

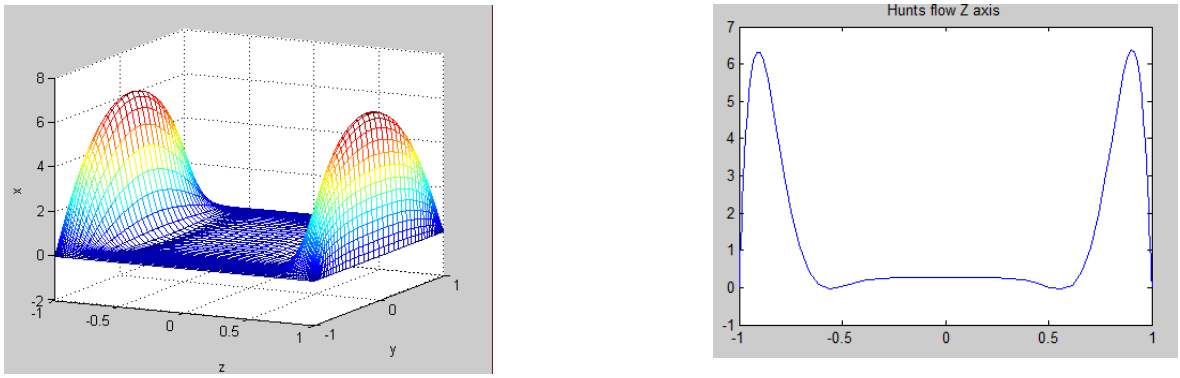

FIGURE 36. Instantaneous snap shot of comparative velocity profiles for varying values of *Ha* and fixed *Re* value. We demonstrate mid-plane cuts at $x = 0$ (left), $z = 0$ (right).

Having now confirmed our initial assumptions, we can progress further to study the KE comparatives within the collective regime. As the KE within a system is a by-product of the shearing effects within a flow, the rise of therefore demonstrates the developments of instabilities. Also, the KE can be used as an indication as to which direction, either *x*, *y* or *z*, the strongest vortices travel. To accomplish this study then we will present the three separate components of KE, i.e. E_x, E_y & E_z all as functions of *Re.* By adopting this approach, it will demonstrate the spread of KE throughout the flow regimes as the velocity of the fluid and magnetic fields are increased Figure 37. If we take for example component E_y, Figure 37 (b), this is particularly interesting due a sharp initial increase in KE for all values of *Ha,* but once the regime achieves $Re \geq 2{,}000$, the KE within the regime dissipates. But surprisingly, begins to rise again, further suggesting additional instabilities within the flow, reaching a peak at $Re = 5{,}000$ for all Ha values. The $Ha = 100$ regime suddenly drops dramatically revisiting 0 again, thus demonstrating no kinetic energy within the regime. This is however a little confusing as we already know that at this Re value the $Ha = 100$ regime witnesses' fully turbulent side wall jets and an essentially laminar core. $Ha = 200$ on the other hand has a second peak at $Re = 5000$, but the drop in KE here is more gradual, which is what you would assume to be the outcome. This begs the question as to why the $Ha = 100$ KE regime reverts back to 0, knowing from our previous results that at higher values of Re, we observe a fully turbulent regime in the side walls. The two separate components, E_x& E_y both demonstrate a reduction in KE in the flow regimes as we progress past *Re* = 3,000. This indicates that once the flow regime has achieved a fully turbulent state and the Lorentz force has damped out large amounts of turbulence within the core of the flow, the KE contained within dissipates monotonically. Another interesting observation, through the monotonic dissipation, which was too witnessed in Figure 37, was that if the values of *Re* were increased, both E_x & E_y components would eventually reach the same *Re* value, i.e. approximately zero. By further postulating that the KE contained within these two particular components would indeed tend to zero, then that would indicate that the liquid metal contained within the blankets would have the same amount of inherent KE as water in the stream-wise and span-wise directions , thus behaving as such. But this is speculation and a more detailed, extended *Re* investigation is required to verify this large assumption. The last component E_z, behaves differently for each separate *Ha* value once past *Re* = 2,000. Once past this *Re* value all *H*a regimes demonstrate anisotropic behaviour, steadily increasing until *Re* = 5,000 is achieved. *Ha* = 100 then drops sharply, but this would coincide with the fact

that at *Ha* = 100, *Re* = 5,000, the flow regime is deemed to exhibit fully turbulent side wall jets and an essentially laminar core. Therefore the anisotropic vortices at this higher Re value would become saturated.

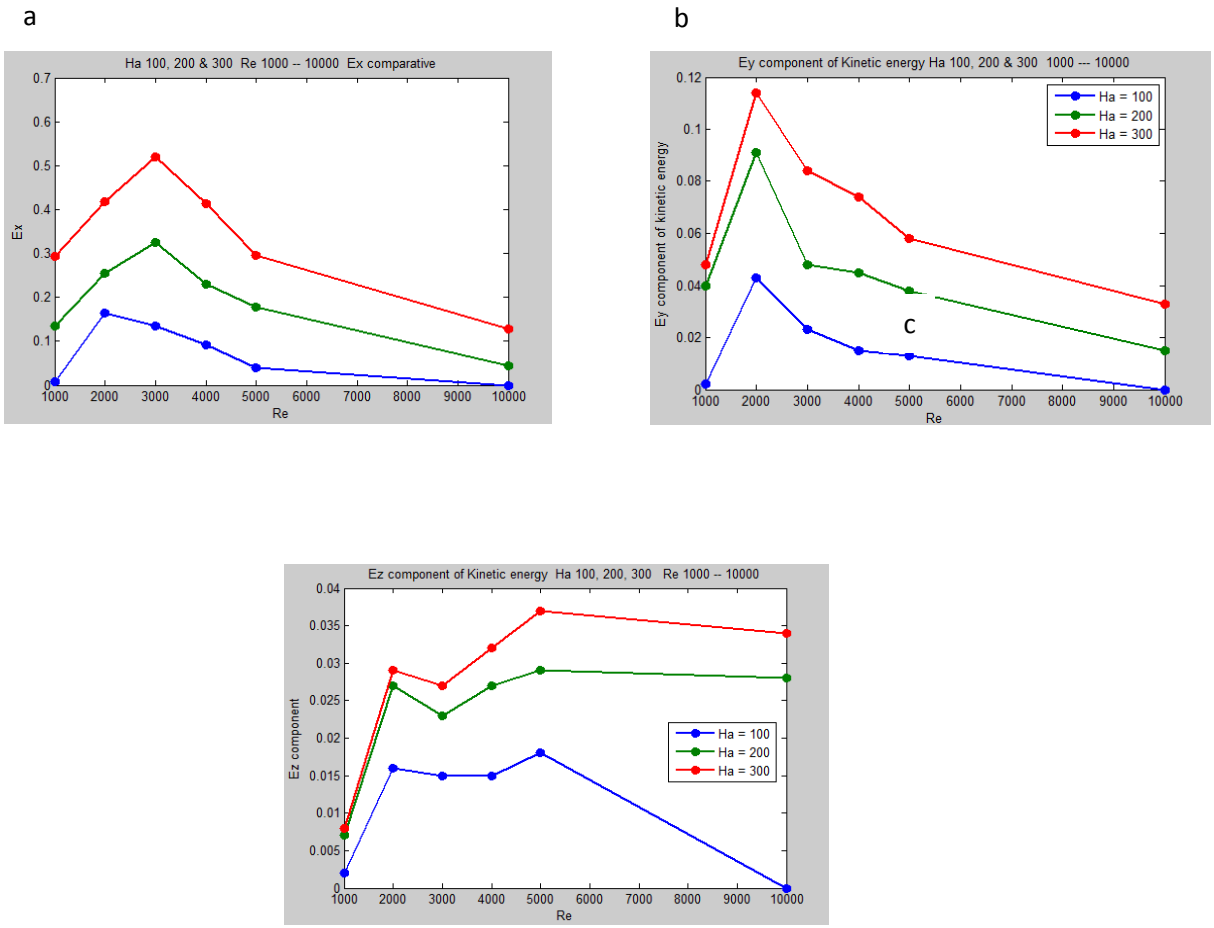

FIGURE 37. Three components of KE E_x (a), E_y (b) & E_z (c) comparative as a function of *Re* at *Ha* = 100 (blue), 200 (green) & 300 (red).

4.8. Jet Width

The thickness of the velocity jet, δ_j, produced within a Hunt's flow regime has historically yet to be fully resolved. Within previous studies [82, 102] investigations have been somewhat un-decisive, even though a jet thickness scaling law of $N^{-\frac{1}{3}}$ has been presented. Therefore there is a certain amount of confusion surrounding this issue. The method for determining this elusive parameter stipulated within [82, 102] has included taking measurements from the duct wall to a tangent line at the inflection point of the mean velocity profile along the $y = 0$

axis. Within this study, the measurement method of δ_j has been done differently. Instead of employing a tangent line applied to the inner region of the jet and calculating the distance from the tangent line to the wall, it has been determined that although this method has been met with some success, once we enter into flow regimes where we experience fully turbulent velocity profiles at higher Re values, the method is inadequate. Therefore in order to overcome this difficulty, we have derived a method which allows the width measurement to alter along the $y = 0$ plane. The reason for this is to allow a certain amount of freedom in attaining the point in which the jets, within the entire study, could be optimally measured.

In addition to the jets being measured within the $y = 0$ plane, Figure 38 (a), an additional study was undertaken which include the measurement of the jet in the $z = 0$ plane also, i.e. from one Hartmann wall to another Figure 38 (b). This inclusive step has been included to enable a more rounded approximation to the theoretical physical appearance to the jet. The aim is to determine if scaling laws in the context of this study for *Re, Ha & N* parameters can be found, either confirming previous results, or presenting new findings.

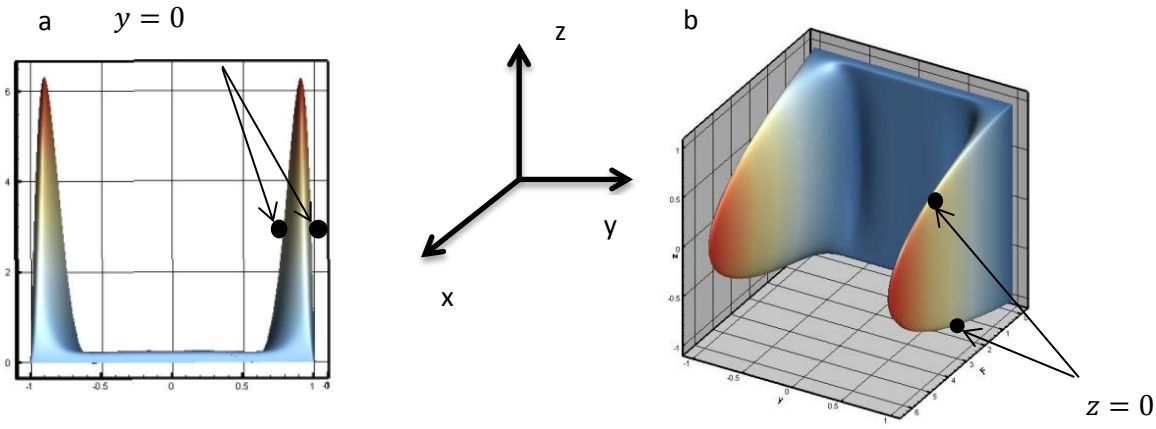

FIGURE 38. Instantaneous velocity profiles in the *x* - stream-wise direction at *Ha* = 100, *Re* = 1000 demonstrating jet measurement method.

This supplementary investigation was conducted via two separate approaches and the data required to carry out this additional study was obtained from the observations carried out in an extensive hysteresis test and as single shot studies. Full results on the hysteresis tests are not included within this work. But once the results of this extensive test have been completed, an academic paper will be produced. One believes that by employing two separate methods, it would further justify any results that may be achieved. Therefore initially, we studied the jet

width as a function of *Ha* in both *y* & *z*-directions as single shot studies. Our set parameters were *Re* = 2,000, *Ha* = 10, 100, 200, 300, 800 and 2,000. As all investigative data was collated, converted to log scaling for asymptotic clarity, super imposed onto a linear fit and plotted, it was observed that as a function of *Ha* there was very little evidence to suggest a linear fit, and thus, subsequently a power law between the thickness of the velocity jet in both the *y* & *z*-directions Figure 39 (a). Upon initial results, a further six studies were carried out to determine if the results at *Re* = 2,000 extended to *Re* values ranging from $500 \leq Re \leq 10{,}000$, using the same *Ha* values as before. The results from the additional six *Re* studies also demonstrated that there is very little evidence to suggest a linear fit to the data for a wide range of *Re* values as functions of *Ha*. The next progressive step forward was to determine whether there was some type of linear fit by switching the study and investigating the jet width as a function of *Re*. Therefore, *Ha* was fixed and the width of the jet plotted against $500 \leq Re \leq 10{,}000$. As we have now moved the study to become a function of *Re*, both the increasing and decreasing data gained from the previous hysteresis investigation could now be included also and it is this which was studied first. As both increasing and decreasing hysteresis data was plotted, results demonstrated that at lower values of *Re*, i.e. $500 \leq Re \leq 2{,}000$ there again was no real correlation to a linear fit. But within the same data set, at higher values of *Re*, i.e. $2{,}000 \leq Re \leq 10{,}000$ the results suggested a good correlation in the *y*-direction, Figure 39 (b). Therefore, the lower *Re* values were omitted from the study and the higher *Re* values were investigated further. Upon plotting the higher *Re* values only, an essentially clear straight line was observed in the *y*-direction. In the *z*-direction, the linear fit data is not so convincing, but this is to be expected, as the velocity jets as *Re* increases becomes increasingly turbulent and anisotropic. It can be seen that there is a very good correlation between the *Re* values and the linear fit of both increasing and decreasing data sets, Figure 39 (b & c), including single shot investigations. Having established an initial visually good fit, it suggested that there was evidence a scaling power law contained within the results could be possible, therefore a further analysis was thus conducted. Due the fact that we are implementing the width of the jet against *Re*, R^2 was used to determine its variability in the *y*-direction against the model, in this case the *Re* values. A small Matlab code was thus wrote to achieve this and the results demonstrate a strong argument that the power law scales to $Re^{\frac{1}{4}}$ for this particular senerio are presented in Table 3(a). The jet width in the *z*-direction does not conclude to the same result, instead, the results are inconclusive, as the average result for a perfect fit is $1.22Re^{0.0401}$, this can be viewed in Table 3(b). The

investigation was extended to include the data from the single shot investigations and the results in both the *y* & *z*-directions essentially matched the results found in the hysteresis results.

a

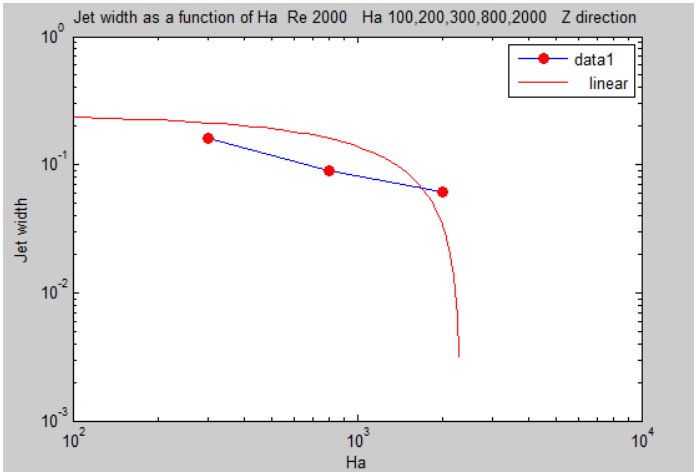

b

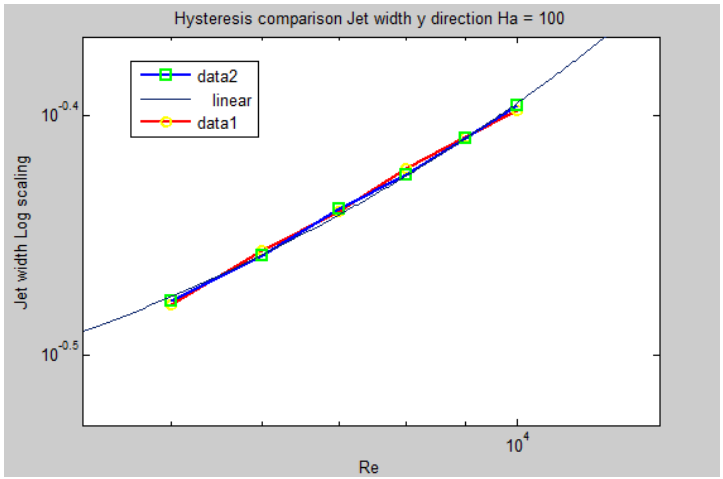

c

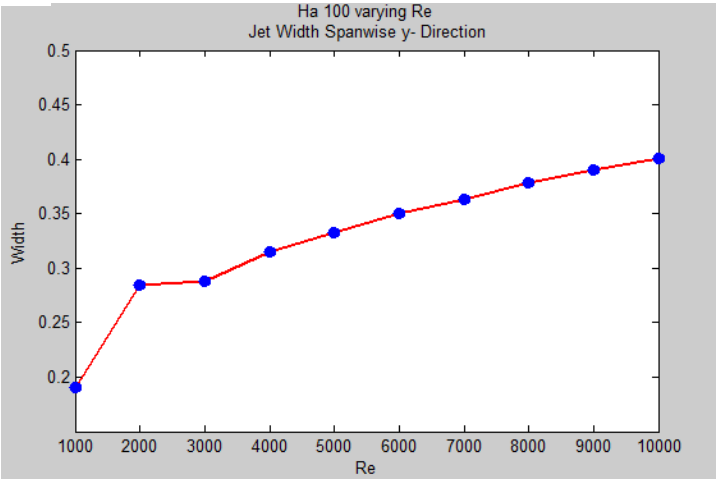

FIGURE 39. Here jet width comparisons are plotted as a function of *Ha* (a) and of *Re* (b) for increasing and decreasing hysteresis data. Plot (c) demonstrates the increase in jet width, again as a function of *Re* in the *y*-direction.

Table 3(a) Jet thickness as a function of *Re* in the *y* plane

Direction	Points	Perfect fit	R^2	Approx fit	R^2
y-up	6	$0.03327\mathrm{R}e^{0.2703}$	0.9991	$0.03988Re^{0.25}$	0.9936
y-up	5	$0.03406Re^{0.2677}$	0.9984	$0.03994Re^{0.25}$	0.9941
y-up	4	$0.03337Re^{0.2700}$	0.9967	$0.03998Re^{0.25}$	0.9913
y-up	3	$0.04016Re^{0.2497}$	0.9999	$0.04005Re^{0.25}$	0.9999
y-down	6	$0.03271Re^{0.2721}$	0.9984	$0.03985Re^{0.25}$	0.9919
y-down	5	$0.03039Re^{0.2803}$	0.9987	$0.03989Re^{0.25}$	0.9872
y-down	4	$0.03077Re^{0.2789}$	0.9971	$0.03996Re^{0.25}$	0.9865
y-down	3	$0.02574Re^{0.2984}$	0.9999	$0.0400Re^{0.25}$	0.9736

Table 3(a). Here we demonstrate the thickness of the velocity jet in the *y* plane from the results gained from the hysteresis investigation. The perfect fit column represents actual data points. Approximate fit represents a forcing study to determine the correlation against *Re.*

Table 3(b) Jet thickness as a function of *Re* in the *z*-plane

Direction	Points	Perfect Fit	R^2
z-up	6	$1.224Re^{0.03972}$	0.9864
z-up	4	$1.224Re^{0.03974}$	0.997
z-up	3	$1.22Re^{0.04013}$	0.9919
z-down	6	$1.26Re^{0.03657}$	0.9919
z-down	4	$1.209Re^{0.04112}$	0.993
z-down	3	$1.183Re^{0.04346}$	0.9868

Table 3 (b). Represents the jet width in the z plane for increasing data points. The approximate forcing procedure has not been conducted here as there is little relevant correlation with *Re*.

To conclude: the width of the velocity jet within MHD duct flow regimes has been historically studied and through earlier investigations [82], have resulted in a scaling power law, i.e. $N^{-\frac{1}{3}}$, which has been regarded as a stable fundamental results for many years within the MHD community. This present investigation has been targeted to either confirm these prior results, or suggest a new power law based upon a Hunt's flow regime. From the early resulting data achieved by this additional investigation, through a multitude of different simulations, there is strong evidence to suggest conflicting results to that stated in earlier investigations [82].

By implementing an R^2 study, we can conclude that the scaling power law stipulated in this study is $Re^{\frac{1}{4}}$ (i.e. $N^{-\frac{1}{4}}$). By approaching the problem from different angles and achieving essentially the same concluding results, we can confidently state that the power law given here is conclusive for *Ha* = 100. In order to verify the conclusion even further, additional studies have been undertaken at increased *Ha* values to determine the same law, but as these results have yet to be concluded and will not be presented in this work. Once the further investigation has been accomplished, the results of which will be published.

5. High Hartmann, Ha = 800 & 2000.

Within previous chapters, the investigation into the differing flow regimes of a conducting fluid subjected to low externally applied magnetic fields, i.e. N = 1, 4 and 9 respectively, has been extensively conducted. Included within this chapter, we now turn our attention to the study of differing flow regimes of a conducting fluid subjected to high external magnetic fields, $Ha = 800\ \&\ 2000$, i.e N = 64 and 400. At these higher Ha parameters we are beginning to approach magnetic fields commonly found in nuclear fusion environments, i.e. $Ha > 4{,}000$. A vital commonality running through this study in its entirety has been the strict adherence to identical initial conditions and methodologies, as inherent comparative studies could be concluded upon in the full knowledge that all simulations, whether employing high or low parameters, would result in a well-rounded comparable approximations of fluid flows and transitional phases. The simulations therefore in this chapter have again been carried out at a fixed Ha value to a single shot targeted Re number, mirroring the methods employed in chapter 4.

For continuity, we begin with the lower of the two high Ha values, i.e. $Ha = 800$, giving a full description of the various flow regimes at this parameter, progressing later on through to $Ha = 2{,}000$. The Re values used at $Ha = 800$ are $100 \leq Re \leq 20{,}000$. At $Ha = 2000$ however we investigate a slightly different range, $500 \leq Re \leq 10{,}000$. Both Ha values will be studied as separate regimes, culminating in a comparison towards the end of the chapter. Although we have already witnessed new and interesting flow regimes in previous chapters, as we develop this study further, we again observe new and interesting flow regimes. However, as we progress it will become evident that there are similarities which can be found at lower Ha regimes.

5.1. Ha = 800.

Throughout the temporal evolution of each flow simulation studied so far, a particular structure has demonstrated commonality, the presence of TW vortices at the initial phase. Here, at $Ha = 800$, we observe TW vortices repeatedly. There is however a striking difference in the TW vortices observed at this higher Ha value, compared to those found at lower Ha regimes. The TW vortices are still observed close to the side walls, but they now

appear to be elongated in the x - direction, Figure 40 (a). This phenomenon cannot be attributed to the increase in fluids velocity, as their stretched appearance is observed at the lower end of *Re* values implemented, i.e. $Re = 100$. Therefore, an alternative phenomenon must be responsible for their stretched appearance. By increasing the value of *Ha*, consequently, we have increased the MHD interaction within the flow regime, which in turn is having a much greater effect on the flow.

Through completion of the first flow simulation at $Re = 100$, it is evident that now stretched TW vortices again quickly disappear after approximately 10 CTU, but unlike the flow regimes described in chapter 4, there is no evidence of new instabilities emerging once the TW vortices have disappeared. The flow after this short transient period becomes completely laminar, exhibiting no instabilities and no side wall velocity jets. The Lorentz force completely dominates the regime, Figure 40 (b). By increasing to $Re = 200$, we again see the appearance and disappearance of the stretched TW vortices at the side walls, for approximately the same amount of CTU as at *Re* = 100, but now, we see the re-emergence of the same new instabilities found at *Ha* = 100, 200 & 300. There is however one striking difference. At this *Re* parameter, the new instabilities do not occupy 80% of the flow region, instead they predominantly occupy the side walls, perpendicular to the external magnetic field and not penetrating the core, which was observed in Chapter 4. This particular regime categorically demonstrates the effects of a completely laminar core, bought about by strong MHD effects which reside there, i.e. the Lorentz force, Figure 40 (c). No further instabilities develop and once this pattern sets in, at approximately 80 CTU, the flow regime does not alter through to completion at 540 CTU. At *Re* = 300 we finally witness the growth of the new instabilities proceeding the disappearance of the TW vortices. The new instabilities now penetrate the core, occupying approximately 60 – 70% of the domain, similar to that witnessed at lower *Ha* values found in chapter 4. Therefore this suggests that the Lorentz force does not have the same influencing effect on the regime at this particular parameter. After 100 CTU, the new instabilities have completely spread through the regime and continue to fluctuate until the simulation has completed at 520 CTU. It should also be mentioned at this point that small localized areas of CCW vortices reside in the outer region of the jet domain which are beginning to influence the fluid within the jet, which results in non-periodic, infrequent partial jet detachment, different in appearance to that found at lower *Ha* values. However, the detachments which do occur do not follow the same pattern found at *Ha* = 100. Here the CCW vortices do not travel through the core, instead they only effect the side

wall jets where they initially reside. A completely different phenomenon bought about by the increased presence of the Lorentz force, Figure 40 (e)

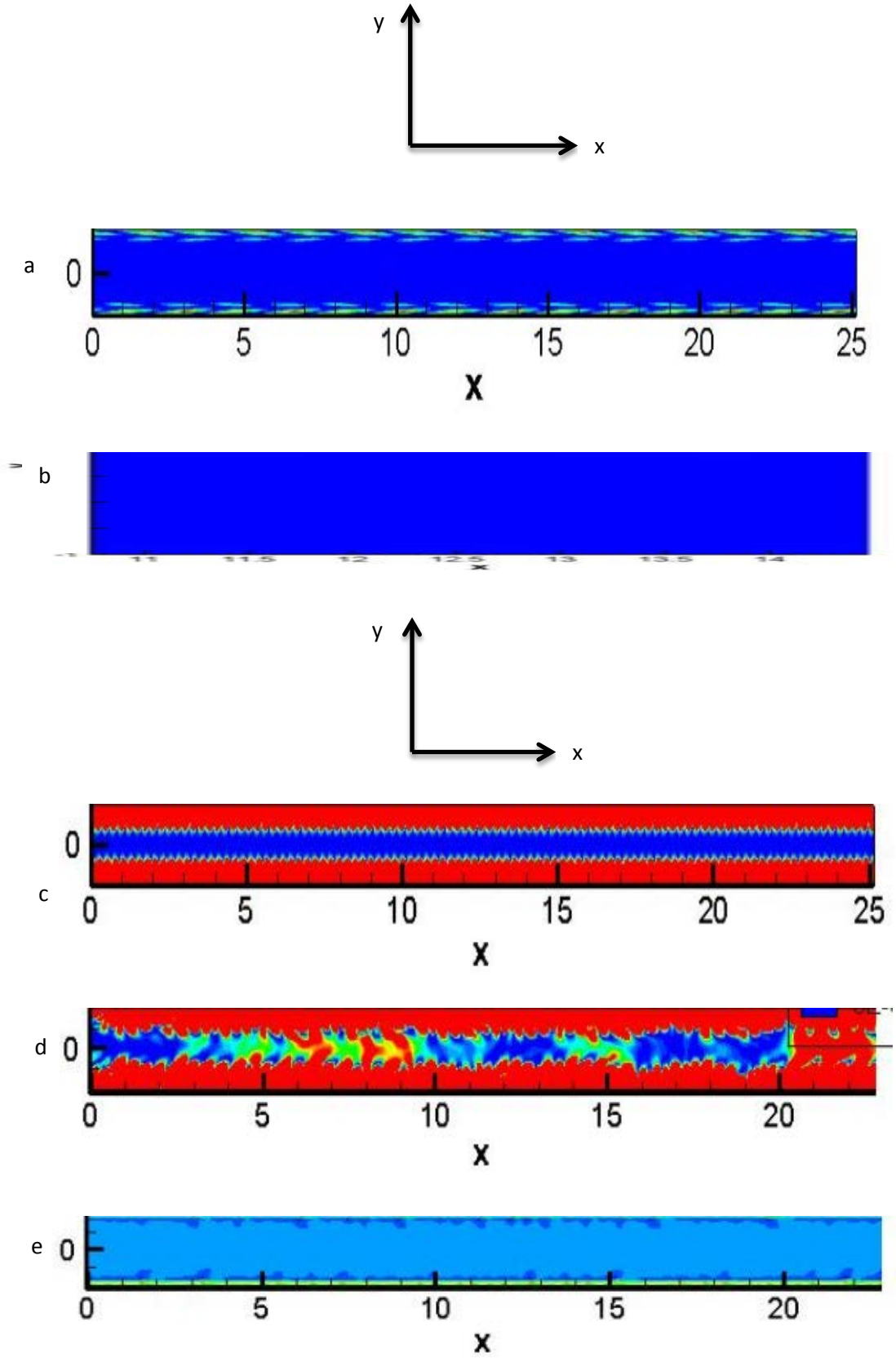

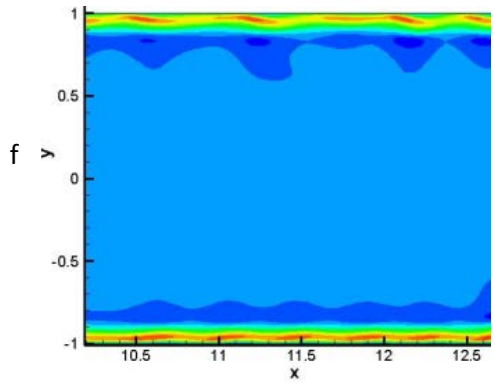

FIGURE 40. Snapshots of the flow from left to right at the plane, z = 0. The fluctuating components of kinetic energy $q =< u_x^2 + u_y^2 + u_z^2 >$ are demonstrated at *Ha* = 800 (a) *Re* = 100, (b) *Re* = 200, (c) *Re* = 300, (d) *Re* = 400. U_x is demonstrated at *Re* = 400 in its entirety at (e) and closer at (f).

Emphasis at this point should be put onto the term *partial*, as at this *Re* value, the fluid within the jet has not fully lifted away from the side wall and there is no total separation of the flow within the jet domain, Figure 40 (f). Increasing slightly to $Re = 500$, the CCW vortices at each side wall have increased in KE, lifting the jet away from the side wall, resulting in total separation of the fluid within the jet, the characteristic observed at *Ha* = 100, Figure 41 (a - b). Here however, at this higher *Ha* value the method of jet detachment differs to that observed at lower *Ha* values. The CCW vortices movement through the core of the flow, interacting with the adjacent CCW vortices, seen lower *Ha* values is not observed. The method now has changed somewhat; Instead, the CCW develop separately at each side wall without moving through the core Figure 41. The same phenomenon which was observed for *partial* jet detachment at *Re* = 400 This phenomenon can only be adhered to the strong effects that the Lorentz force has on the flow, totally inhibiting the movement of the CCW through the core, keeping them close to the side walls. We may conclude then, that the jet detachments observed at *Ha* = 800 and within the range of $100 \leq Re \leq 500$ are totally decoupled, exhibiting thin, turbulent side wall jets detachments and an essentially laminar core.

The transitional phases of temporal flow development at *Ha* = 800, $500 \leq Re \leq 1800$ do not alter dramatically to that which was just described at $100 \leq Re \leq 500$, but as *Re* = 2000 is

reached an additionally interesting development occurs: a slower CW vortex is observed underneath the jet at the point of fluid separation. Throughout the entire investigation, this is the first time that a CW vortex has been observed within such an area.

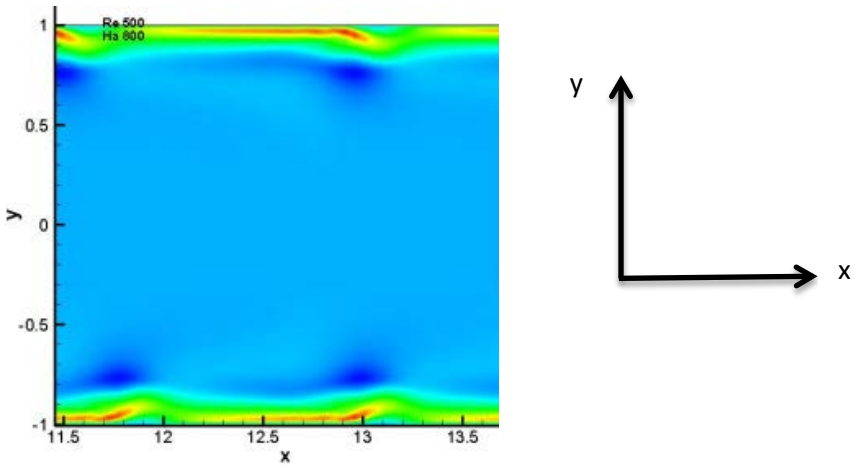

FIGURE 41. Contours of velocity component U_x moving from left to right in the (x, y) mid-plane at z = 0 at *Ha* = 800, *Re* = 500. CCW vortices (dark blue) tend to stay closer to the side walls, without moving through the core.

Moreover, we now have a regime where there are multiple jet detachments, adjacent to each other in an almost periodic formation, similar to the regimes demonstrated at lower *Ha* values in Chapter 4 Figure 42 (a). Again, the multiple detachments have been the result of the intense, localized CCW vortices at the outer jet region, but like the regimes at $100 \leq Re \leq 500$, the CCW vortices have not moved through the core of the flow. At the point where the jet totally detaches itself from the side wall we have already stated that there is a CW vortex underneath the detachment, but also there is another dramatic observation. As can be seen in Figure 42 (b) at the point of fluid separation, the leading edges of the jets change their characteristic representation. In other words they become increasingly turbulent, exhibiting additional instabilities. At *Re* = 10000 the velocity jets have lost their parallel, periodic formation found at *Re* = 2000, however they continue to demonstrate turbulence at their leading edge and through the entire length of their separated domain. By focusing in on their inherent structure it can be clearly seen that there are pairs of CCW vortices rotating around each other in a CW rotation (need to put a figure in showing this). The CW rotating vortex

seen underneath the leading edge of the jet detachment at *Re* = 2000 is also seen at *Re* = 10000 but there is still separated jet detachment at the comparative *Re* = 10,000 value with regions of slower CW vortices at the leading edge, Figure 42 (b). It is a common occurrence so far at this *Ha* value that the CCW vortices responsible for jet detachment do not move through the core of the flow due to the increased Lorentz force and at Re = 10000 this is also the same. Instead they stay increasingly closer to the side walls, elongating in the *x* - direction, Figure 42 (b). This results in an increased laminar core in the *y* – direction. Progressing through the *Re* = 20000, the highest *Re* value studied, jet formation at the leading edge is becoming increasingly turbulent and the jets themselves are becoming increasingly elongated in the *x* – direction and their width in the *y* – direction has decreased. As can be clearly seen at the bottom of Figure 43 (c), there are distinct CW rotating vortices underneath the leading edge of the jet.

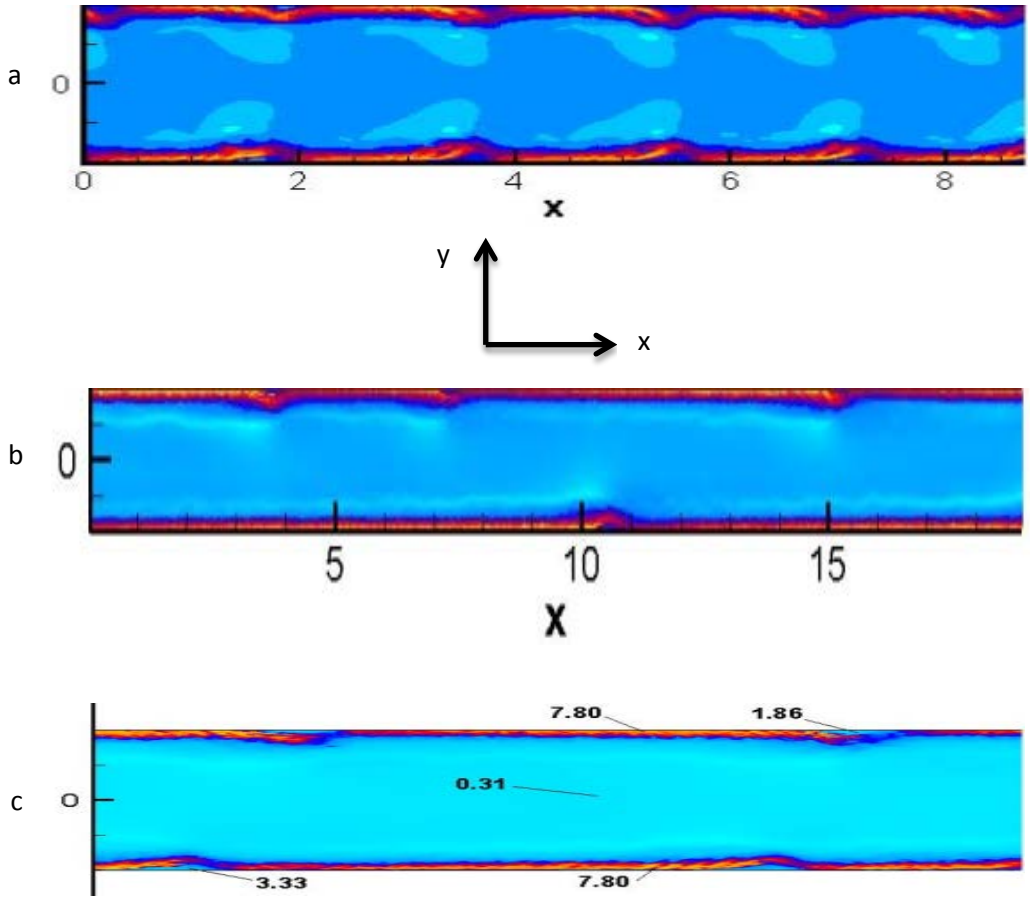

FIGURE 42. Full stream velocity U_x is shown in the (x, y) mid-plane cut at z = 0 for (a) *Re* = 2000, (b) *Re* =10,000 & (c) *Re* = 20000, *Ha* = 800. Flow is from left to right. (c) shows pin point fluid velocities at various areas in the flow.

As well as the visual representation of the flow regime extensively demonstrated above, the three components of KE contained within each differing flow regime must be analysed to confirm the amplitude of the inherent vortices and the transitional phases of the flow. This additional study will be done as a comparative investigation at the end of this chapter.

5.2. *Ha* = 2000

By studying the flow regime at the highest *Ha* value within this entire investigation, we are beginning to approach the realistic working environment set within a thermo nuclear fusion reactor. Therefore this particular sub-section will be of particularly interests if we are to determine the Hunt's Flow regime as a proposed liquid metal blanket cooling system for nuclear fusion reactor environments.

We begin the study at the benchmark *Re* value employed almost throughout the entire investigation, $Re = 500$. Immediately, as with other differing flow regimes investigated in this study, TW vortices are present at the initial temporal evolution of the regime. In fact, throughout the remainder of this $Ha = 2{,}000$ study, TW vortices have been present at all *Re* values at the initial stage for every simulation. It can be postulated that within this particular Hunt's flow study, in its entirety, TW vortices are essentially a common feature and contribute to the first transitional phase to a turbulent regime. This investigation has proved this to be an accurate statement. However, we have also discovered that the transition to turbulence enters different transitional phases which are highly dependant upon the value of *Re* and *Ha*, thus the Lorentz force Therefore it can be suggested that TW vortices are regarded as the first onset to a turbulent regime, subjected to a combination of critical *Ha* and *Re* values. The range at which *Re* was studied in this chapter mirrors that set out in Chapter 4. The decision for ensuring $Re \leq 10000$ was mainly due to computational costs, in addition to keeping strict consistency policies for post processing the other flow parameters.

For the moment one will remain with TW vortices as new additional instabilities have been observed at their outer region at simulation parameters $Ha = 2000$, Re = 500. After only approximately 5 – 10 CTU, the TW vortices columnar structure appears to be stretched in the x-stream-wise direction Figure 43 (a), similar to their formation found at Ha = 800. Within this particular regime though, as we approach 30 CTU, two small additional periodic rows of CCW vortices are seen at the outer region of the TW vortices, similar to the structures found at Ha = 100, Re = 1450, i.e. *pike teeth.* These new instabilities remain in the outer region of the TW vortices for approximately 40 CTU before the KE contained within the regime increases amplitude and spreads throughout the flow occupying 80 – 90% of the domain. The development of the KE here almost mirrors that to what was observed in chapter 4. The second appearance of the small additional CCW vortices in between the transitional phases further iterates the suggestion that they could in fact be the catalyst to intensify the KE contained within the TW vortices, eventually being responsible for the KE spreading through the entire duct domain, Figure 43 (b - c).

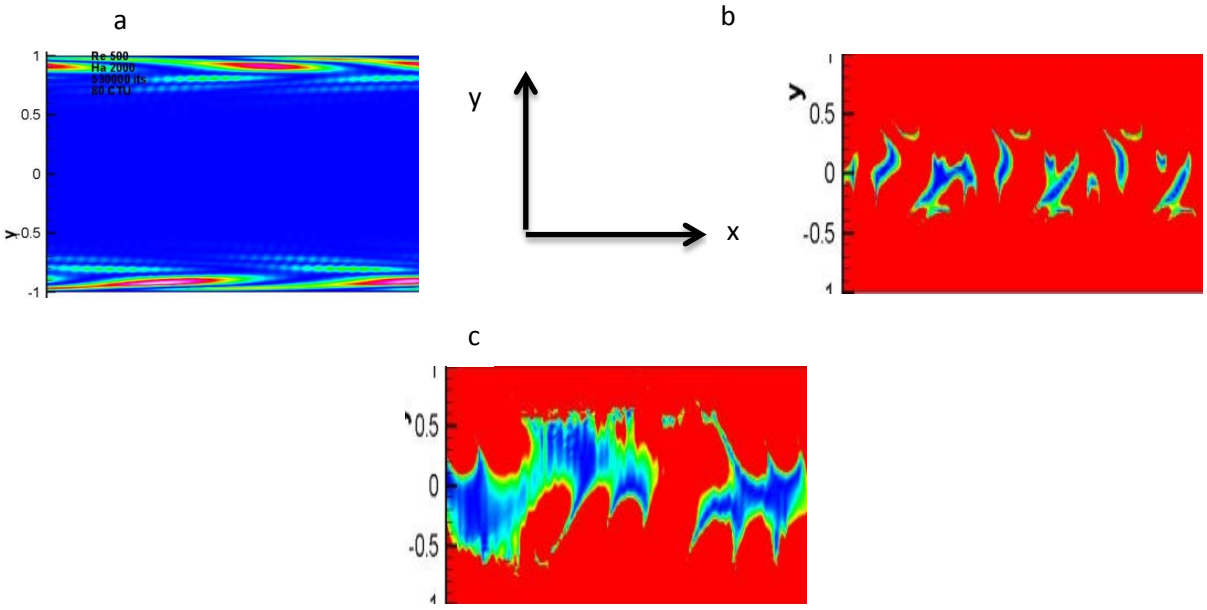

FIGURE 43. Close snap shots of $q_t = u_y^2 + u_z^2$ in the z = 0 plane, Ha = 2,000, Re = 500. Demonstrated is the stretched appearance of the TW vortices (a) and the temporal evolution of the new instabilities (red) spreading through the duct domain (b) & (c).

At this particular Ha value, *partial* jet detachment, the emphasis again on *partial*, occurs at the lowest Re value we have investigated, $Re = 500$. It is observed again that the CCW

vortices are the main instigators for reducing the velocity of the fluid within the jet, but they exhibit a different behaviour than their turbulent appearance observed at $Ha = 800$ for the same *Re* value: in so far as they are now small periodic structures located at each side wall, in an almost parallel formation. Although the CCW vortices have retarded the fluid within the jet, as of this point they are not sufficiently strong enough both in size and amplitude to cause flow separation within the jet, thus not fully detaching the jet from the side walls. Therefore at $Ha = 2000,\ Re = 500$, we confirm that there is *partial*, but not full jet detachment Figure 44. The core of the flow has been completely laminarized by the strong Lorentz force which resides there.

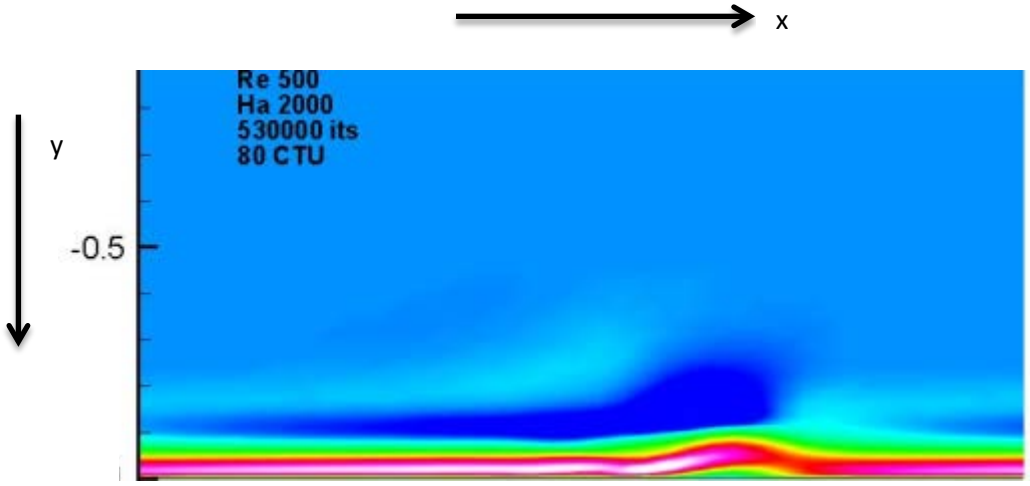

FIGURE 44. A close up snap shot of velocity U_x in the mid-plane z = 0, fluid flow is from left to right. The CCW vortices (dark blue) are shown not to fully separate the velocity jet (pink) at *Re* = 500, *Ha* = 2,000.

The flow regime alters however as *Re* increases to $Re = 1{,}000$. The temporally evolved CCW vortices retain their periodic formation for the time being, Figure 45 (a) and have developed to cover extended areas of the fluid within the jet. As the flow develops over time, the extended CCW vortices cause flow separation within the fluid of the jet, thus fully lifting the jet away from the side walls. But yet again, the CCW vortices do not move through the core of the flow and only develop as each separate side wall. At $Ha = 2000, Re = 1000$ we can now confirm that we have full jet detachment from the side walls. In section 5.1 we demonstrated that at *Ha* = 800, a small CW vortex was found underneath the leading edge of the jet detachment and stated that this was the first time that this CW vortex had been

observed. At this higher *Ha* value, we again see the same CW vortex underneath the point of jet detachment Figure 45 (a). In fact, the CW vortex is inherent to all *Re* values studied at this high *Ha* value, but as will be demonstrated later, the CW vortex has an increasingly turbulent effect on the leading edge of the jet, similar in manner to the turbulent effect shown at *Ha* = 800. Progressing to $Re = 3{,}000$ a different flow regime temporally evolves: interestingly the periodic, almost parallel CCW vortices found previously have now bunched together in groups of approximately fourteen smaller separate entities in an alternative formation at the side walls. At approximately 100 CTU, the unusual alternating formation sets into the flow and remains for the full duration of the simulation Figure 45 (b). By studying the KE contained within each individual vortex, it has been found that there is a slight incremental build up, beginning with the leading partial detachment through to the last in the series, Figure45 (c) as the fluctuating transverse velocity component is q_t is measured. The flow behind the last partial detachment demonstrates short periods of laminaization which can be visually seen within Figure 45 (c) and through measuring the fluctuating velocity component u_x^2. Once this alternating bunching pattern sets in, it continues through to completion. It must be noted that this is the only *Ha* and *Re* values that demonstrate this unusual pattern. Thus the jet detachments at *Re* = 3,000 can now be characterised as train detachment, with the length comparable to the computational domain. The reason as to why we have this particular new train detachment flow regime is still unknown and requires further investigation.

The flow regime at $Re = 4{,}000$ observes a change once more Figure 45 (d). If however we briefly remind ourselves of previous flow regimes by reverting back to lower levels of Ha & Re, jet detachment is seen to take a curved, almost smooth geometry as it leaves the side wall and moves in the y – direction towards the core. At $Re = 4{,}000$, *Ha* = 2,000 however, the leading edge of the detachment has altered, exhibiting the same turbulent appearance found at *Ha* = 800, even though full detachment is still observed Figure 45 (d). By focusing our attention upon this leading edge, we begin to see a brake up of the fluid within the jet, a resultant of small areas of increased CW and CCW vortices, Figure 45 (e). Moreover, underneath the leading edge, a CCW is present, which is different to the CW vortex found at *Ha* = 800 Figure 45 (e) . It can be postulated that the presence of the CCW vortex underneath the leading edge aids the turbulence within this region Figure 45 (f). The same leading edge turbulent regime can also be observed at $Re = 5{,}000$ & 10,000.

Progressing to the final and maximum *Re* parameter used at this *Ha* value, i.e. *Re* = 10,000, the grouping of the CCW vortices seen at *Re* = 3,000 & 4,000 have disappeared, replaced by a flow regime exhibiting an ordered periodic formation again, witnessed at lower *Re* values Figure 45 (g). *Partial* detachment is attained, but not full detachment. It should be noted at this point that throughout the entire *Ha* = 2,000 study, there was not a single CCW vortex that moved through the core of the flow. In fact, the core of the flow remained essentially laminar throughout. Therefore the CCW vortices have achieved partial and full jet detachment in a different manner to that observed in Chapter 4.

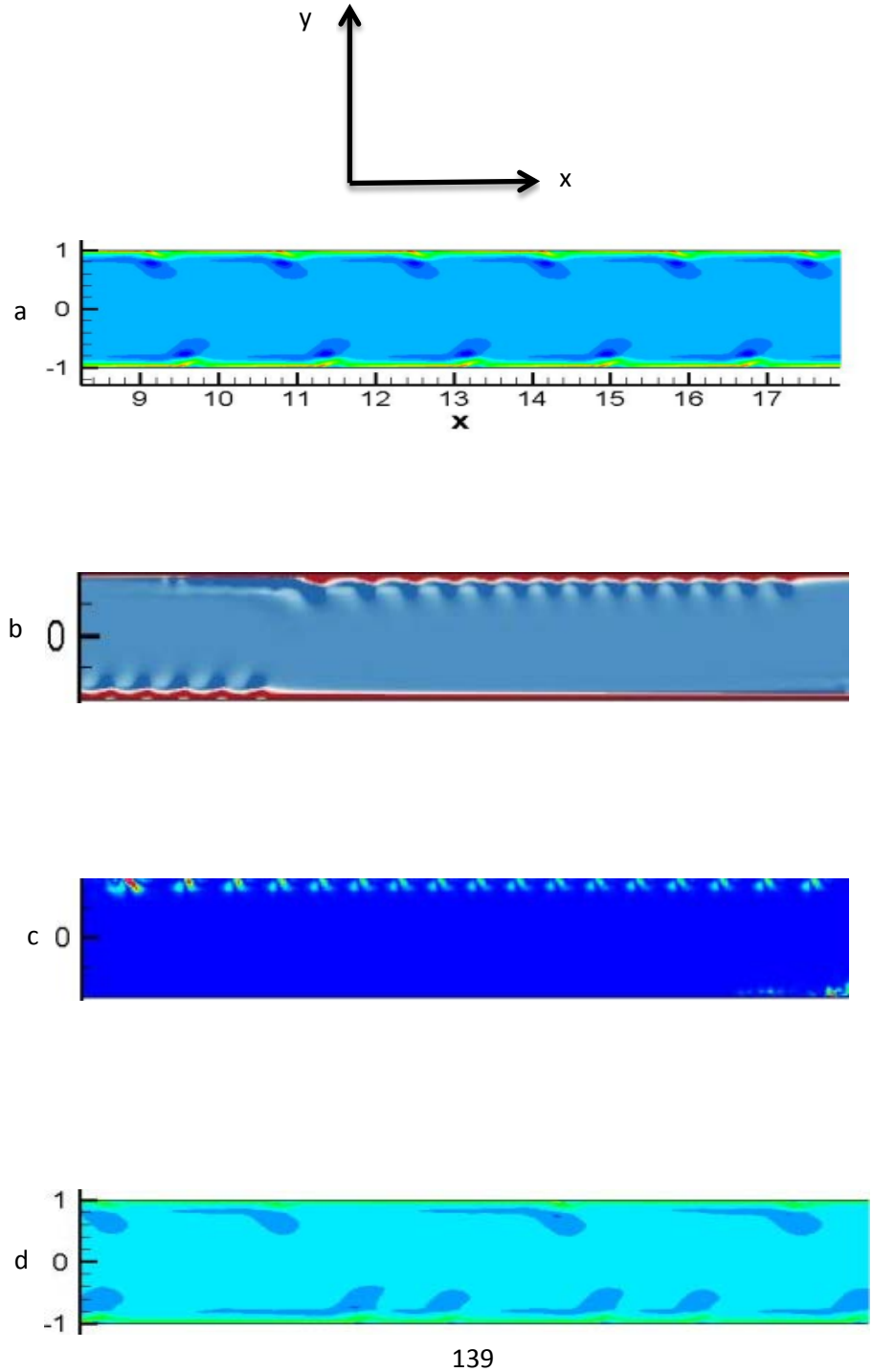

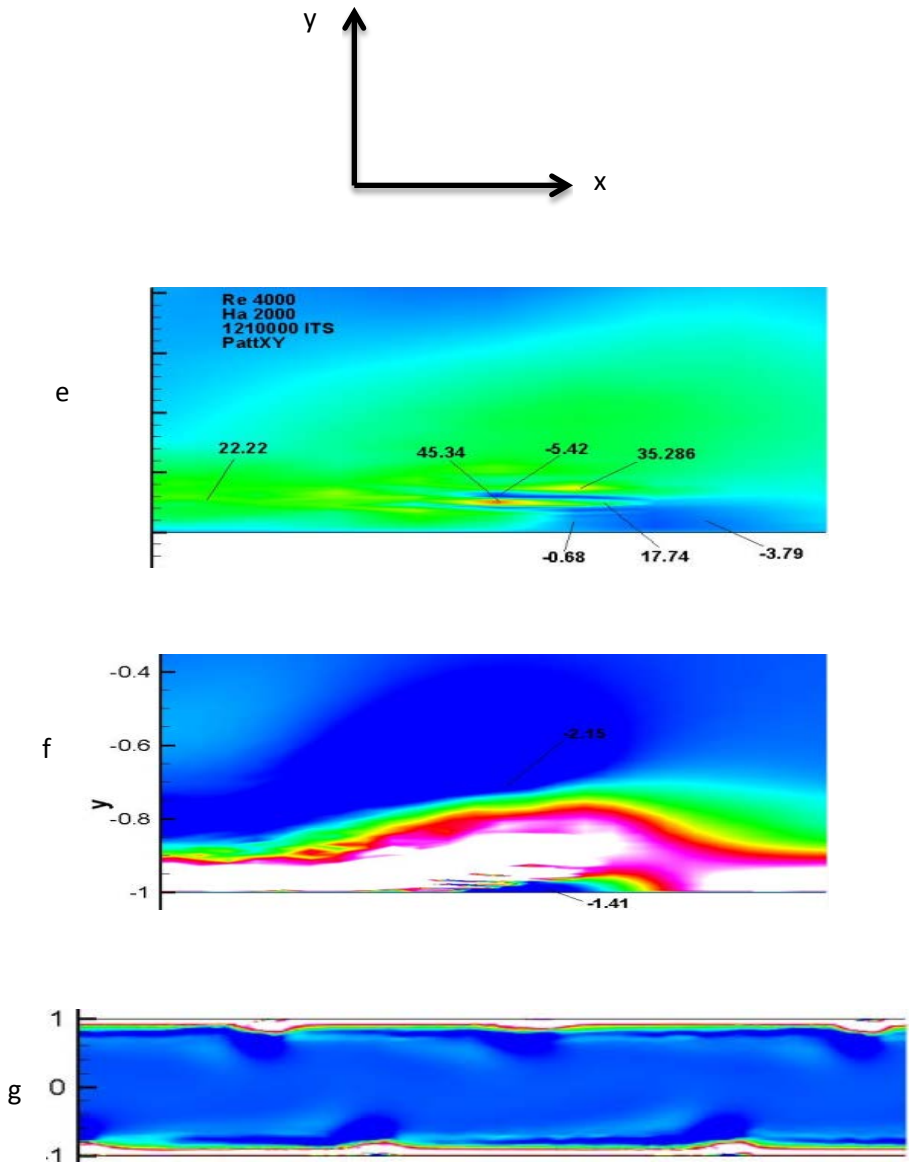

FIGURE 45. Full stream velocity U_x is demonstrated in the (*x*, *y*) mid-plane at *z* = 0 for a, b, d, e, f, g. Also c demonstrates q_t.Here (a) *Re* = 1,000, (b & c) *Re* = 3,000, (d, e & f) *Re* = 4,000 and (g) *Re* = 10,000, *Ha* = 2,000. Data displayed in (e) and (f) describes the pinpoint fluid velocities underneath and on top of the partial jet detachment.

5.3. Comparison

In order to gain a deeper understanding of the flow regimes described in sub-section 5.1 & 5.2, a direct comparison between the two different *Ha* values will now be presented. Comparative plots will be displayed, analysed and conclusions drawn.

We begin for the sake of continuity once more with the pressure gradient. Over the course of the investigation, as a whole, the effects of $\boldsymbol{J} \times \boldsymbol{B}$ have been seen to increase along with increasing *Ha*. Therefore one can consider the Lorentz force to be a major contributor to the pressure gradient in an MHD flow regime.. When the flow is relatively slow, i.e. at lower values of *Re*, the flow is dominated by the Lorentz force and there is a noticeably large pressure gradient in both *Ha* regimes, even more so at *Ha* = 2,000. As the flow velocity increases, the pressure gradient also begins to increase, demonstrating the increasing effects of inertia. The greatest difference in the pressure gradient observed is 188%, at *Ha* = 800, $500 \leq Re \leq 3{,}000$, for the same *Re* values but for *Ha* = 2,000 we have 177%, which coincides with the second transitional phase to turbulence, i.e. jet detachment. However, upon further investigation of the pressure gradients Figure 46 (a) can be somewhat misleading, as the difference between the pressure gradient of the two regimes is only 19% over the total investigation. To explain this further, over the entire *Ha* = 800 study, the pressure gradient increase from $500 \leq Re \leq 10{,}000$ is 394% and over the same *Re* range for *Ha* = 2,000 we have an increase of 378%. At the third transitional phase, were both regimes have reached a stage were fully turbulent side wall jets and an essentially laminar core are observed, the pressure gradient in both regimes has diminished in comparison to the second transitional phase. Also, as with the study in Chapter 4, the trend of the graph suggests that at greater *Re* values than studied here, the two comparative regimes would converge to the same point, i.e. zero, meaning that the importance of the Lorentz force diminishes. This again suggests that as the *Ha* and *Re* parameters increase, the MHD fluid regimes inside the duct would behave in the same manner as water.

Moving onto the KE comparisons within both flows, we will first examine the three separate components of KE as a function of *Re*, then consolidate to give a final more rounded picture. As KE results from the work done by a combination of pressure and shear forces, a reduction of which suggests a decrease in the magnetic energy due to the effect of the Lorentz force. Additionally, as stated in chapter 4, by studying this phenomenon, we are also able to determine the flows transitional phases into a turbulent regime, if there is indeed one.

Therefore beginning with q_x^2 at *Ha* = 2000, Figure 46 (b), we observe three transitional phases. The first phase occurs at the point at which partial jet detachment is found, between *Re* = 500 – 1000, here partial jet detachment resides in an almost periodic staggered formation at each side wall. As the fluid increases in velocity, the CCW vortices in the lee of the detachment eventually lift the jet away from the side wall to give full jet detachment. It should be noted that the CCW vortices do not move through the core of the flow. The dramatic increase in KE between *Re* = 1000 - 3000 is in direct comparison to the grouping together of fourteen smaller partial jet detachments. The grouping obviously displays much more KE and is the second transition phase to turbulence. At values *Re* = 3000 - 5000 the flow gradually moves into its third and final phase of transition were the Lorentz force is much stronger, almost laaminarizing the core of the flow and giving fully turbulent side wall jets. Subsequent to the regime at *Re* = 5000, the KE in the flow alters very little, but never the less, continues to drop. In direct comparison, *Ha* = 800, there is again three transitional phases which coincide with the visual flow development demonstrated in section 5.1, at *Re* = 500. At this *Re* value there is already partial jet detachment at the walls, previously seen in Figure 40 (f), but interestingly, as the regime moves into its second transitional phase, the KE drops as full detachment occurs and then begins to rise slightly, before moving into its final third transitional phase where we see an almost fully turbulent side wall jet regime. The KE comparison of the two q_x^2 regimes at *Re* = 3000 demonstrates a difference of 69%, thus suggesting a weaker Lorentz force and a much more turbulent regime at this *Re* parameter at *Ha* = 2000.The first transitional phases in both regimes demonstrate an increase in KE as the flows develop from partial jet detachment to full jet detachment. The second phase observes a drop in the KE in both regimes, especially within the *Ha* = 2000 regime as it drops to almost the same level as the initial transitional phase. Once both regimes have reached the point where they display fully turbulent side wall jets, the KE within the q_y^2 component continues to drop or remains essentially stable, through and into the third and final transitional phase. Interestingly, as both *Ha* regime hit *Re* = 10000 they basically demonstrate the same inherent KE, suggesting that the Lorentz force exerts the same effect on the flow irrelevant of *Ha*. Although at present this conclusion cannot be conclusively drawn without further study into other *Ha* values, it does show some evidence to this effect. The last and certainly not the least component studied, q_z^2, clearly demonstrates an increasingly anisotropic regime, especially at *Ha* = 2000, Figure 46 (d). It should be noted also that the q_z^2 component is the only component which increases throughout the entire high *Ha* investigation, further

demonstrating that the vortices within the regime become increasingly anisotropic as the *Re* values are increased.

Now that we have examined the three separate components of KE and the way in which they determine the transitional phases of the higher *Ha* flow regimes, we are now able to combine all three to components to demonstrate the full scale KE across the entire duct domain within the two separate *Ha* regimes Figure 47. As is clearly seen, the full scale KE is at it's highest at the lower values of *Re*, which coincides with the point in which we have a transition from partial to full jet detachment. Both regimes exhibit a reduction in energy as *Re* = 2,000 is approached. Within the *Ha* = 800 regime the KE continues to decrease gradually, the same however cannot be said for *Ha* = 2,000. At the second transition phase, *Re* = 2,000, there is a sharp increase in KE again, which continues to rise until *Re* = 4,000 is reached, the regime subsequently then decreases monotonically to its lowest value at *Re* = 10,000. This is not surprising, due to the fact that at *Re* = 10,000, a turbulent flow regime is observed within the side wall jet region. The decrease of KE is clearly the result of the growing importance of the Reynolds stresses as *Re* values increase in addition to the Lorentz force. The full scale KE plot clearly demonstrates that this latter phenomenon clearly damps out turbulent fluctuations in both regimes.

a

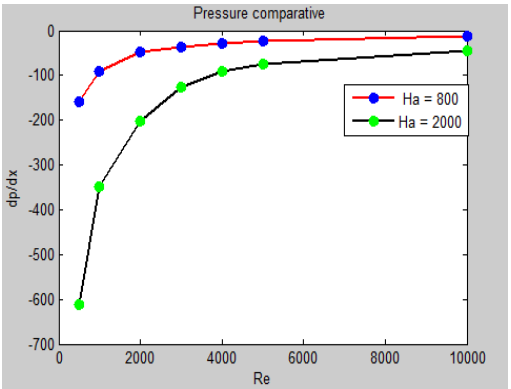

b

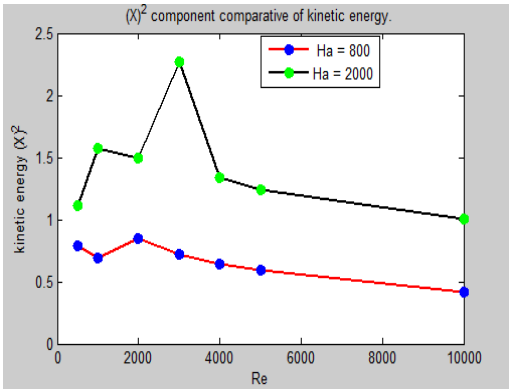

c

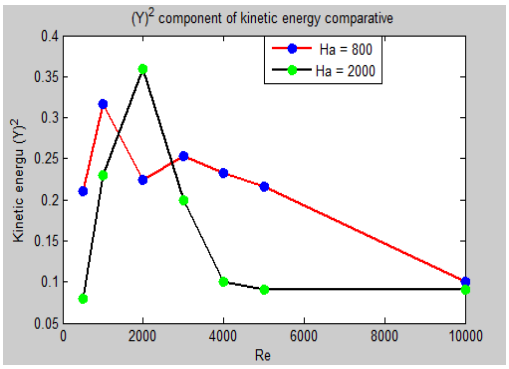

d

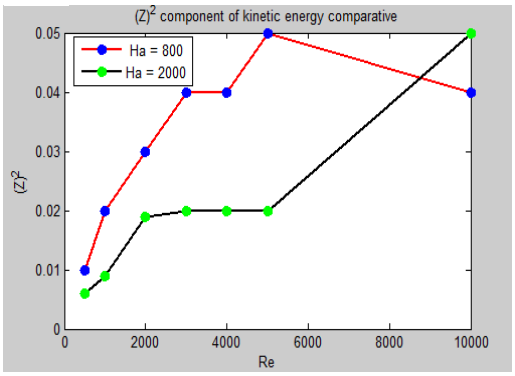

FIGURE 46. Here we demonstrate the comparative graphs at *Ha* = 800 & 2,000 as a function of *Re* for (a) $\frac{\partial \mathrm{p}}{\partial \mathrm{x}}$ and three components of KE (b) q_x^2, (c) q_y^2 and (d) q_z^2.

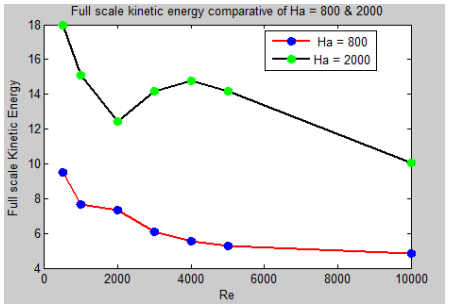

FIGURE 47. Full scale KE comparison for *Ha* = 800 & 2000 as a function of *Re*.

This next step forward, now that the KE study was complete, is to determine whether there is indeed a difference in the velocity profiles of the two *Ha* values at *Re* = 500 and *Re* = 5000. As is evident from Figure 48 (a - b), the jets are much more pronounced along the side walls of the duct at *Ha* = 2,000 within both *Re* values investigated in u_x. In addition to this, there is a much stronger reversed flow for *Ha* = 2,000 at the lower *Re* parameter, i.e. *Re* = 500, Figure 48 (a). This demonstrates that the CCW vortices, which are housed within this region, have a stronger effect on the flow regime, which has been observed when jets partially detach. As the regime is increased to *Re* = 2000 two opposite effects occur: the jets decrease in both u_x

& u_y, the jets at *Ha* = 800 increase in the u_y and decrease in the u_x. Demonstrating increased thickness in the side wall jets, which further suggests increased instabilities housed within, hence their increased width. The velocity jet at *Ha* = 2,000 however have become increasingly thinner, displaying slight turbulence within their region. Both Figure 48 (a - b) demonstrate the differing effects that the Lorentz force and inertia has on the different flow regimes.

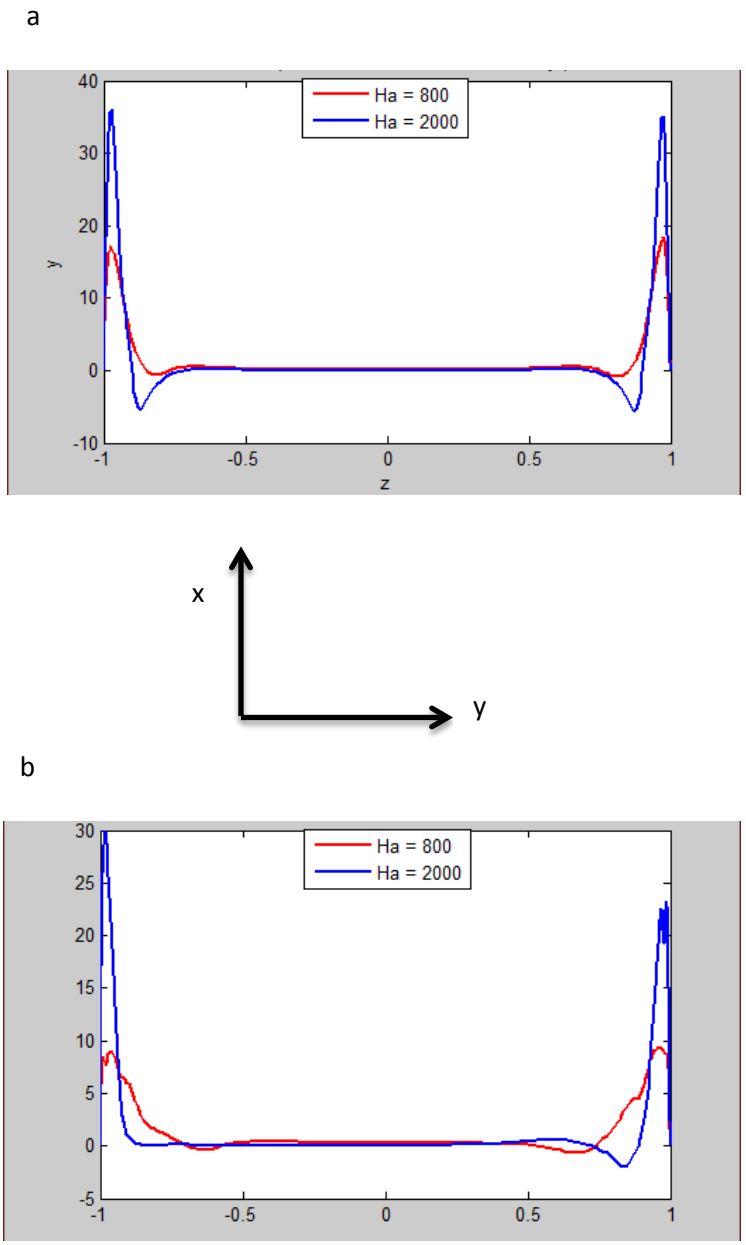

FIGURE 48. Mid plane cut at *z* = 0 of u_x velocity component for (a) *Re* = 500 and (b) *Re* = 5000. *Ha* = 800 (red), *Ha* = 2,000 (blue).

Summary

Large nuclear fusion reactors operate within very hostile environments, where intense magnetic fields can operate in excess of eight Tesla. Therefore it is of paramount importance that flow simulations mirror, as much as possible, these harsh environments in order for liquid metal blankets to be realized as real contenders for the proposed cooling system of a fusion reactor. Contained within this chapter there has been an investigation into the flow of fluid travelling through a duct at high *Ha* values, one of which is close to the magnetic field strength observed in fusion reactor environments. At higher values of *Ha*, it is quite evident that the flow regimes differ to that observed at lower *Ha* parameters. This is to be expected, as the increase in *Ha* brings with it an increase in the MHD interactions within the regimes, i.e. $\boldsymbol{J} \times \boldsymbol{B}$. It is interesting however to observe the increased effect that the Lorentz force has on the regimes, dominating large areas of the flow from the core out towards the side walls. The increased Lorentz force damps extended areas of turbulent flow within the duct thus exhibiting an essentially laminar core. The first evidence of this is the stretched appearance the TW vortices. Thinner side wall jets have been observed as *Ha* is increased along with a more intense reverse flow near the outer region of the high velocity jet. An additionally interesting difference between the high and low *Ha* values is the way in which jet detachment occurs. At lower values of *Ha*, the CCW vortices housed at the outer region of the jet, move through the core of the flow regime, thus resulting in a turbulent core. At higher values of *Ha* however, the CCW vortices are still responsible for slowing the jet down and lifting it away from the side walls, but transitional movement of the CCW vortices is not observed in either regime, tending to stay closer to the side walls. We can postulate that this scenario can only be determined by the strong MHD effects inherent at higher *Ha* values. However, this is yet to be confirmed and requires a much more in depth analysis as to the extent in which the Lorentz force has on a Hunt's flow regime. Due to the fact that the core of the flow is subjected to an almost full laminarzation, heat and mass transfer at these high *Ha* parameters would be extremely limited.

Equally interesting is the behaviour of the pressure gradient at these high parameters. Initially, there is quiet a substantial decrease in the pressure gradient across the entire domain at the beginning of both *Ha* regimes, but as *Re* is progressively increased to *Re* = 10,000, the pressure reduces and tends towards zero, although this assumption is un-validated at the present moment as higher *Re* values need to be studied at these fixed *Ha* parameters. What is

most interesting about this phenomenon is that we have seen strong Lorentz force effects damping out turbulent fluctuations within larger areas of the core. The combined MHD effects, inherent of higher *Re* and *Ha* values, In addition to the decreasing pressure gradient observed in both systems leads to the assumption that the KE in both flow regimes, within the context of these parameters investigated, behave very similar to a flow which is hydrodynamic and non-conducting, similar to water, This suggestion is quiet contradictory as a hydrodynamic flow at these *Re* values is well known to be fully turbulent But at present these are purely assumptions and the clarification of such requires much further investigation.

6. Low Hartmann, *Ha* = 10.

It is well defined that in purely hydrodynamic laminar flow regime between solid walls, the velocity profile is parabolic for low values of *Re* Figure 49 (a). Additionally, as *Re* progressively increases in a purely hydrodynamic flow, we could expect to observe an increasingly turbulent flow regime Figure 49 (b). However, if an electrically conducting fluid traverses through the same solid walls, subjected to an externally applied magnetic field, the effects of the Lorentz force, specified by the component of the electrical current perpendicular to the magnetic field: $\boldsymbol{f_L} = \boldsymbol{J} \times \boldsymbol{B}$ alters the appearance of the flow in the duct. The altercation arises as the momentum balance is established between the pressure gradient and $\boldsymbol{J} \times \boldsymbol{B}$, exhibiting a velocity profile commonly referred to as the M-profile. Briefly, we remind ourselves that at lower values of *Ha*, viscous forces dominate electromagnetic forces. Naturally then, at this low *Ha* value used within this chapter, we would expect to observe a flow where the effects of the Lorentz force would be minimal. The question therefore one would ask is "*At what point, if any, would one expect to see a turbulent flow within a Hunt's flow regime at such a low Ha value ?*". The remainder of this Chapter will attempt to answer this question by giving a progressive, visual in depth representation of Hunt's flow as *Ha* is fixed at $Ha = 10$ and *Re* increases in value $100 \leq Re \leq 20{,}000$. Initial conditions and methodologies mirror those set out in previous Chapters 4 & 5.

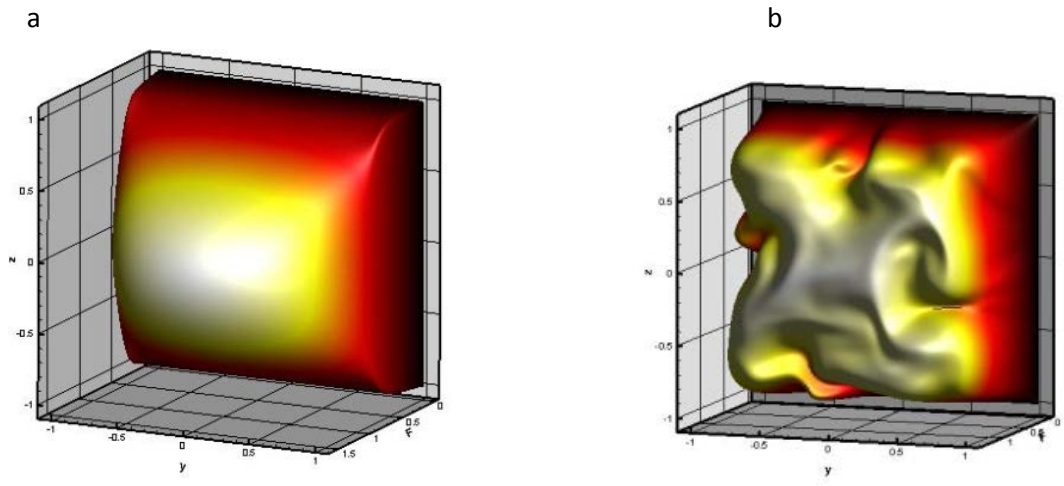

FIGURE 49. Instantaneous velocity profiles of a hydrodynamic flow in the *x*-direction. (a) *Ha* = 0, Re = 1,000, (b) *Ha* = 0, *Re* = 2,000.

Therefore, if we begin our investigation at the lowest value of *Re* studied in this Chapter, i.e. $Re = 100$, we immediately observe TW vortices present again at the side walls. With other values of *Ha* studied within the context of this research, it has been demonstrated that as the flow temporally evolves the TW vortices disappear to be replaced with new forms of instabilities. Now however, at *Ha* = 10, this is not the case. The TW vortices instead of disappearing to be replaced, they do not disappear instead they temporally evolve, loosing their columnar appearance. Their inherent KE also develops in magnitude and distributes itself throughout the entire domain. By continuing along the vein of temporal evolution, the presence of the Lorentz force, although being much weaker at this *Ha* parameter, begins to exert its effects throughout the core of the flow. Gradually, the Lorentz force damps out the fluctuating KE, leaving a fully laminar state Figure 50 (a – c). As we progress through to higher *Re* numbers, we discover that this described flow pattern at $Ha = 10$ is a common occurrence at the beginning of all simulations at these *Ha* and *Re* values, even at $Re = 1{,}000$.

Based on the fact that we are observing a conducting fluid subjected to an external magnetic field, the velocity profile which one would predict would be a laminar, M-shaped profile, predictably it is exactly this which is observed, Figure 50 (a). The flows velocity profile however maybe misleading, because if we compare the velocity profile of $Ha = 10$ against the velocity profiles of $Ha = 100 \,\&\, 2{,}000$, we gain a true perspective of the effects that $\boldsymbol{J} \times \boldsymbol{B}$ has on the differing regimes Figure 51 (a). As is apparent, the effect of the Lorentz force on a low *Ha* value within the context of this study is minimal. Moreover, the Lorentz force temporally evolves the flow into the characteristic M-profile over a longer period of time compared to higher *Ha* values. At high *Ha* values, the M-shaped velocity profile is instantaneous at the initial point of all simulations within this study, here however at $Ha = 10$, it is not. The effects of the Lorentz force gradually spreads out from within the core of the domain, temporally evolving out towards the side wall in the *y*-direction. This gradual effect Lorentz force can be observed through to $Re = 10{,}000$. At $Re = 20{,}000$, the effects of $\boldsymbol{J} \times \boldsymbol{B}$ have very little effect on the flow and only weak velocity jets are observed at this high *Re* parameter Figure 52.

Throughout this investigation so far, the transitional phases to a fully turbulent regime within Hunt's flow has been the main focus of study. Now however, we will investigate laminar Hunt's flow, or to be more precise, the transitional phase from initial conditions to a laminar, homogeneous regime. The reason for this alternative is that at these low *Ha* values, most if

not all flow regimes, within the context of this chapter, demonstrate a temporally evolving laminar flow. Instabilities throughout the domain occur at the beginning of the simulations, the Lorentz force and viscous forces, thus tend to damp out turbulence as the flow is allowed to develop. Therefore the most interesting phenomena in the developing regime is whilst under this transitional period. Therefore, flow regimes under the widely regarded threshold for non-MHD turbulent regimes, i.e. $Re = 1{,}200$ will now be studied further. It must be stressed at this point that all previous and subsequent flow investigations within this chapter are at a fixed $Ha = 10$.

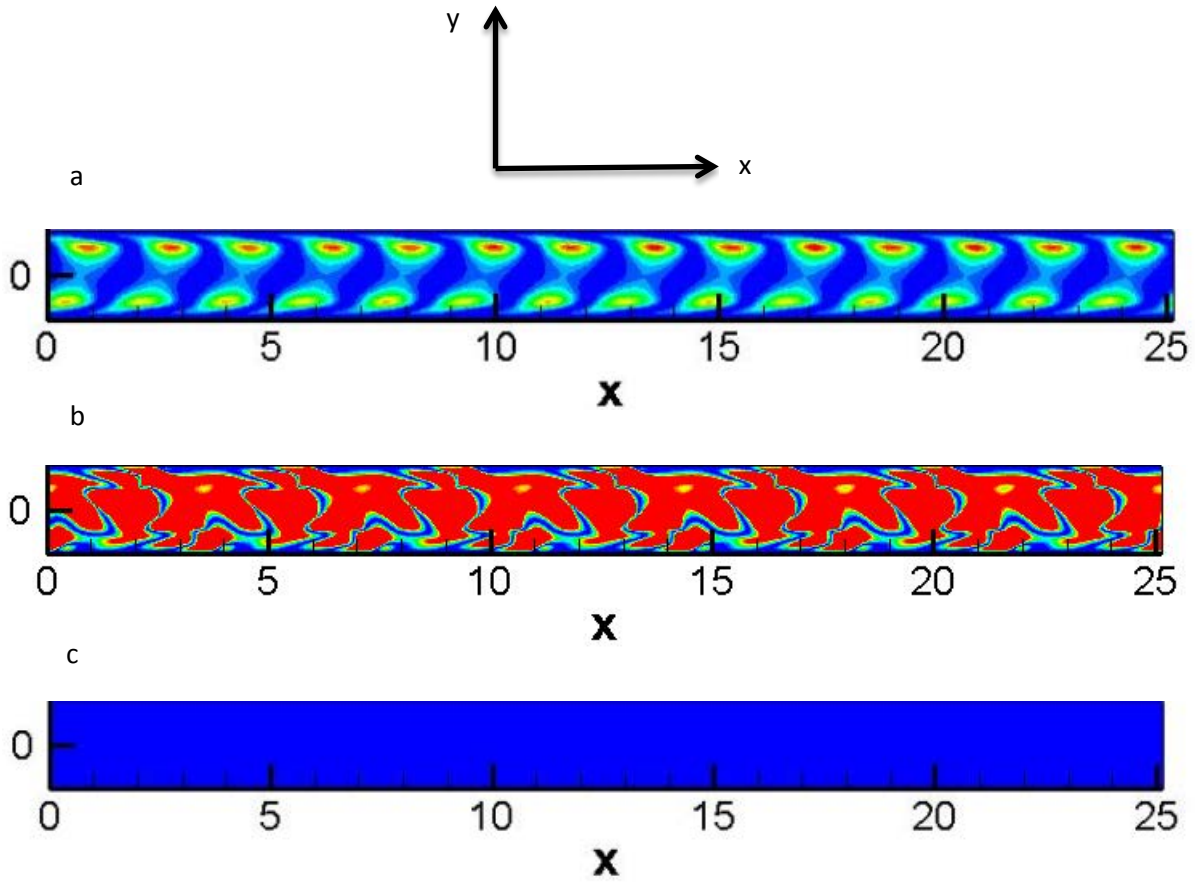

FIGURE 50. Mid-plane cut at z = 0 of the temporal damping of $q_t = u_x^2 + u_y^2 + u_z^2$. (a) Demonstrates the presence of TW vortices (b) exhibits the temporal evolution of q_t and (c) shows the laminarization of the flow at the end of the simulation.

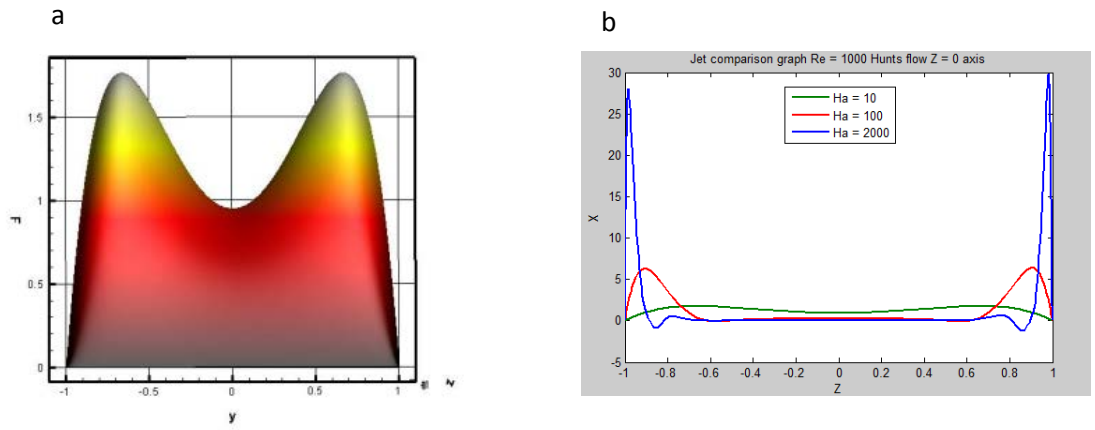

FIGURE 51. (a) represents a typically 3-D predicted instantaneous velocity profile at *Ha* = 10, *Re* = 100. Within (b) we see the 2-D mid-plane cuts at *x* = 0 (left) *z* = 0 (right) for the comparative of *Ha* = 10, 100 & 2,000.

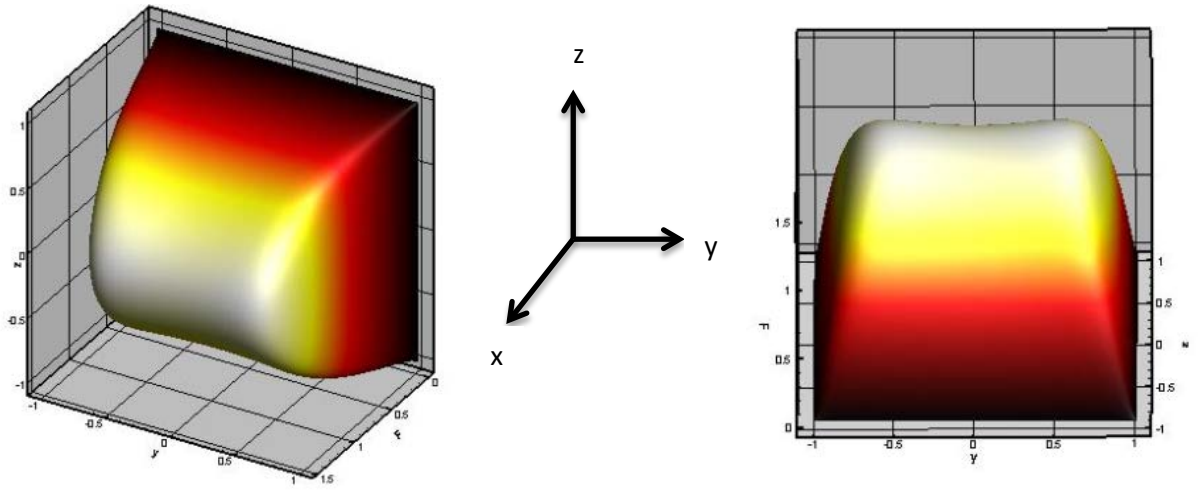

FIGURE 52. 3-D instantaneous velocity representation of the weak effects that $\boldsymbol{f_L = J \times B}$ has on a flow regime at *Ha* = 10, *Re* = 20,000.

The description of the subsequent flow regimes will now range from $100 \leq Re \leq 1000$. Under such low parameters, the investigation will demonstrate interesting flow patterns at the early stages of temporal development before the effect of $\boldsymbol{J \times B}$ completely laminarizes the flow. By commencing the study at $Re = 100$, the KE contained within the TW vortices is initially localized, mirroring what is found at higher *Ha* and *Re* numbers within this investigation. After approximately 30 CTU, the KE begins to spread throughout the entire flow domain and continues to do so for a further 15 CTU. As the flow temporally evolves the

opposing Lorentz force rapidly supresses the KE fluctuations in the core of the flow, leaving an essentially laminar, homogeneous regime in u_x. Interestingly, although the regime is classified as laminar, clearly there are instabilities within the flow. This can be confirmed by almost periodic patches of, in comparison to the core, high areas of KE close to the side walls, suggesting that the instabilities are small vortical structure. By focusing in on the small areas of KE, it has been observed that they contain small paired vortices rotating around each other in a CW motion Stages of this evolution can be observed in Figure 53 (a – c). It worth noting at this point, that the range of the fluctuating KE values at this particular *Re* is very low, i.e. $0.02 * 10^{-15} - 0.03 * 10^{-16}$. Residing between the core and the outer region of the jet, a band of fluid is observed in approximately the same region in which the band of CCW vortices are witnessed at higher *Ha* values. The slower velocity band however does not contain any CCW vortices at this point and thus no reversed fluid flow is observed travelling in the *x*-direction. Interestingly, in comparison to the entire domain, inclusive of the velocity jets and core, the band produces the slowest fluid flow in the entire region, only slightly perturbing the fluid within the outer jet in the *y* & *z*-direction. It must be stressed that the fluctuations are very weak at this stage, but nevertheless, if we directly compare the velocity of the fluid within the jet at the beginning of the regime, to its velocity once the flow has laminarized, we can obviously see the combined effects of the Lorentz force and the slower band of fluid. The velocity range of the jet therefore is 4.65 – 1.84 units. In fact, this type of temporal flow development is also observed at $Re = 200$. As the first two *Re* numbers studied are quite low in value, there is no evidence of reversed flow near the outer region side wall jets. Therefore one can be confident in stating that within the context of a Hunt's flow regime, velocity jets are being constructed purely through the effects of the Lorentz force spreading through the fluid in the span-wise *y*-direction.

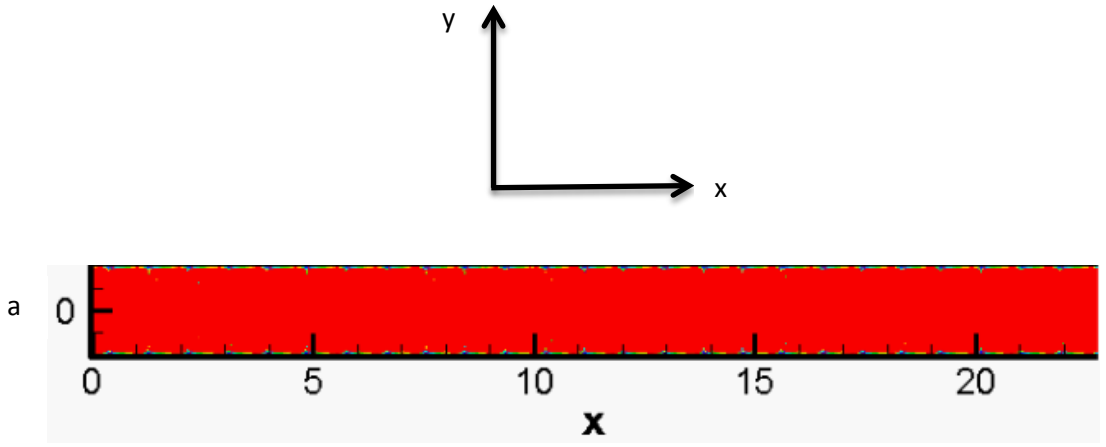

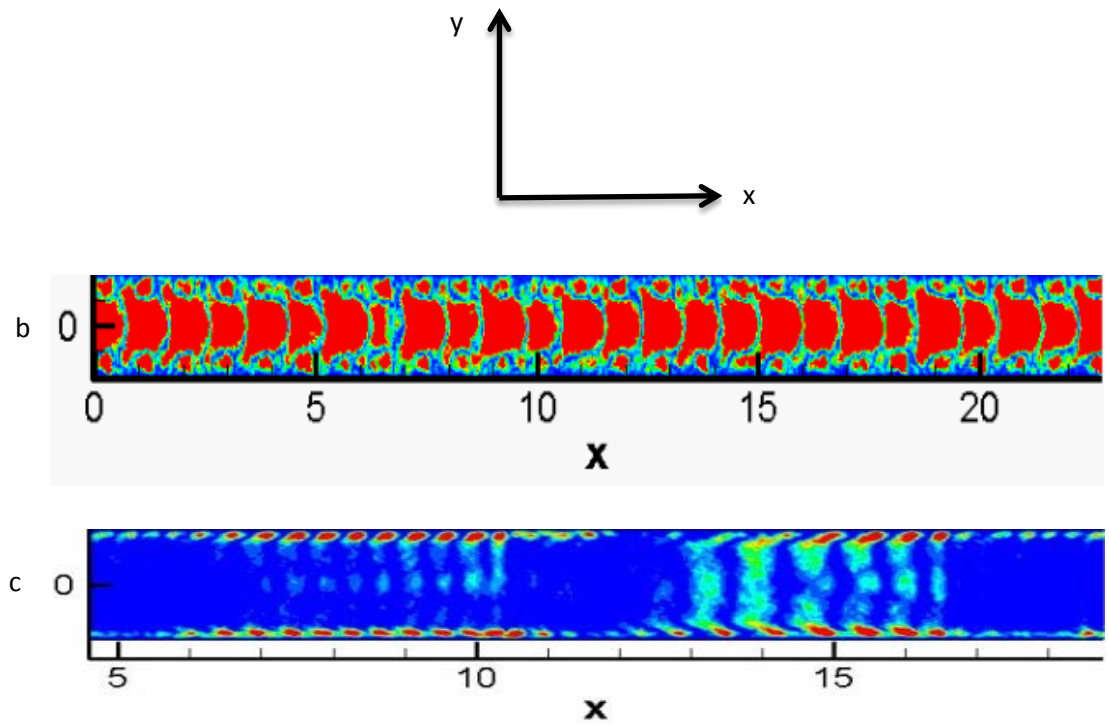

FIGURE 53. (Top to bottom) Here we demonstrate the damping effects that $\boldsymbol{f_L} = \boldsymbol{J} \times \boldsymbol{B}$ has on $q_t = u_y^2 + u_z^2$ at Ha = 10, Re = 100. The bottom image (c), shows that the greatest development of $q_t = u_y^2 + u_z^2$ is close to the side walls, housed within the jets.

By increasing to $Re = 400$, there is a defined transitional period within the flow regime as the Lorentz force begins to have a greater effect on the flow. The KE within the flow again dominates the initial regime, but then temporally dissipates, leaving a homogeneous, laminar flow. The range of KE contained within is still very small, but in comparison to the KE at $Re = 100$ & 200, there has been quiet a large increase, i.e. $9.5 * 10^{-6} - 5 * 10^{-7}$, especially within u_x. Again, a band of slower moving fluid can be clearly defined within the outer region of the jet. The temporal evolution of the flow at $Re = 400$, results in the slower band of fluid losing its familiar laminar appearance, lifting the outer region of the jet in the y – direction. The slower band of fluid not only influences the outer jet, but effects the jet in its entirety, having a negative effect on it's over all velocity. This transitional period completely alters the flow regime and creates a regime which resembles a type of Kelvin-Helmholtz instability, Figure 54 (a – c). As the flow temporally evolves further, the Lorentz force damps

out the velocity fluctuations and reverts the flow back to a laminar regime after approximately 20 CTU .

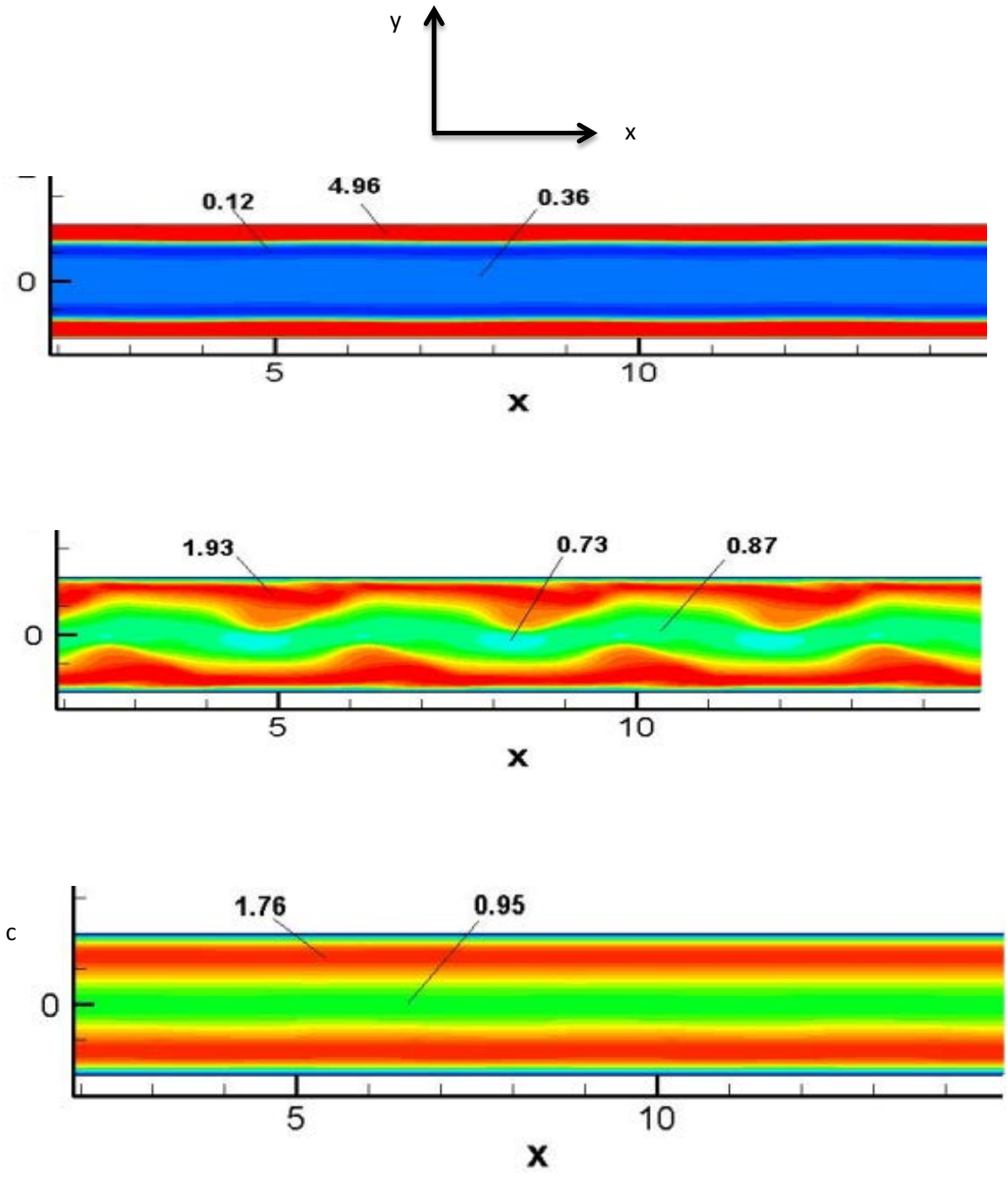

FIGURE 54. Full stream-wise velocity u_x in the (x, y) mid-plane at z = 0 for *Ha* = 10, *Re* = 400. The turbulent transitional period is demonstrated, from and initially laminar state (a) through to the transition to turbulence (b), through to laminar flow once more (c). Flow is from left to right. Data points are displayed of fluid velocities within the flow.

Progressing to $Re = 800\ \&\ 1{,}000$, the short transitional phases from laminar, to turbulent, through to laminar again become increasingly interesting. To aid in the elimination of continuous repetition, both of these higher *Re* numbers will be studied in unison. The reason for this approach is that the flow regime at $Re = 800$ is similar in appearance and behaviour to that at $Re = 1{,}000$. The range of KE contained within $Re = 800, is \quad 8 * 10^{-25} - 5 * 10^{-26}$, the velocity of the fluid within the jets at the beginning of the simulation, i.e. 1 – 10 CTU is 5.75 units. The concluding jet velocity, once the regime has been subjected to the transitional phases, i.e. 50 – 100 CTU is 1.76 units; At $Re = 1{,}000$, $1.2 * 10^{-19} - 1 * 10^{-20}$, initial jet velocity 5.92 units, i.e. 1 – 10 CTU, concluding jet velocity, i.e. 50 – 100 CTU is 1.75 units. As is evident, the initial and concluding jet velocities from both *Re* regimes are essentially equivalent. Therefore, this suggests that a temporally evolving flow regime at these *Re* parameters are essentially identical and that the Lorentz force has the same final effect for both regimes. But the transitional stage of both regimes produces the most interesting phenomenon.

The transitional phases at $Re = 1000$ can be demonstrated in four phases Figure 55 (a –d). The regime immediately demonstrates the initial effects an opposing Lorentz force has on the flow, displaying velocity jets (red) and a reduced velocity core (light blue). Although the effects can clearly be seen, the flow is deemed to be laminar Figure 55 (a). In addition to the velocity jets, a band of slower moving fluid in the outer region of the jet (dark blue) is also clearly defined. Here we observe the flow before its first transitional phase at approximately 1 – 10 CTU. As the regime temporally evolves, i.e. 10 – 30 CTU, we see a first transitional phase. The band of slower moving fluid located at the outer region of the jet begins to have an increasing effect, slowing the fluid contained within the jet, thus lifting it in the *y* – direction and altering the flow into a turbulent regime Figure 55 (b). In doing so, both the jets and the slower fluid lose their characteristic elongated profile and becoming increasingly more localized into smaller turbulent regions. The now fully turbulent jets stretch in the *y* – direction, thus producing a turbulent core with isolated areas of slower and faster CW rotating vortices, similar to the process in which one observes a Kelvin – Helmholtz instability. The visual process upon first inspection is very similar to the mechanism in which the CCW vortices lift the side wall jets described in Chapter 4, but here there are no

CCW vortices, this suggests that the slower band of fluid is singularly responsible for the first transitional phase in this particular flow development. Progressing further into the temporal evolution of the flow, i.e. 30 – 60 CTU, it can clearly be seen that the regime is fully turbulent Figure 55 (c). There are distinct, isolated areas of reduced KE in an almost periodic, staggered formation located at the side walls, but also moving through the core. The final transitional phase, i.e. 60 – 500 CTU is a return to a laminar regime once more Figure 55 (d). The Lorentz force progressively damps out all turbulent fluctuations within the flow and the jets eventually merge once more, becoming the more familiar single entity at each side wall, thus reverting the regime back to a homogeneous, laminar flow state. At this stage all fluctuations have been damped out by the Lorentz force. It should be noted that the effect of the Lorentz force are weak in comparison to the flow regimes described in Chapters 4 and 5 and as a result the velocity jets are much wider in the both the *y* and *z* – directions, Figure 56 (a) and (b).

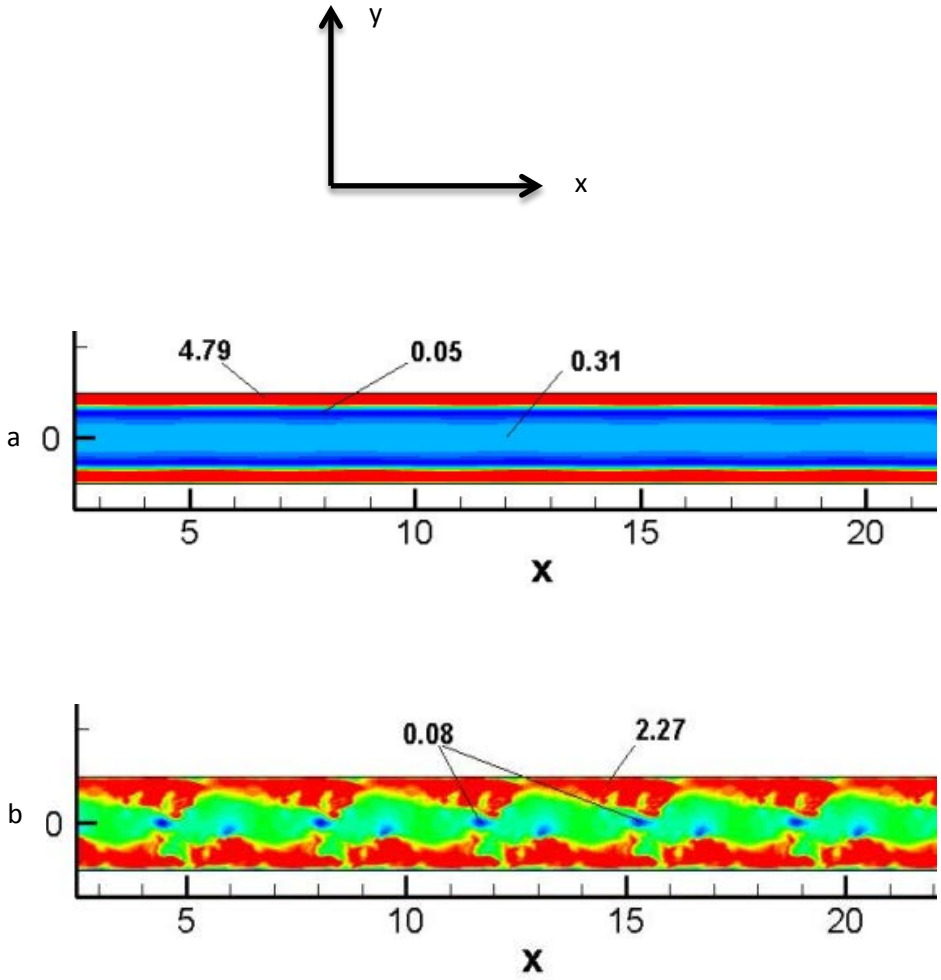

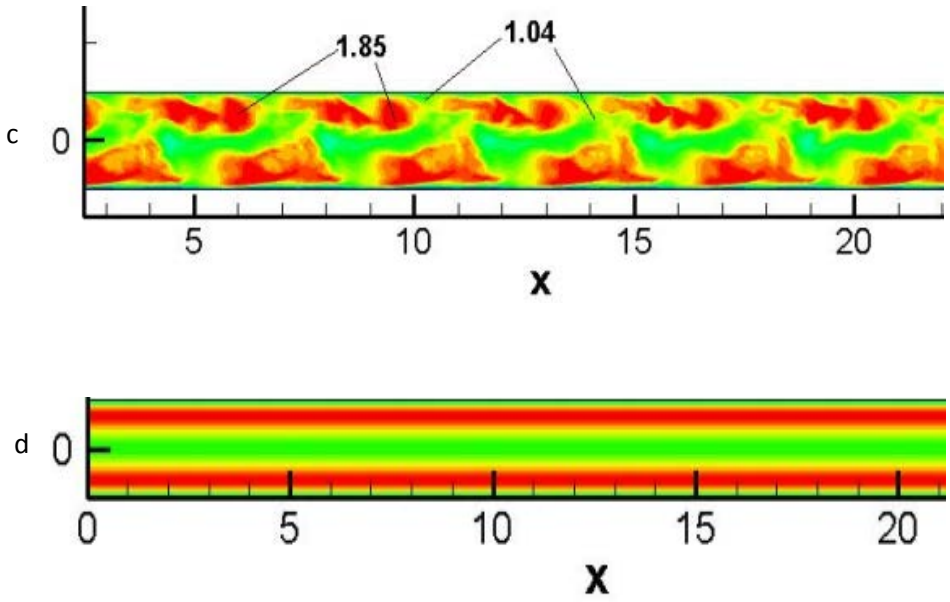

FIGURE 55. Full stream-wise velocity u_x in the (*x*, *y*) mid-plane, at *z* = 0 for *Ha* = 10, *Re* = 1000. (a), (b) and (c) show pin point fluid velocity within the flow.

At high values of *Re*, i.e. 10,000 & 20,000 the initial same transient process can be seen as in the lower values of *Re* throughout this chapter. At *Re* = 10,000 the velocity of the fluid has greatly increased, but nevertheless the flow regime still demonstrates very weak damping Lorentz force effects, Figure 56 (a - b). At *Re* = 20,000 Figure 56 (c - d), the highest *Re* value studied.. The fact that the velocity profile exhibits very weak to no side wall velocity jets is a surprising result. The MHD effects on the flow regime at this *Re* parameter, i.e. high fluid velocity are negligible.

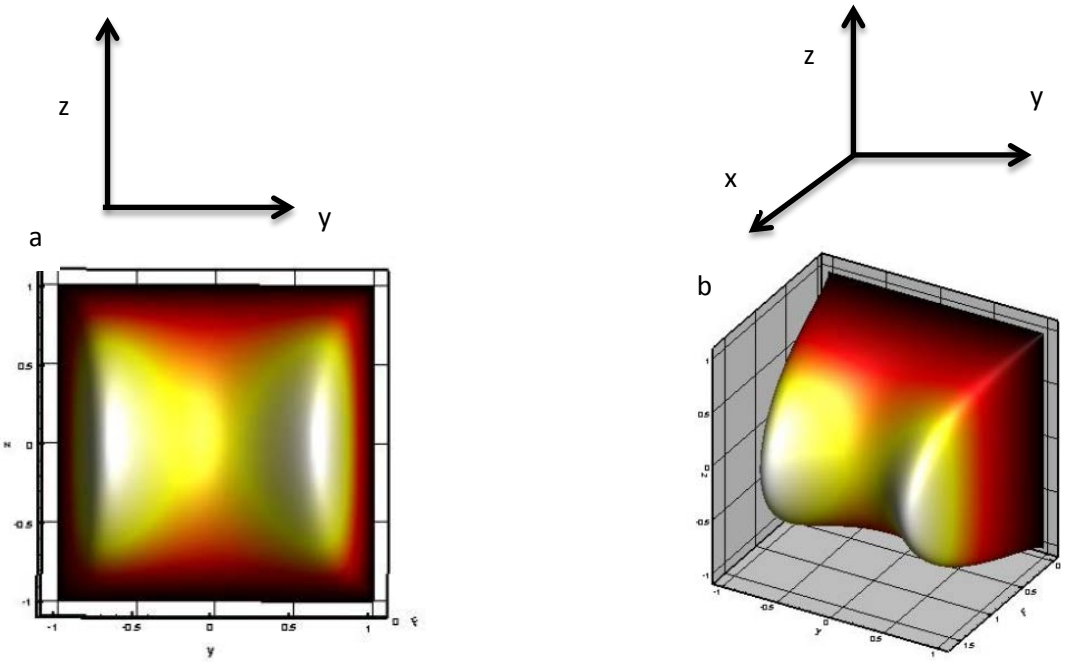

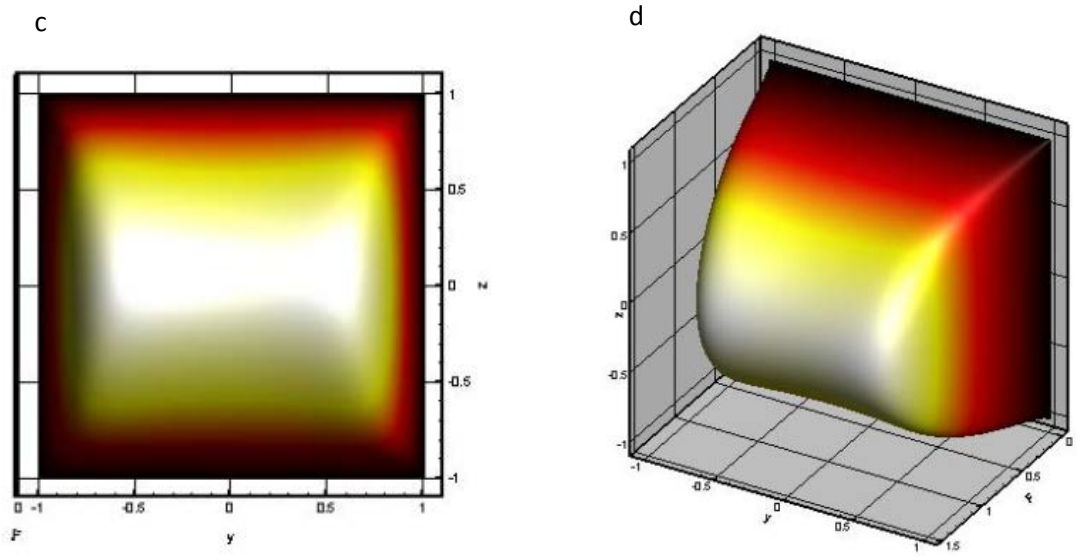

FIGURE 56. Instantaneous velocity profiles of Hunt's flow in the *x*-stream wise direction at *Ha* = 10, *Re* = 10,000 (a) & (b), in addition too *Re* = 20,000 (c) & (d).

Summary

Here we have investigated an electrically conducting fluid subjected to a relatively low applied external magnetic field. The values employed for this particular smaller investigation were $Ha = 10$, and $100 \leq Re \leq 20{,}000$. By taking the entire investigation as a whole, the Lorentz force administers a weak effect on the fluid as demonstrated in the cross sectional velocity comparison with higher *Ha* values. Nevertheless, the effects of the Lorentz force are strong enough to alter the velocity profile of every *Re* number studied until *Re* = 20,000 is reached. The question posed at the beginning of this chapter was: *"At what point, if any, would one expect to see a fully turbulent flow within a Hunt's flow regime at such a low Ha value ?"*. Having now conducted the investigation in its entirety, it can be stated with full confidence that a fully turbulent flow regime at such a low *Ha* value occurs at the first transition to turbulence phase, approximately, i.e. 10 – 40 CTU for $Re \leq 10000$. Once the regime has reached this temporal phase, it persists for approximately 30 – 60 CTU, which can be deemed as quiet a short transitional period. After 60 CTU, the Lorentz force completely damps out all turbulent fluctuations in the flow, reverting it back to an essentially laminar state. Throughout the small additional study, velocity jets have been present for all flow regimes up to and including $Re = 10000$. Due to weaker effect of the Lorentz force at this

Ha value, the velocity jets are much thick in both the *y* and *z* – directions and not as pronounced in the *x* – direction, in comparison to higher values of *Ha*. When the regime is increasing to *Re* = 20000, the Lorentz force has very little effect on the flow regime and essentially the characteristic velocity jets diminish leaving an almost parabolic flow profile, closely resembling that of a hydrodynamic profile. A linear stability analysis on Hunt's flow was previously studied at a low *Ha* value [103] which uncovered a wide variety of perturbations, including streaks spreading out from the core towards the duct wall in the *y*-direction. Having established the behaviour of Hunt's flow at even lower values of *Ha*, it would be interesting to conduct a linear stability analysis as an additional investigation to determine whether the unstable modes stipulated in [103] are similarly observed at *Ha* = 10. This can be viewed as further work.

7. Conclusions and outlook.

The present investigation was concerned with the transition to turbulence in a particular duct configuration known as Hunt's flow, which has very strong side wall jets. Low, moderate and high magnetic fields were considered. The purpose of this study was to understand what happens to the side wall jets as the Reynolds number, which characterizes the fluid, is varied. For moderate magnetic fields with *Ha* = 100 - 200 the transition was found to involve a number of instabilities and various on-linear effects as the Reynolds number was increased. First, at low values of *Re* the familiar Ting-Walker vortices were reproduced in the side-wall jets. These vortices have the characteristic length scale of the Shercliff layer $O(Ha^{-1/2})$. It is important to note that these vortices are weak and thus have a negligible effect on the mixing of the flow. It was demonstrated in this study that when *Re* was increased, these small Ting-Walker vortices completely disappear, being replaced by new much more energetic, larger and thicker vortices which occupy almost all of the duct cross-section. This phenomenon has not been observed in any prior study. Increasing *Re* leads to the emergence of new, more energetic vortical structures, "pike-teeth", which are aligned with the field, and serve as the seeds to another phenomenon, jet detachments. The jet detachments from the sidewalls are important as they lead to intensive fluid mixing at lower *Ha* values. Jet detachment is not a new phenomenon, but as to what causes it was unknown until this investigation. It was found in this study that jet detachments occurs due to large-scale counter rotating vortices which appear in the outer region of the jets and lift the higher velocity fluid contained within the jets away from the side wall. This process was extensively investigated and explained in chapter 4.

The detachments at the two sidewalls are not independent: but rather coupled by the counter rotating vortices from one jet travelling through the core of the flow and causing a respective jet detachment at the opposite wall. But this is only observed at the lower end of the *Ha* parameters used within this study. As *Re* is increased, an additional new phenomenon appears, detachments becomes more irregularly and frequent, leading to multiple jet detachments at the side walls. Intuitively, one would expect that the higher the fluids velocity the more turbulent the flow becomes. However, this is not the case found in this study, as a yet further increase in *Re* leads to a previously unseen flow regime with a nearly laminar core, populated by very weak quasi-two-dimensional vortices and fully turbulent jets. In this

flow regime only the fluid near-wall is mixing. Another new result found in this study were multiple flow states that can exist for the same values of *Re* and *Ha* depending upon initial conditions. An intensive investigation into hysteresis-like phenomenon has been performed by first gradually increasing *Re* to a certain value and then reducing it back to its initial value. For moderate values of *Re* the flow was found to return to a state different from the initial one that existed at the same *Re* value: namely, instead of the original Ting Walkers vortices, jet detachment was found for a different *Re* number

Finally, at high values of *Ha* the scenario of transition to turbulence was found to be similar to that summarised above, but with some essential differences. First of all, the much stronger Lorentz force leads to a more laminar core with thinner jets. Secondly, the jet detachments that now occur at higher *Re* are smaller in size and occur more frequent. Next, the large-scale vortices that lead to jet detachments in a moderate magnetic field, are now smaller in size and are now most probably related to the reversed flow at the outer edge of the jets. This issue requires an additional investigation.

Concerning the outlook and the scope for future work, there are several issues that need to be studied. First of all, the dependence of the flow on the initial state is very important. Here temporal evolution of the flow has been investigated as the conditions along the flow are periodic. What is important is to study the spatial evolution for various entrance and exit conditions. These conditions will determine which of the multiple states is realised in practice. For example, one state may exist when the flow is enters the magnetic field, but another when the flow follows a 90 or 180 degree bend, as in certain blanket designs.

Another type of flow that needs to be studied is for a duct with finite conductivity of thin walls. The reason is that the balance of the fluid carried by the core and the jets strongly depends on this. In some cases the finite flow in the core may lead to situations with more intensive flow mixing.

Ultimately, the test for a blanket concept is how efficiently heat and tritium are removed from the blanket. Therefore, the final step is to study the non-isothermal flows. At the present moment, the rigorous tests that have been carried out on this specific blanket design (Hunt's flow) have demonstrated that it would not be an ideal candidate for use within a nuclear fusion reactor environment. The reason for this has been self-evident throughout this investigation at higher values of *Ha*: heat and mass transfer are of paramount importance within blanket design and development. Due to the increasingly strong electromagnetic forces

which are present within an MHD flow regime subjected to high magnetic fields, as in a fusion reactor. It has been demonstrated through this study that this greatly reduced the turbulent nature of the flow within the core, thus severely hindering the turbulent nature of the fluid contained within. This in turn, hinders the heat and mass transfer capabilities within this particular specific blanket design.

List of Figures

[1a] http://www.statemetalindustries.com/statemetalindustries/

[1b] https://www.iter.org/newsline/252

[2] http://www.nature.com/nphys/journal/v12/n5/fig_tab/nphys3759_F1.html

[3] https://uk.pinterest.com/pin/25755029089495154/

[4] http://www.nasa.gov/mission_pages/sunearth/news/gallery/Earths-magneticfieldlines-dipole.html

[5] http://link.springer.com/chapter/10.1007/978-1-4020-4833-3_10#page-1

[6] http://images.slideplayer.com/24/7026236/slides/slide_13.jpg

[7]https://www.google.co.uk/search?site=&tbm=isch&source=hp&biw=1299&bih=661&q=electrically+insulatind+square+channel&oq=electrically+insulatind+square+channel&gs_l=img.3...4230.18366.0.19782.38.13.0.25.10.0.183.1544.5j8.13.0....0...1ac.1.64.img..0.22.1673...0j0i30j0i8i30j0i24.pROc4C7HKbo#tbm=isch&q=magnetofluiddynamics+in+channels+and+containers&imgrc=

Bibliography

[1] Borgstedt, H. U. & Glasbrenner, H. 1995 Development of a direct insulation layer for a self cooled liquid meal fusion reactor blanket. *Fusion Sng & Design, vol* ***27,*** 659-662.

[2] Madarame, H., Tillark, M. S. & Taghavi, M. S. 1985 The influence of leakage currents on MHD pressure drop. *Fusion Technology, vol* ***8***, 264-269.

[3] Tillark, M.S. & Morley, N. B. 1995 Flow balancing in liquid metals. *Fusion Eng & Design, vol* ***27***, 735-741.

[4] Hartmann. J. & Lazarus. F. 1937 Experimental investigation on the flow of Mercury in a homogeneous magnetic field. *Danske Vid Sels Mar-Fys Medd XV, vol* ***7,*** 1 - 45.

[5] Alfven, H. 1943 On the existence of electromagnetic - hydrodynamic waves. *Arkiv f Mat Astron o Fys, vol* ***29B*** *(2)*, 1 - 7.

[6] http://www.iter.org/sci/whatisfusion.

[7] Braams, C. M. & Spatt. P. E. 2002 *Nuclear Fusion: Half a century of Magnetic Confinement.* Institute of Physics Publishing. ISBN 0-7503-0705-6

[8] Kobzen, A. P. 2010 The mechanism of Vavilov – Cherenkov Raditation. Physcics of Particles and Nuclei, vol **41** No 3, pp 452 – 470.

[9] http://home.physics.ucla.edu/calendar/conference/cmpd/talks/cowley.pdf

[10] Electromagnetic waves in a plasma, in Leontovich: 1963 Reviews of Plasma Physics, vol. **3**.

[11] http://www.esi.nagoya-u.ac.ip/h/isets07/Contents/Session03/1348llgisonis.pdf.

[12] Dolan, T. J. 1982 Fusion Research, vol **1**.-Principles. Pergamon press. LCC QC791.D64.

[13] http://www.euro-fusion.org/newsletter/50-years-of-tokamaks/

[14] Artsimovich, L. A., Anashin, A. M., Gorgunov, D .P., Ivanov, D. P., Petrov, M. P. & Strelkov, V. S. 1971, March 29 Investigation of plasma neutron radiation from Tokomak T-3a installation. *Soviet physics Jetp, vol* ***34****, No 2*, 575 - 581.

[15] Shcheglov, D. A. & Kuznetsov, E. I. (1971). *Sov. Phys - Tech Phys., vol* ***15***, 1453.

[16] Bobrovski'l, G. A., Kuznetsov, E. I. & Razumova, K. A. 1971 *Sov. Phys.-JETP, vol **32***, 599.

[17] http://www.ialtenergy.com/joint-european-torus.html

[18] Khajeh Marjan, A. S. & Sobhanian, S. 2012 A new form of the Grad-Shafranov equation for a Tokomak with elongated cross section. *Journal of Theoretical and Applied Physics, vol **6***, 34.

[19] Strelkov, V. 2001 History of the T-10 Tokomak: Creation and Development. *Plasma Physics Report, vol **27***(No 10), 819 - 824.

[20] http://english.hf.cas.cn/ic/ip/ht7/

[21] Artsimovich, L. A., Brobrovskii, G. A. & Gorbunov, E. P. 1968 *Proc III Int. conf. Plasma Physics and Controlled Nuclear Fusion Research.* Vol ***1,*** 157. Novosibirsk: IAEA Vienna.

[22] Artsimovich, L. A., Anashin, E. P., Gorbunov, D. P., Ivanov, Petrov, M. P. & Strelkov, V. S. 1969 *JETP Lett, vol **10***, 82.

[23] Anashin, A. M., Gorbunov, D. P., Lysenko, S. E., Pikok, N. D., Robinson, Ch., Strelkov, V. S. & Sannikov, V. V. 1971 *Sov - Phys.-JETP, vol **33***, 1127.

[24] https://www.euro-fusion.org/2010/04/lecture-of-i-v-kurchatov-at-harwell

[25] http://www-naweb.iaea.org/napc/physics/2ndgenconf/data/Proceedings%201958/NG900090.pdf

[26] Alfven, H. 1942 Existence of electrodynamic-hydrodynamic waves. Nature, 150, 405 – 406.

[27] Trefthens, L.M. 1950 Heat transfer between a non-wetted surface and a moving fluid. Nature 165, 973.

[28] Murgatroyd, W. 1953 Experiments in magnetohydrodynamic channel flow. *Phil Mag, vol **44***, 1348 - 1354.

[29] Moffatt, H.K. 2011 John Arthur Shercliff 10 September 1927 – 6 December 1983. Osdfm.

[30] Shercliff, J. 1953 Steady motion of conducting fluids in pipes under transverse magnetic fields. Prec. Camb. Phil. Soc. 49, 136 – 144.

[31] Shercliff, J. 1954 Relation between the velocity profile and the sensitivity of electromagnetic flowmeters. J. appl. Phys. 25, 817.

[32] Shercliff, J. 1955 Some engineering applications of magnetohydrodynamics. Proc. R. Soc. Lond. A 233, 289.

[33] Shercliff, J. 1956 The flow of conducting fluids in circular pipes under transverse magnetic fields. J. Fluid. Mech. 1, 644 – 666.

[34] Shercliff, J. 1960 One- Dimensional magnetogasdynamics in oblique fields. *J Fluid Mech, vol **9***, 481 - 505.

[35] Shercliff, J. 1960 Some generlization on one-dimensional magnetohydrodynamics. *Rev Mod Phys, vol **32***, 980 - 986.

[36] Shercliff, J. 1977 *Vector Fields* (Vol. 1). Cambridge University Press. doi:ISBN 0521290929

[37] Hasimoto, H. 1960 Steady longitudinal motion of a cylinder in a conducting fluid. *J. Fluid Mech, vol **8***, 61 - 81.

[38] Alty, C. 1971 Magnetohydrodynamic duct flow in a uniform transverse magnetic field of arbitary orinentation. *J. Fluid Mech, vol **48***, 429 - 461.

[39] Baylis, J.A. 1964 Detection of the onset of instability in cylindrical magnetohydrodynamic flow. Nature, 204 – 563.

[40] Chandrasekhar, S. 1961 *Hydrodynamic and hydromagnetic stability.* Oxford: Clarendon Press.

[41] Baker, R. 1965 Maximum growth rate of Rayliegh-Taylor instabilities due to electromagnetic force. *Nature, vol **207***, 65 - 66.

[42] Hunt, J. C. 1965 Magnetohydrodynamic flow in rectangular ducts. *J. Fluid. Mech., vol **21***, 577.

[43] Hunt, J.C.R. & Stewartson, K. 1965 Magnetohydrodynamic flow in rectangular ducts. II. *J. Fluid. Mech., vol **23***, 563.

[44] Gilbert, W. 1991 *De Magnete.* (P. Fleury, Trans.) Dover Publications Inc.

[45] Elsasser, W. 1978 *Memoirs of a Physicist in the Atomic Age.* New York: Science History Publications.

[46] Elsasser, W. 1955 Hydromagnetism I. L. A. Review. Am J Phys 23, 590 – 609.

[47] Elsasser, W. 1955 Hydromagnetism II. L. A. Review. Am J Phys, 24, 85 – 110.

[48] Elsasser, W, 1950 The hydromagnetic equations. Phys Rev, 79, 183

[49] Muller, U. & Buhler, L. 2001 *Magnetofluiddynamics in Channels and Containers* (Vol. 1). Berlin: Springer – Verlag. ISBN 3-540-41253-0

[50] Malang, S. & Mattas, R. 2012 Comparison of lithium and the Eutectic lead-litium alloy, two candidate liquid metal breeder materials for self cooled blankets. *F. Eng & Design, vol **27** (1-2),* 399 - 406.

[51] Abdou, M. E. 1983 Blanket comparison and selection study-interim report. *Technichal Report ANL/FPP-83-1 I.* Argonne National Laboratory.

[52] Chang, C. & Lundgren, S. 1961 Duct flow in magnetohydrodynamics. *Zeitschrift fur angewandte Mathematik und Physik, XII*, 100-114.

[53] Hunt, J. C. R. & Hancox, R. 1971 *The use of liquid lithium as a coolant in a toroidal fusion reactor.* Technical report CLM-R 115, Culham Laboratory, Oxford.

[54] Smith, D. L., Baker, C. C., Sze, D. K., Morgan, G. D., Abdou, M. A., Piet, S. J., Schultz, S. R., Moir, R. W. & Gordon, J.D. 1985 Overview of the blanket comparison and selection study. *Fusion Technol, vol **8** (1),* 10-113.

[55] Shercliff, J. A. 1956 The flow of conducting fluids in circular pipes under transverse magnetic fields. *J. Fluid. Mech., vol **1**,* 644.

[56] Shercliff, J. A. 1962 Magnetohydrodynamic pipe flow. Part 2. *J. Fluid. Mech, vol **13**,* 513-19.

[57] Ludford, G. S. 1961 The effects of a very strong magnetic cross-field on steady motion through a slightly conducting fluid. *J. Fluid. Mech., vol **10**,* 141.

[58] Williams, W. E. 1962 Magnetohydrodynamic flow in a rectangular tube at high Hartmann Number. *J. Fluid. Mech., vol **16**,* 263.

[59] Brouillette, E. C. & Lykoudis, P. S. 1967 Magneto-fluid-mechanics channel flow. I Experiment, *The Physics of Fluids vol **10***(4), 995-1001.

[60] Todd, L. 1966 Hartmann flow in an annular channel. *J. Fluid Mech., vol **28**,* 371.

[61] Hunt, J. C. R. & Williams, W. E. 1967 Some electrically driven flows in magnetohydrodynamics. Part 1. Theory. *J. Fluid Mech., vol **31***, 705.

[62] Hunt, J. C. R. & Malcolm, D. G. 1967 Some electrically driven flows in magnetohydrodynamics. Part 2. Theory and experiment. *J. Fluid Mech., vol **33***, 775.

[63] Hunt, J. C. R. & Leibovich, S. 1967 Magnetohydrodynamic flow in channels of variable cross-section with strong transverse magnetic fields. *J. Fluid Mech., vol **28,*** 241-260.

[64] Hunt, J. C. R. & Ludford, G. S. S. 1968 Three-dimensional MHD duct flows with strong transverse magnetic fields. Part 1. Obstacles in a constant are channel. *J. Fluid Mech., vol **33***, 693-714.

[65] Hunt, J. C. R. & Branover, G. G. 1969 Magnetohydrodynamic flow in a rectangular channel with walls of finite conductivity. *Magnitnaya Gidrodinamika, vol **5***(3), 139-142.

[66] Hunt, J. C. R. & Shercliff, J. A. 1971 Magnetohydrodynamics at high Hartmann Number. *Annu. Rev. Fluid Mech, vol **3***, 37-62.

[67] Uflyand, Y. S. 1961 *Sov. Phys. Tech. Phys, vol **5***, 1194.

[68] Gelfgat, Yu., Dorofeev, V. S. & Scherbinin, E. V. 1971 Experimental investigation of the velocity structure of and MHD flow in a rectangular channel. *Magnetohydrodynamics, vol **7***, 26 - 29.

[69] Platnieks, I. & Freibergs, J. 1972 Turbulence and some problems in the stability of flows with M-shaped velocity profiles. *Magnetohydrodynamics, vol **8***, 164 - 168.

[70] Moffat. H. K. 1978 Magnetic field generation in electrically conducting fluids. *Cambridge University Press*.

[71] Almenay. A., Moreau. R., Sulem. P. L. & Frisch. U. 1979 Influence of external magnetic field on homogeneous MHD turbulence. *J de Mecanique, vol **18***, 280-313.

[72] Holroyd. R. J. & Walker. J. S. 1978 The theoretical study of the effects of wall conductivity, non-uniform magnetic fields and variable-area ducts on liquid metal flows. *J Fluid Mech., vol **84** (3),* 471-495.

[73] Walker J. S, Ludford G. S. S. & J. C. R. Hunt . 1971 Three dimensional MHD duct flows with strong transverse magnetic fields. Part 2. Variable-area rectangular ducts with conducting sides. *J Fluid Mech., vol **46**,* 657-684.

[74] Garnier, M., Alemany. A., Sulem, P. L. & Pouquet, A. 1981 Influence of an external magnetic field on large scale low magnetic Reynolds number MHD turbulence. *Journal de Mecanique, vol **20** (2),* 233 - 251.

[75] Moss, E. 1983 Transition to turbulence in accelerating flows. *Israel J. of Technology, vol **21***, 221-226.

[76] Greenblatt, D. & Moss, E. A. 2003 Rapide transition to turbulence in pipe flows accelerated from rest. *J. Fluid Eng, vol **125**,* 1072-1075.

[77] Eckhardt, B., Schneider, T. M., Hof, B. & Westerwell, J. 2007 Turbulence transition in pipe flow. *Annu. Rev. Fluid Mech., vol **39***, 447-468.

[78] Jones, O. 1976 An improvement in the calculations of turbulent friction in rectangular ducts. *J. Fluids Engng, vol **98***, 173-181.

[79] Peixinho, J. & Mullin, T. 2006 Decay of turbulence in duct flow. *Phys. Rev. lett, vol **96**,* 094501.

[80] Tatsumi, T. & Yoshimura, T. 1990 Stability of the laminar flow in a rectangular duct. *J. Fluid Mech, vol **212**,* 437-449.

[81] Uhlmann, M., Pinell, A., Kawahara, G. & Sekimoto, A. 2007 Marginally turbulent flow in a square duct. *J. Fluid Mech., vol **588**,* 153-162.

[82] Reed, C. B. & Picologlou, B. F. 1989 Side wall flow instabilities in liquid metal MHD flows under blanket relevant conditions. *Fusion Tech., vol **15**,* 705-715.

[83] Stieglitz, R., Barleon, L., Buhler, L. & Molokov, S. 1996 Magnetohydrodynamic flow in a right hand bend in a strong magnetic field. *J. Fluid Mech, vol **326**,* 91-123.

[84] Stieglitz, R. & Molokov, S. 1997 Experimental study of magnetohydrodynamic flows in electrically coupled bends. *J. Fluid Mech., vol **343***, 1-28.

[85] Ting, A. L., Walker, J. S., Moon, T. J., Reed, C. B. & Picologlou, B. F. 1991 Linear stability analysis for high velocity boundary layers in liquid metal magnetohydrodynamic flows. *Int. J. Engng. Sci., vol **29***, 939-948.

[86] Mueck, B. 2000 Three dimensional simulation of MHD side-layer instabilities. *4th Int. PAMIR Conf., vol **1***, pp. 297-302. Giens, France.

[87] Yoshizawa, A. 1987 Sub-grid modelling for magnetohydrodynamic turbulent shear flows. *Annu Rev Fluid Mech., vol **30** (4),* 1089 - 1095.

[88] Theobald, M., Fox, P. & Sofia, S. 1994 A subgrid-scale resistivity for magnetohydrodynamics. *Phys Plasmas, vol **1***, 3016 - 3032.

[89] Agullo, O. Muller, W. C., Knaepen, B. & Carati, D. 2001 Large eddy simulation for decaying magnetohydrodynamic turbulence with dynamic subgrid modelling. *Phys Plasmas, vol **7,*** 3502 - 3505.

[90] Coleman, G. N., Ferzinger, J. H. & Spalart, P. R. 1992 Simulation of the stably stratified turbulent Ekman layer. *J Fluid Mech., vol **244***, 677 - 712.

[91] Corral, R. & Jimenez, J. 1995 Fouier/Chebyshev methods for the incompressible Navier-Stokes equations in finite domains. *J Comp. Phys., vol **121***, 261 - 270.

[92] Hussaini, M. Y. & Zang, T. A. 1987 Spectral methods in fluid dynamics. *Annu. Rev. Fluid Mech., vol **19***, 339 - 367.

[93] Kolmogrov, A. 1991 The local structure of turbulence in incompressible viscous fluids for very large Reynolds numbers. *R. Soc. Lond. A, vol **434***, 9 - 13.

[94] Spalart, P. 1988 Direct simulation of a turbulent boundary layer up to Re=1410. *J Fluid Mech., vol **187***, 61 - 98.

[95] Madabhushi, R. K. & Vanka, S. P. 1991 Large eddy simulaton of turbulence driven secondary flow in a square duct. *Phys. Fluids A., vol **3***, 2734 - 2745.

[96] Gavrilakis, S. 1992 Numerical simulation of low Reynolds number turbulent flow through a straight duct. *J Fluid Mech., vol **244***, 101 - 129.

[97] Madabhushi, R. K. & Vanka, S. P. 1993 Direct numerical simulation of turbulent flow in a square duct at low Reynolds number, Near wall turbulent flows. (E. Launder, Ed.) *RMC So. C.G. Speziale and B.*

[98] Noguchi, H. & Kasagi, N. 1994 Direct numerical simulation of liquid metal MHD turbulent channel flows. *(in Japenese) Reprint of JSME No 940 -53,* 365 - 366.

[99] Buhler, L. & Horanyi. 2009 *Fusion Eng. Des., 84,* 518.

[100] Krasnov, D., Rossi, M., Zikanov, O. & Boeck, T. 2008 Optimal growth and transition to turbulence in channel flow with spanwise magnetic field. *J Fluid Mech., vol* ***596***, 73 - 101.

[101] Krasnov, D., Zienicke, O., Zikanov, O., Beock, T. & Thess, A. 2004 Numerical study of the instabilitites of the Hartmann Layer. *J Fluid Mech., vol* ***504***, 183 - 211.

[102] Kinet, M., Knaepen, B. & Molokov, S. 2009 Instabilities and transition in magnetohydrodynamic flows in ducts with electrically conducting walls. *Phys Rev Lett, vol* ***103***, 154501.

[103] Priede, J., Aleksandrova. & S., Molokov. 2010 Linear stability of Hunt's flow. *J Fluid Mech., vol* ***649***, 115 - 134.

[104] Zhao, Y. & Zikanov, O. 2012 Instabilities and turbulence in magnetohydrodynamic flow in a toroidal duct prior to transition in Hartmann Layers. *J Fluid Mech., vol* ***692***, 288 - 316.

[105] Shercliff, J. A. 1956 Steady motion of conducting fluids in ppes under transverse magnetic fields. *J. Fluid Mech., vol* **1**, 644-666.

.

[106] Peyet, R. 2002 *Spectral methods for incompressible viscous flows.* New York: Springer.

[107] Krasnov, D., Thess, A., Beock, T. (2013). Patterned turbulence in liquid metal flows: Computational reconstruction of the Hartmann Experiment. *Phys. Rev. Lett, 110,* 084501.

[108] Krasnov, D., Zikanov, O., Beock, T. (2011). Comparative study of finite difference approaches to simulation of magnetohydrodynamic turbulence at low magnetic Reynlds number. *Comp. Fluids, vol* ***50***, 46 - 59.

[109] Canuto, C., Hussaini, M. Y., Quarteroni, A. & Zang, T. A. 2007 *Spectral Methods: Evolution to complex Geometries and Applications to Fluid Dynamics*. Berlin: Springer – Verlag Heidelberg,

[110] Morinishi, Y., Lund, T. S., Vasilyev, O. V. & Moin, P. 1998 Fully conservative high order finite difference schemes for incompressible flow. *J. Comp. Phys., vol* ***143***, 90 - 124.

[111] Ni, M. J., Munipalli, R., Huang, P., Morley, N. B. & Abdou, M. A. 2007a A current density conservative scheme for incompressible MHD flows at a low magnetic Reynolds number. Part I: On a rectangular grid system. *J. Comp. Phys., vol* ***227***, 174 – 204.

[112] Ni, M. J., Munipalli, R., Huang, P., Morley, N. B. & Abdou, M. A. 2007b A current density conservative scheme for incompressible MHD flows at a low magnetic Reynolds number. Part II: On an arbitary collocated mesh. *J. Comp. Phys., vol* ***227***, 205 - 228.

[113] Adams, J. A., Swarztrauber, P., Sweet, R. Efficient fortran subprograms for the solution of seperable elliptic partial differential equations. http://www.cisl.ucar.edu/css/software/fishpack/.

[114] Adams, J. C. Mudpack: Multigrid software for elliptic partial differential equations. http://www.cisl.ucar.edu/css/software/mudpack/.

[115] Walker, J. 1981 Magnetohydrodynamic flows in rectangular ducts with thin conducting walls. *Journal de Mecanique, 20,* 79 - 112.

[116] Sterl, A. 1990 Numerical simulation of liquid metal MHD flows in rectangular ducts. *J. Fluid Mech, vol* ***216***, 161 – 191.

[117] Kinet, M. 2009 MHD turbulence at low magnetic Reynolds number: Spectral properties and transition mechanism in a square duct. *Doctoral Thesis*. Universite Libre de Bruxelles, Belgium.

[118 Drazin, P. G. & Reid, W. H. 2004 *Hydrodynamic stability*. Cambridge University press.

[119] Kerswell, R. R. 2005 Recent progress in understanding the transition to turbulence in a pipe. *Nonlinearity*, 18 (6):17-44.

[120] Lehnert, B. 1952 On the behaviour of an electrically-conductive liquid in a magnetic field. Arkiv For Fysik, 5:69-90.

[121] Lehnert, B. 1955 An instability of laminar flow of mercury caused by an external magnetic field. *Proceedings of the Royal Society of London. Series A. Mathematical and Physical Sciences*, pgs 299-302.

[122] Burr, U., Barleon, L., Muller, U., Tsinober, A. 2000 Turbulent transport of momentum and heat in magnetohydrodynamic rectangular ducts with strong side wall jets. J. Fluid Mech, 406:247-279.

[123 Walker, J. S. 1981 Magnetohydrodynamic flows in rectangular ducts with thin conducting walls. *Journal de Mecanique*, 20(1):79-112.

[124] Moresco, P., Alboussiere, T. 2004 Experimental study of the instability of the Hartmann layer. J. Fluid Mech, 504:167-181.

[125] Muller, U. & Buhler, L. Magnetofluiddynamics in channels and containers. Springer. 2001.

[126] Banjura, R. A. & Catalano, M. R. 1974 Transition in a two-dimensional plane wall jet, J. Fluid. Mech., 70: 773 – 799.

[127] 1112Buhler, L. & Horanyi, S. 2009 Measurements of time dependent liquid metal magnetohydrodynamic flows in a flat rectangular duct. Fusion Engineering and Design. 84, 518-521.

[128] Schmid. P. J. & Hennington, D. S. Stability and Transition in Shear flows. Springer, Berlin. 2001.

[129] 14Jeong, J. & Hussein, F. 1995 On the identification of a vortex. J. Fluid. Mech, 285(1): 69 – 94.

[130] Braiden, L., Krasnov, D., Molokov, S., Boeck, T. & Buhler, L. 2016 Transition to Turbulenc in Hunt's Flow in a Moderate Magnetic Field. *EPL* G37015.

MATLAB

Calculating jet width

```
% Taking slice at midpoint of data showing  /\___/\ profile
midpoint=ceil(size(U,2)/2); % find midpoint
Zslice=Z(midpoint,:)';      % Y positions of slice
Uslice=U(midpoint,:);       % Values at y positions

% finding maximum of jet on left hand side of slice  /\_
% storing value (Umax) and location (Umaxlocation)
[Umax,Umaxlocation]=max( Uslice( 1:midpoint ) );


Umidpoint=Umax/2;  % value of U to measure width of jet at (1/2 maximum
value)


u2=find( Uslice(1:Umaxlocation) > Umidpoint,1 );   % finds 1st point where
value of U is greater than Umidpoint (1/2 maximum value)   (above)
u1=u2-1;                                          % gets the point just the
other side of Umidpoint (point before prevous point)     (below)
u4=find(Uslice(Umaxlocation:midpoint) < Umidpoint,1)+Umaxlocation-1;
                                                  % finds 1st point after the
maximum where value of U is less than 1/2 maximum value (below)
u3=u4-1;                                          % gets the point just the
other side of Umidpoint (point before prevous point)     (above)

ZvalueLHS=interpy(Zslice(u1),Zslice(u2),Uslice(u1),Uslice(u2),Umidpoint);
    % Interpolates between points either side of Umidpoint on LHS of peak
to
    % find Y value at U=1/2 maximum value on LHS of peak

ZvalueRHS=interpy(Zslice(u3),Zslice(u4),Uslice(u3),Uslice(u4),Umidpoint);
    % Interpolates between points either side of Umidpoint on RHS of peak
to
    % find Y value at U=1/2 maximum value on RHS of peak

Zwidth=ZvalueRHS-ZvalueLHS % finds Z width, the distance between Z values
at U= 1/2 maximum value

% Uslice([u1,u2,u3,u4]) % Displays U value before and after 1/2 maximum
value
% Yslice([u1,u2,u3,u4]) % Displays Y values corresponding the the U values
above

% Taking slice at midpoint of data showing  /''\ profile
Yslice=Y(:,Umaxlocation);
Uslice=U(:,Umaxlocation)';

utemp=find(Uslice > Umidpoint); % finds the locations where U is greater
than 1/2 maximum value
u2=utemp(1);        % takes the first of these locations just after U rises
above 1/2 maximum value
u1=u2-1;            % find the location just before previous point (last
point where U is below maximum value on LHS)
u3=utemp(end);      % takes the last location just before U falls below 1/2
maximum value
```

```
u4=u3+1;            % finds location just after previos point (first point
where U is blow maximum value on RHS)

YvalueLHS=interpy(Yslice(u1),Yslice(u2),Uslice(u1),Uslice(u2),Umidpoint);
    % Interpolates between points either side of Umidpoint on LHS of peak
to
    % find X value at U=1/2 maximum value on LHS of peak

YvalueRHS=interpy(Yslice(u3),Yslice(u4),Uslice(u3),Uslice(u4),Umidpoint);
    % Interpolates between points either side of Umidpoint on RHS of peak
to
    % find X value at U=1/2 maximum value on RHS of peak

Ywidth=YvalueRHS-YvalueLHS % finds Y width, the distance between Y values
at U= 1/2 maximum value
```

Cross section V_y & V_z

```
midpoint=ceil(size(U,2)/2);
figure(4)
plot(Z(midpoint,:),U(midpoint,:),'-b')
title ( 'Hunts flow Z axis')

midpoint=ceil(size(U,1)/2);
figure(5)
plot(Y(:,midpoint),U(:,midpoint),'-b')
title ('Hartmann Layer and flat core, Y direction')
```

Energy Integral

```
% Inputs
fname=input('Enter file name to look at ( no extension): ','s');
columnToUse = input('Enter column number (2 to 6): '); % column of file
containing the data t plot & integrate

data = load([fname '.oft']);    % This loads the file chosen
numtimesteps=size(data,1);

npt = input(['Enter number of integratio time steps (max '
num2str(numtimesteps) '): '])-1;

% Now this following commands goes and gets the data from the loaded file
time = data(:,1); % gets the time
dataFromColumn = data(:,columnToUse);  % this gets the data from the
desired column
```

```
% Fix jumps in the time between the runs
needs_fixing = any(diff(time)<0);
previousJumps = 0;
while needs_fixing
    currentJump = find(diff(time)<0,1);
    time((currentJump+1):end) = time((currentJump+1):end)+time(currentJump)
- previousJumps;
    needs_fixing = any(diff(time)<0);
    previousJumps = time(currentJump);
end

% The following plots and calculates the integral
figure()
if npt == numtimesteps+1
plot(time,dataFromColumn,'-b')
else
plot(time,dataFromColumn,'-r',time((end-npt):end),dataFromColumn((end-
npt):end),'-b')
end
total_integral = trapz(time,dataFromColumn)
integral_LastPoints = trapz(time((end-npt):end),dataFromColumn((end-
npt):end))
%approximate the line height = total integral / time(end)
%approximate the line height from the last point = integral last point/
%time(end)-time(end-npt-1))
```

Hysteresis

```
%% HYSTERESIS DOWN - get data points

% set up
figure  % make a new figure
set(gcf,'name','HYSTERESIS DOWN') % name the figure
cd('C:\Users\braidenl\Documents\MATLAB\Post_SEPTEMBER_2014_RESULTS\ZEUS
SIMULATION RUNS\All matlab Information\HYSTERESIS DOWN\7010000_ITS Fin Re
500')
load flux.oft % navigate to hysterysis down folder and load flux (for
finding changes in Hartman number)
%% Identify changes in Hartman number
start_point = 3000; % skip begining where system is unstructured
number_of_jumps = 11; % number of Hartman number values

data = flux(:,3); % use dp/dx to find changes in Hartman number

%%%%%%%%%%% algorith to detect changes n Hartman number %%%%%%%%%%%%%%%%%%%
% looks for increasngly bigger jumps in dp/dx, and uses the later values
last_point=data(start_point-1); % intialise point
max_diff = abs(data(start_point)-data(start_point-1)); % inital diffrence
between initial points
jumps_down=[]; % initalise locatons array
```

```
for ii = start_point:numel(data)% from the start point to the end of the
data
    current_point = data(ii); % update current point
    if abs(current_point-last_point)>max_diff % test if diffrence between
last point and current point is biggest so far
        jumps_down(end+1)=ii; % if so store the index
        max_diff = abs(current_point-last_point); % and update the maximum
difference
    end
    last_point = current_point; % update last point for next iteration
end
%%%%%%%%%%%%%%%%%%%%%%%%%%%%%%%%%%%%%%%%%%%%%%%%%%%%%%%%%%%%%%%%%%%%%%%%%%%
jumps_down = jumps_down(end-number_of_jumps+3:end); % ony take last however
many data points to remove errors from small difference at start of
algorithm
jumps_down=[690,1035,jumps_down]; % manually add first points (As hard to
detect due to system being unstructured)


%%%%%%%%%%%%%%%%%%%%%%%%%%%%%%%% POPUP BOX %%%%%%%%%%%%%%%%%%%%%%%%%%%%%%%%
% gets file/ column from user and plots
filename = questdlg('Choose a file - Hysteresys
Down','File','enrg.oft','flux.oft','tauw.oft','flux.oft');
load(filename)
switch filename
    case 'enrg.oft'
        columnNumber= listdlg('promptString','Choose a
column','name','Column','listString',{'time','Etotal','E'''','Ex'''','Ey'''','
Ez'''},'Selectionmode','single');
        plot(enrg(:,columnNumber))
    case 'flux.oft'
        columnNumber = listdlg('promptString','Choose a
column','name','Column','listString',{'time','flux','dp/dx','Tw'},'Selectio
nmode','single');
        plot(flux(:,columnNumber))
    case 'tauw.oft'
        columnNumber = listdlg('promptString','Choose a
column','name','Column','listString',{'time','Tw','Ty','Tz'},'Selectionmode
','single');
        plot(tauw(:,columnNumber))
    otherwise
        error('Problem with options')
end
%%%%%%%%%%%%%%%%%%%%%%%%%%%%%%%%%%%%%%%%%%%%%%%%%%%%%%%%%%%%%%%%%%%%%%%%%%%

% adds tick marks and labels for Hartman numbers
Ha = [10:-1:1,0.5]; % genretate decending Hartman numbers
Ha = num2str(Ha.'); % convert to text
set(gca,'Xtick',jumps_down,'XtickLabel',Ha) % add labels at locations
calulated by algorithm earlier


%%
%%%%%%%%%%%%%%%%%%%%%%%%%%%%%%%%%%%%%%%%%%%%%%%%%%%%%%%%%%%%%%%%%%%%%%%%%%%
%% HYSTERESIS UP
figure
set(gcf,'name','HYSTERESIS UP')
```

```
cd('C:\Users\braidenl\Documents\MATLAB\Post_SEPTEMBER_2014_RESULTS\ZEUS
SIMULATION RUNS\All matlab Information\HYSTERESIS UP\7010000 Re 10000
complete')
load flux.oft

%%
end_point = 1;
number_of_jumps = 11; % number of jumps from end

data = flux(:,3);
last_point=data(end);
max_diff = abs(data(end-1)-data(end));
jumps_up=[];

% algorit as above but works in other direction along x axis
for ii = numel(data)-1:-1:end_point
    current_point = data(ii);
    if abs(current_point-last_point)>max_diff
        jumps_up(end+1)=ii;
        max_diff = abs(current_point-last_point);
    end
    last_point = current_point;
end



jumps_up = jumps_up(end-number_of_jumps+1:end);
jumps_up = fliplr(jumps_up);% flip as algoritm was done backwards
%%
filename = questdlg('Choose a file - Hysteresys
Up','File','enrg.oft','flux.oft','tauw.oft','flux.oft');
load(filename)
switch filename
    case 'enrg.oft'
        columnNumber= listdlg('promptString','Choose a
column','name','Column','listString',{'time','Etotal','E'''','Ex'''','Ey'''','
Ez'''},'Selectionmode','single');
        plot(enrg(:,columnNumber))
    case 'flux.oft'
        columnNumber = listdlg('promptString','Choose a
column','name','Column','listString',{'time','flux','dp/dx','Tw'},'Selectio
nmode','single');
        plot(flux(:,columnNumber))
    case 'tauw.oft'
        columnNumber = listdlg('promptString','Choose a
column','name','Column','listString',{'time','Tw','Ty','Tz'},'Selectionmode
','single');
        plot(tauw(:,columnNumber))
    otherwise
        error('Problem with options')
end
%%
Ha = [0.5,1:10];
Ha = num2str(Ha.');
set(gca,'Xtick',jumps_up,'XtickLabel',Ha)

cd('C:\Users\braidenl\Documents\MATLAB') % navigate back to 'default'
directory
```

Velocity Profile V_x, V_y & V_z

```
load vel2
for i=1:129;
    for j=1:129;
        Z(i,j)= vel2(j+(i-1)*129,1);
        Y(i,j)= vel2(j+(i-1)*129,2);
        U(i,j)= vel2(j+(i-1)*129,3);
        V(i,j)= vel2(j+(i-1)*129,4);
        W(i,j)= vel2(j+(i-1)*129,5);
        dUdY(i,j)= vel2(j+(i-1)*129,6);
        dUdZ(i,j)= vel2(j+(i-1)*129,7);
    end
end
figure(1)
mesh(Z,Y,U)
xlabel('z'),ylabel('y');zlabel('x')
figure(2)
mesh(Z,Y,V)
figure(3)
mesh(Z,Y,W)
figure(4)
mesh(Z,Y,dUdY)
title('dU/dy')
figure(5)
mesh(Z,Y,dUdZ)
title('dU/dz')
```

Velocity profile Time and Domain averaging at z = 0

```
load vel0

for i=1:129;
    for j=1:129;
        Z(i,j)= vel0(j+(i-1)*129,1);
        Y(i,j)= vel0(j+(i-1)*129,2);
        U(i,j)= vel0(j+(i-1)*129,3);
        V(i,j)= vel0(j+(i-1)*129,4);
        W(i,j)= vel0(j+(i-1)*129,5);
        dUdY(i,j)= vel0(j+(i-1)*129,6);
        dUdZ(i,j)= vel0(j+(i-1)*129,7);
    end
end
figure(1)
mesh(Z,Y,U)
xlabel('z'),ylabel('y');zlabel('x');
figure(2)
mesh(Z,Y,V)
figure(3)
mesh(Z,Y,W)
figure(4)
```

```
mesh(Z,Y,dUdY)
title('dU/dy')
figure(5)
mesh(Z,Y,dUdZ)
title('dU/dz')
```